HYDROMECHANICAL FRAMEWORKS FOR ASSESSING THE OCCURRENCE OF WELLBORE BRIDGING AND FRACTURE BROACHING DURING BLOWOUTS

A Dissertation

by

OLUWAFEMI ISAAC OYEDOKUN

Submitted to the Office of Graduate and Professional Studies of
Texas A&M University
in partial fulfillment of the requirements for the degree of

DOCTOR OF PHILOSOPHY

Chair of Committee,	Jerome J. Schubert
Committee Members,	Junuthula N. Reddy
	Thomas Blasingame
	Peter Valko
Head of Department,	A. Daniel Hill

May 2017

Major Subject: Petroleum Engineering

ABSTRACT

Rigorous hydromechanical frameworks needed for modeling wellbore bridging and broaching during uncontrolled production of oil and gas are developed in this work. First, two sources of sand production are identified: borehole breakout and erosion of the producing formation. Theoretical framework for predicting the morphology of type B breakout mode is developed for the first time in this study; both fracture mechanics and shear failure theories are used in predicting the breakout geometry. Furthermore, a framework for estimating the size of caving produced during breakout (type A or B) is presented. Using asymptotic analysis of crack-boundary interactions, the state of damage around the borehole during the breakout process is determined, and the limiting buckling lengths of the resulting wing-cracks are predicted based on plate buckling theory. Third, a three-phase erosion kinetic equations, coupled with an erosion constitutive law, which is based on virtual power principle, are used in modeling radial and axial erosion in the reservoir and along the wellbore respectively. The proposed erosion constitutive law identifies the limitation of the pressure-gradient phenomenological model, which is currently being used. For a rigorous investigation into the self-killing of the well, a thermodynamically multiphase field model is developed for the gas-liquid-solid flow. The model, which is the combination of Navier-Stokes and Cahn-Hilliard type equations, incorporates the hydrodynamic interactions among the different species of the mixture. Lastly, this work considers a faster means for estimating fracture propagation in heterogeneous media (layered or naturally fractured) in the event the well is shut-in.

DEDICATION

Thanks to the Son of the living God, Jesus Christ, for the inspiration and strength He gave me throughout my graduate program. I also appreciate the understanding and support from my wife Oluwaseun Bangudu-Oyedokun.

ACKNOWLEDGEMENTS

I acknowledge the supports and advice of my research advisor, Dr. Jerome Schubert, and the rest of my dissertation committee. Similarly, I thank the Blowout Risk Assessment Joint Industry Project Companies for the permission to use this work for my PhD thesis.

CONTRIBUTORS AND FUNDING SOURCES

Contributors

This work was supervised by a dissertation committee consisting of Dr. Jerome Schubert (Chair), Dr. Peter Valko and Dr. Thomas Blasingame of the Department of Petroleum Engineering, and Dr. Junuthula Reddy of the Department of Mechanical Engineering.

The data used in Section 1 was retrieved from the works of Skalle et al. (1999). All other work for the dissertation was completed independently by the student.

Funding Sources

This work was sponsored by the Blowout Risk Assessments Joint Industry Projects.

TABLE OF CONTENTS

Page

ABSTRACT ii

DEDICATION iii

ACKNOWLEDGEMENTS iv

CONTRIBUTORS AND FUNDING SOURCES v

TABLE OF CONTENTS vi

LIST OF FIGURES x

LIST OF TABLES xvi

1. INTRODUCTION AND LITERATURE REVIEW 1

1.1 What Is a Blowout? 1
1.2 Casuses of Blowout 2
1.3 Past Studies on Blowout Control 3
1.4 Past Studies on Wellbore Breakout Analysis 5
1.5 Previous Studies on Hydraulic Fracture Containment 6
1.6 Research Problem Statements and Objectives 7
1.7 Dissertation Layout 8

2. THEORETICAL DEVELOPMENT ON MORPHOLOGY OF WELLBORE TOROIDAL BREAKOUT 10

2.1 Scope…. 10
2.2 Backgroud on Borehole Breakouts 11
2.3 Theory on Shear Fracture Induced Toroidal Spalling…… 15
2.4 Stress Distributions Around Wellbore……. 16
2.5 Breakout Pattern Under Shear Fracture 19
2.6 Breakout Depth and Width 22
2.7 Numerical Example of Type-B Breakout Pattern in a Homogeneous Fromation……. 26
2.8 Numerical Example of Type-B Breakout Pattern in a Heterogeneous Formation 31
2.9 Theory on Extensile Fracture Induced Toroidal Spalling…. 33

2.10 Breakout Pattern Under Extensile Splitting 34
2.11 Algorithm for Determing the Path of the Propagating Cracks 41
2.12 Numerical Example of Type-B Breakout Pattern Formed Through Extensile Splitting in a Homogeneous Formation 42
2.13 Breakout Volume… 47
2.14 Summary….. 47

3. ESTIMATING CAVING SIZE DURING WELLBORE BREAKOUT 49

3.1 Scope…. 49
3.2 Damage Initiation Around Wellbore 49
3.3 Failure Mechanism and Wing Crack Model 52
3.4 Initial Size of the Representative Pre-Existing Crack 59
3.5 Buckling Lengts of the Growing Slender Rock Layer 60
3.6 Breakout Width Estimation…. 63
3.7 Numerical Analysis…. 64
3.7.1 Parametric Studies on 1-D Plate Strip Approximation….. 64
3.7.1.1 Effect of Plain Strain Young's Modulus on Caving Size .. 64
3.7.1.2 Effect of In-situ Loading and Well Angles on Caving Size…… 65
3.7.1.3 Effect of Wellbore Shape on Caving Size……..... 67
3.7.2 Parametric Studies on Rectangular Plate Approximation…… 67
3.7.3 Effect of Back Stress on Unstable Crack Growth……. 69
3.8 Summary…. 73

4. DEVELOPMENT OF AN ENERGY-CONSISTENT EROSION CONSTITUTIVE RELATION FOR DEFORMABLE POROUS MEDIA 75

4.1 Scope….. 75
4.2 Background on Wellbore Erosion 76
4.3 Erosion Constitutive Law for Deformable Porous Media 80
4.3.1 Definition of Terms 80
4.3.2 Derivaton of the Energy-Consistent Erosion Constitutive Law 81
4.4 Derivation of Critical Erosion Hydraulic Gradient 90
4.5 Three-Phase Erosion Governing Equations 92
4.6 Critical Observations from the Proposed Erosion Constitutive Relation 96
4.7 Numerical Application 97
4.8 Summary 103

5. A THERMODYNAMICALLY CONSISTENT MULTIPHASE-FIELD MODEL FOR NON-ISOTHERMAL TRANSPORT OF GAS-LIQUID -SOLID PARTICLE FLOW: THEORETICAL DEVELOPMENT 105

5.1 Scope…… 105

5.2 Background on Multiphase Fluid Flow Modeling 105
5.2.1 Advanced Modeling Methods for Multicomponent Fluid Flows..... 109
5.2.2 Phase-Field Model..... 110
5.2.3 The Notion of Configurational Forces 111
5.3 Model Development..... 113
5.3.1 Mass Balance of Species 116
5.3.2 Balance of Linear Momentum 117
5.3.3 Energy Balance of the Mixture 118
5.3.4 The Second Postulate of Thermodynamics; Clausius-Duhem Inequality..... 119
5.3.5 Constitutive Relations 121
5.3.6 Constructing the Free Energy Functional and Diffuse Interface Thickness..... 126
5.4 Governing Field Equations..... 131
5.5 Summary 132

6. A QUICK AND ENERGY CONSISTENT ANALYTICAL METHOD FOR PREDICTING HYDRAULIC FRACTURE PROPAGATION THROUGH HETEROGENEOUS LAYERED MEDIA AND FORMATIONS WITH NATURAL FRACTURES: THE USE OF AN EFFECTIVE FRACTURE TOUGHNESS 134

6.1 Scope…. 134
6.2 Background on Hydraulic Fracture Modeling and Effective Fracture Toughness..... 135
6.3 Mathematical Formulations..... 137
6.3.1 Effective Fracture Toughness for Layered Media..... 137
6.3.2 Effective Fracture Toughness Derivation Without Tensile Stresses ... 142
6.3.3 Minimum Fracture Extension Pressures 143
6.3.4 Effective Fracture Toughness for Formations with Disordered Natural Fractures 145
6.3.5 Effective Fracture Toughness for Formations with Ordered Natural Fractures 150
6.4 Numerical Examples 150
6.5 Summary 159

7. CONCLUSIONS AND FURTHER WORKS..... 162

7.1 Wellbore Breakout Mechanisms 162
7.2 Erosion… 165
7.3 Thermodyamically Consistent Multiphase-Field Modeling of Gas-Liquid-Solid Flow..... 166
7.4 A Quick Method for Predicting Fracture Broaching..... 166
7.5 Future Works..... 167

NOMENCLATURE 169

REFERENCES 173

APPENDIX A: DERIVATION OF MINIMUM FRACTURE PROPAGATION PRESSURE FOR THREE-LAYER PROBLEM 206

APPENDIX B: LIST OF PUBLICATIONS FROM DISSERTATION 210

B.1 Peer-Reviewed Articles 210
B.2 Manuscripts Under Peer-Review 210

LIST OF FIGURES

FIGURE		Page
1.1	Blowout control methods used in 187 wells in OCS from 1960 to 1996 (Data from Skalle et al. 1999).	3
1.2	Blowout control methods used in 826 wells in Texas from 1960 to 1996 (Data from Skalle et al. 1999).	4
1.3	Borehole breakout classification according to Maury and Sauzay (1987).	6
2.1	(a) Plane view of the type-A breakout. (b) A 3D view of symmetric type-A breakout along an inclined wellbore.	12
2.2	Guenot and Maury's prediction of type-B breakout shape (Maur 1992)...	13
2.3	(a) A view of the breakout experiment performed by Perie and Goodman. The failed zones appear as concentric arcs to the borehole. (b) A schematic illustration of the propagating cracks in the breakout experiment. (c) A view of the propagating radial cracks and toroidal failure Reprinted with the permission from ASME. (Perie and Goodman 1989).	14
2.4	(a) Detail of the incipient breakout of inclined-segmented margins observed in particular well located in southern North Sea. (b) Occurrence of different breakout modes in a particular well located in the southern North Sea. (Plump 1989).	15
2.5	Longitudinal and radial shear fractures propagation.	20
2.6	Shear fractures in the r-z plane for a homogeneous formation. The deepest depth occurs at the center of the formation.	21
2.7	(a) Shear fractures in the r-z plane for a heterogeneous formation. The deepest depth occurs at a deeper location when the stronger zone is at the top of a weaker zone. (b) Shear fractures in the r-z plane for a heterogeneous formation. The deepest depth occurs at a shallower location when the weak zone is at top of a stronger zone.	22

FIGURE Page

2.8 Using the rational polynomial in fitting the data above. The solid orange line is the polynomial fit, while the dashed line is the data. The projected line is the solid blue line.... 28

2.9 Effective stress distribution at the wellbore wall. It is evident from the plot that breakout direction is at the azimuth of minimum horizontal in-situ stress..... 29

2.10 A schematic illustration of the projected straight lines. After determining the maximum break depth location with the fracture angle, the dashed lines illustrate the adjusted projection lines..... 30

2.11 Effective stress distributions at the wellbore wall..... 31

2.12 The area under the projected-lines over estimates the volume of sand produced. 32

2.13 (a) A schematic representation of the radial crack path. It is assumed that symmetric deformation occurs at the other end of the borehole. (b) A schematic representation of the longitudinal crack's path. The cracks are located at the azimuth of maximum compression (c) The intersections of the last line segments with the borehole geometry (points P and Q) yield the breakout width. This is done by solving a system of algebraic equations. 36

2.14. Schematic illustration of the path of the propagating radial crack..... 38

2.15. Schematic illustration of the paths of the propagating longitudinal cracks..... 40

2.16. Standing crack under compression loading, in the vicinity of a circular borehole, (in an infinite medium) under polyaxial loading, propagating through a wedging force..... 42

2.17. (a) The stress intensity factors distribution from the tip of the initial crack to the borehole boundary $(r-\theta)$. (b) The stress intensity factors distribution from the tip of the crack to the borehole boundary after the crack has increased in length (the first step size) $r-\theta$ plane (c) Estimation of the breakout width; only the quadrant is shown since symmetry is applicable. The breakout width in this case is almost 180^0.. 44

FIGURE Page

2.18. (a) Mode I stress intensity factor distribution from the tip of the initial crack to the borehole boundary ($r-z$ plane). (b) Mode II stress intensity factor distribution from the tip of the initial crack to the borehole boundary($r-z$ plane). (c) Mode I stress intensity factor distribution from the tip of the crack to the borehole boundary after the length has increased ($r-z$ plane). (d) Mode II stress intensity factor distribution from the tip of the crack to the borehole boundary after the length has increased ($r-z$ plane)..... 45

2.19. Breakout pattern in the $r-z$ plane..... 47

3.1. Damaged state around the wellbore prior to the stable propagation of the . standing initial cracks..... 50

3.2. Existing cracks propagating towards the direction of the maximum compressive force in the horizontal plane..... 52

3.3. Propagation of cracks in the vertical and horizontal planes..... 53

3.4. (a) Schematic of the forces acting on the slender rock layer (b) a representation of the foregoing problem by beam asymptotic..... 55

3.5. Comparing mode-1 stress intensity factor with numerical data; back stress is zero in this case. 57

3.6. Size of the representative pre-existing crack (enlarged size) in the horizontal plane. 59

3.7. Free body diagram showing the force system acting on the plate as viewed in the horizontal plane. 61

3.8. Free body diagram showing the force system acting on the plate as viewed in the vertical plane..... 62

3.9. Buckled rock plate as viewed in the horizontal plane..... 63

3.10. (a) Variation of caving size on plane strain Young's modulus. (b) Variation of caving size on plane strain Young's modulus an example case... 65

FIGURE Page

3.11. (a) Variation of caving size with buckling stress. (b) Variation of buckling stress with well angles. 66

3.12. Variation of caving size with borehole shape. 67

3.13. Influence of the initial damage state on the size of caving produced. In this example case, the Elastic modulus of the formation is taken to be 145 Kpsi, Poisson ratio and Vertical stress are assumed to be 0.3 and 4000 psi respectively. 68

3.14. Influence of in-situ stress loading on the size of caving produced. In this example case, *h*, Poisson ratio and elastic modulus are assumed to be 0.5in., 0.3, and 145Kpsi respectively. 69

3.15. Variation of (a) hoops stress, (b) radial stress, and (c) vertical stress around a circular wellbore with well angles. In this case A, the well azimuth is zero. 70

3.16. Variation of (a) hoops stress, (b) radial stress, and (c) vertical stress around a circular wellbore with well angles. In this case B, the well azimuth is zero. 71

3.17. Crack propagation in case A. 72

3.18. Crack propagation and arrest in case B. 73

4.1. Geometry of two spherical particles elastically deforming in contact. The dashed line represents the undeformed surface of each particle. 91

4.2. Pressure wave and eroson fronts during radial erosion. 96

4.3. Model domain and boundary conditions notation. 99

4.4. Pressure (in KPa) distribution in the open-channel and porous medium at the onset of erosion. 99

4.5. Velocity (in m/s) distribution in the open-channel and porous medium at the onset of erosion. 100

4.6. Shear rate (in 1/s) distribution in the open-channel and porous medium at the onset of erosion. 100

FIGURE Page

4.7. Distribution of fluidized particles concentration (in mol. /m^3) in the porous medium during the erosion process at times (a) 3s, (b) 10s, and (c) 20s. 101

4.8. Porosity evolution in the porous medium during the erosion process at times (a) 3s, (b) 10s, and (c) 20s 102

5.1. Representative volume element of the mixture of three species having different interface widths 114

6.1. Asymmetric multilayer hydraulic fracture propagation. 139

6.2. Asymmetric three-layer equilibrium height problem. 139

6.3. Possible fracture tips positions in three-layer media. 143

6.4. Region map of the tips positions when the pressure inside the fracture is 53.09MPa (7700 psi) for 11-EHP.. 152

6.5. Region map of the tips positions when the pressure inside the fracture is 53.78MPa (7800 psi) for 11-EHP. 152

6.6. Region map of the tips positions when the pressure inside the fracture is 54.47MPa (7900 psi) for 11-EHP. 152

6.7. Region map of the tips positions when the pressure inside the fracture is 53.09MPa (7700 psi) for 3ER-EHP. 152

6.8. Region map of the tips positions when the pressure inside the fracture is 53.78MPa (7800 psi) for 3ER-EHP 153

6.9. Region map of the tips positions when the pressure inside the fracture is 53.78MPa (7800 psi) for 3ER-EHP 153

6.10. Region map of the tips positions when the pressure inside the fracture is 54.47MPa (7900 psi) for 3BR-EHP. 154

6.11. Region map of the tips positions when the pressure inside the fracture is 54.47MPa (7900 psi) for 3WL-EHP. 154

6.12. Region map of the tips positions when the pressure inside the fracture is 54.47MPa (7900 psi) for 11-EHP, Case 2. 156

FIGURE Page

6.13. Region map of the tips positions when the pressure inside the fracture is 54.47MPa (7900 psi) for 3ER-EHP, Case 2..... 156

6.14. Region map of the tips positions when the pressure inside the fracture is 54.47MPa (7900 psi) for 3BR-EHP, Case 2. 156

6.15. Region map of the tips positions when the pressure inside the fracture is 54.47MPa (7900 psi) for 3WL-EHP, Case 2. 156

6.16. Region map of the tips positions when the pressure inside the fracture is 54.47MPa (7900 psi) for 3EER-EHP, Case 2. 157

6.17. Variations of the normalized shear modulus, μ_D, and normalized fracture toughness with damage in any material displaying a linear elastic response. $\lambda = 0$ in this case. 157

6.18. (a) Variation of the normalized shear modulus, μ_D, considering different infill materials (b) Variation of normalized fracture toughness, $K_{IC,D}$, with damage considering different infill materials 159

6.19. Comparing the performance of the proposed model for effective shear modulus of a material body having (a) empty or open natural fractures, Case 1, (b) micro-fractures filled with lower modulus material, Case 2, and (c) micro-fractures filled with higher modulus material, Case 3. 160

LIST OF TABLES

TABLE		Page
2.1	Breakout Depth and Width Variation with Depth	27
2.2	Comparison between Fracture Angle Calculated from Mohr Circle and Inclination Angle of the Failure Lines at Wellbore Interface.	27
2.3	Breakout Depth and Width Variation with Depth	32
3.1	Stress state and mechanical properties of the formation for case A	71
3.2	Stress state and mechanical properties of the formation for case B	72
4.1	Model parameters for axial erosion simulation	98
6.1	Description of the formation properties and in-situ stress profiles for the 11- layer problem	151
6.2	Description of the formation properties and in-situ stress profiles for the equivalent three-layer problem	151
6.3	Description of the formation properties and in-situ stress profiles for the 11-EHP, Case 2	155
6.4	Elastic Properties of the Matrix and Inclusions	158

1. INTRODUCTION AND LITERATURE REVIEW

After the Macondo oil spill in 2010, the petroleum exploration and development companies have been under severe scrutiny of their respective host governments to provide faster means of killing a blowing well. Drilling a relief well can take several days to complete and the use of cofferdams has its own limitations. Borehole bridging technology is currently being pursued by the industry as a faster alternative to kill a blowing well, but no detailed scientific investigations have been conducted on its viability. Therefore in this work I present rigorous hydromechanical frameworks for predicting the potential for self-killing or induced-bridging of blowing oil and gas wells. For borehole bridging to occur solid-particles (especially sand) must be produced or there is a significant reduction in the permeability of the producing formation(s), or reservoir pressure depletes significantly such that there is no sufficient energy to carry the reservoir fluids to the surface.

1.1 What Is a Blowout?

Uncontrolled influx of formation fluid(s) into the wellbore is termed “taking a kick” in the petroleum industry. When the kick is not detected or controlled early and the reservoir energy is sufficient to transport the formation fluid against the imposed back-pressure of the mud column, the whole wellbore will be filled with the reservoir fluid(s); then, it can be said that blowout has occurred.

Depending on the sink (outlet domain) of the formation fluids, blowout can be categorized into three: (1) surface blowout occurs when the formation fluids are

transported to the surface (above the sea level), (2) subsurface blowout occurs when the formation fluids are deposited into the sea, and (3) underground blowout is the deposition of the reservoir fluids into another rock formation. Underground blowout can occur with irrespective of the condition of the blowout preventer (BOP). When the BOP is closed, pressure builds-up in the wellbore, and when the fracture pressure gradient of any of the weak or soft formations is exceeded, the fluids create a path through these weak openhole-intervals. On the other hand, cross-flow into a depleted formation can lead to underground blowout, once the wellbore pressure exceeds the formation pressure, the fluid will diffuse into the formation.

1.2 Causes of Blowout

Blowout can occur during drilling and completion operations; but no interest is placed on blowouts occurrence during workover operations in this study. Therefore, the different causes of blowout during drilling operations are: (1) drilling into an abnormally high pressured formation, (2) tripping out of the borehole at a relatively high-speed such that the differential pressure caused by swabbing creates an underbalanced condition in the wellbore, (3) loss of the marine riser connecting the seabed to the rig in deepwater drilling operations, (4) flow through the casing-cement or cement-formation annuli as a result of the created flow-gap from the disproportionate expansions of the formation, casing, and cement, and (5) failure of the BOP to seal the well.

1.3 Past Studies on Blowout Control

Few studies have been conducted on blowout control analyses. One of the notable field studies include the statistical analysis of killing methods used between the year 1960

to 1996 in Texas and US Outer Continental Shelf (USOCS) by Skalle et al. (1998 and 1999). In this study the authors found out that 39.6% of blowouts in the USOCS were controlled by wellbore bridging (Fig. 1.1). While 16% of blowouts in Texas were controlled by bridging (Fig. 1.2); the difference in the percentage of wellbore bridging occurrences in these two locations could be as a result of change in lithology of the formations.

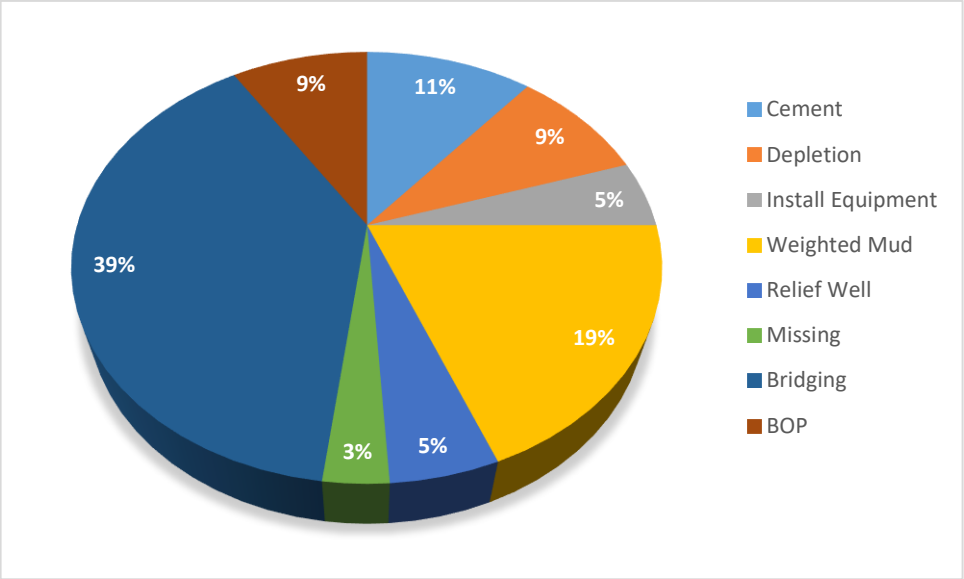

Fig. 1.1. Blowout control methods used in 187 wells in OCS from 1960 to 1996 (Data from Skalle et al. 1999).

Danenberger (1993) compiled blowout occurrences in the USOCS for over a 21-year period, from 1971 to 1991. Out of the total 21, 436 wells drilled, 87 blowouts were recorded and most of the blowouts were traced to shallow gas. Eighteen of the wells

stopped flowing within a one-hour period, 50 of the wells were controlled within a day, and 73 within a week. Sixty-two of the 87 blowouts were controlled by bridging, while the rest of the wells were killed by pumping mud or cement and activating the BOP.

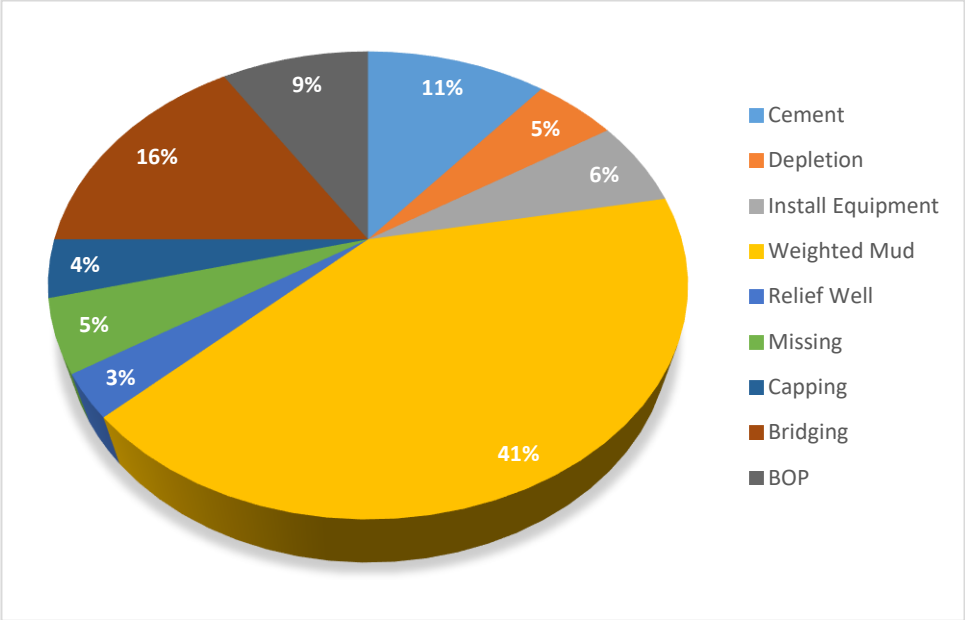

Fig. 1.2. Blowout control methods used in 826 wells in Texas from 1960 to 1996 (Data from Skalle et al. 1999).

Recently attempts were made to understand the physics behind the self-killing of blowing oil and gas wells, by studying the transient borehole failure and cavings transport during blowout. Nesheli and Schubert (2006) attempted to use the breakout analysis to qualitatively predict the potential for self-killing of blowing wells; they only estimated the breakout angle without determining the volume of solids produced. Wilson (2012) and

Wilson et al. (2013) were the first to thoroughly study the geomechanics and cuttings transport analyses during kick development and blowout. In their studies, borehole breakouts, erosion, collapse of overburden rocks, gas depressurization, and influx of aquifer into a gas reservoir were identified as the main mechanisms that can lead to self-killing of blowing wells. But they also concluded that blowouts from prolific deepwater reservoirs cannot be stanched by borehole breakouts or erosion only; in fact once the kick develops into a blowout, self-killing cannot be a reliable remedy in controlling the wells. They further emphasized the impact of rate of borehole failure in stanching the flow during kick development. If the borehole failure is enormous and rapid, the tendency for self-killing is higher compared with gradual borehole failure with the same amount of solids production.

1.4 Past Studies on Wellbore Breakout Analysis

Borehole breakout is one of the main borehole failure mechanisms that can lead to self-killing of wells. And as mentioned earlier, the rate of borehole failure is very critical when predicting the potential for borehole bridging. Wellbore breakouts are generally classified into four major categories, type A, B, C, and D (Maury and Sauzay 1987 and Guenot and Santarelli 1988).

As observed in Fig. 1.3, types A and B produce relatively large amount solids compared with type C.

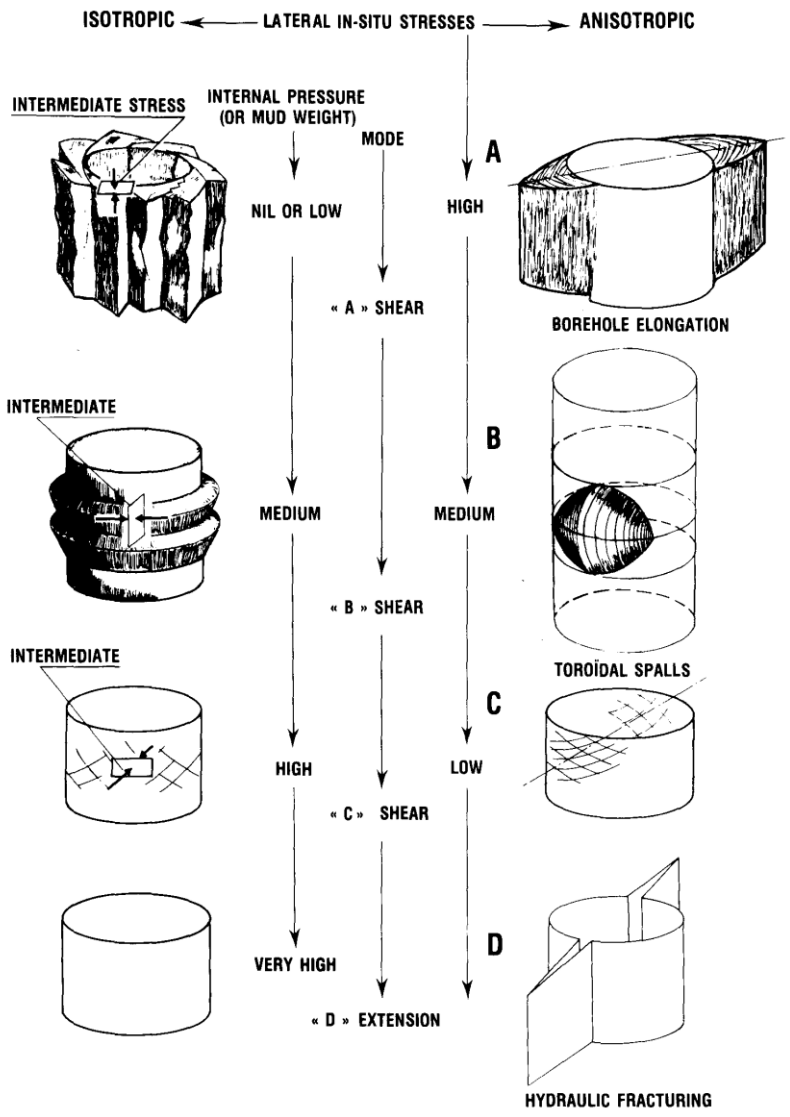

Fig. 1.3. Borehole breakout classification according to Maury and Sauzay (1987).

1.5 Previous Studies on Hydraulic Fracture Containment

In the event the BOP is closed, pressure builds up in the wellbore, and a formation with low fracture gradient can host the fracture path. Depending on the stress regime where

the well is situated, the facture length can grow in the vertical direction, towards the surface (in a strike-slip faulting regime) or in the horizontal plane (in a normal faulting regime). Without shear loading of the borehole, a hydraulic fracture's length propagates in the direction of the intermediate in-situ stress, its height propagates in the direction of the maximum in-situ stress, and its width in the direction of least in-situ stress.

1.6 Research Problem Statements and Objectives

This study aims to answer two major questions on blowout control:

1. Can a blowing well kill itself? In answering this question two hydromechanical frameworks for sand production will be developed. These frameworks are: erosion of damaged/unconsolidated formation and wellbore breakout. For a well to kill itself, it is necessary, but not sufficient, that solid particles be produced. The sizes of cuttings, rate of cuttings production, borehole geometry, and the total energy from the reservoir(s) significantly determine the bridging tendency. Thus, each of these factors will be thoroughly treated in this work.
2. What are the chances of having fracture broaching to the surface/sea bed when the BOP is closed? To answer this question P3D hydraulic fracture model will be used to determine the positions of the fracture tips. To reduce the rigor of modeling fracture propagation in layered media, an effective fracture toughness that homogenizes the different formation layers is developed; similarly, an effective fracture toughness that homogenizes a naturally fractured formation is also proposed; the effective fracture toughness is dependent on area of the discontinuities of a representative volume element and the mechanical properties of the formation matrix.

1.7 Dissertation Layout

This dissertation presents hydromechanical frameworks for predicting self-killing potential of blowing oil and gas wells. For a well to kill itself, sand production is a necessary condition. Two major sources of sand production that are of interest in this study are erosion and wellbore breakout.

Extensive studies have been conducted on type A breakout, but no theoretical development on type B is available in the literature. Thus, Section 2 presents the theoretical development for predicting the morphology of type B breakout. The impact of vertical heterogeneity layout on the morphology of type B breakout mode is also presented. Using shear failure theory and fracture mechanics approach, the failure pattern is shown to be toroidal. While in Section 3 a framework for estimating the size of caving produced during the breakout process is presented. Dipole and beam asymptotic methods are used in deriving the stress intensity factors at the tips of the propagating micro-crack and plate buckling theory is applied to determine the limiting buckling dimensions of the generated slender rock layer produced during the breakout process.

Mathematical frameworks for modeling reservoir and wellbore erosion is presented in Section 4. A comprehensive erosion constitutive relation based on principle of virtual power is presented; this relation reduces to the form of the phenomenological model proposed by Papamichos (2010). I showed that the proposed erosion power balance satisfies the principle of frame indifference if and only if linear and angular momentum balances are satisfied. Furthermore, the three-phase erosion-kinetic equations are presented.

The constitutive behavior of the mixture of gas, liquid, and solid particles produced during the erosion or breakout process needs to be known to adequately predict bridging potential. Considering a deepwter environment, where the temperature contrast at the bottom of the well to the mud-line is high the behavior of the mixture can change as it is transported from the bottom of the well to the surface. Hence, Section 5 presents a thermodynamically consistent multiphase-field model for the flow of the mixture of solid, gas, and liquid during blowout. In this formulation, I added the internal workings in the bulk of the different phases and interfaces due to the internal configurational forces to the first thermodynamics postulate to account for possible evolution of each phase in the continuum. The proposed model

In the event the well is shut in, fracture can initiate and propagate from any of the open-hole interval and broach to the surface. Therefore, Section 6, provide a faster means for estimating the growth of fractures in heterogeneous media during the broaching process. Using equivalent energy-release rate hypothesis, an effective fracture toughness, which homogenizes heterogeneous media, is developed. Finally, conclusions and future works are provided in Section 7.

2. THEORETICAL DEVELOPMENT ON MORPHOLOGY OF WELLBORE TOROIDAL BREAKOUT*

2.1 Scope

Few researchers have conducted experimental investigations on the occurrence of wellbore toroidal breakout; also this breakout mode has been observed in the field. Unfortunately, there is no published theoretical study that adequately describes the occurrence of this unique feature. Thus, we have developed a theory that answers some of the questions related to the occurrence of wellbore toroidal breakout: (a). is the failure mode toroidal? (b). is the deepest depth for a homogeneous and isotropic formation at the center? (c). location of the deepest depth for a heterogeneous formation? To consider the impacts of support pressure on the breakout pattern, the two failure modes were considered, namely: shear fracture and extensile-splitting induced breakouts. Minimum strain energy criterion was used in determining the direction of the propagating extensile cracks; and the trajectories of the cracks were tracked with Fourier series of piece-wise linear functions. In the numerical experiments conducted, it was observed that the extensile cracks propagated in the *r*-*z* plane through mode II (shear) predominantly, and by mode I in the $r-\theta$ plane. By rotating the cracks profile in the r-z plane through the vertical axis by the breakout width, the breakout volume can be approximately determined; the volume generated by this rotation is usually greater than the actual volume.

*Reprinted with permission from Oyedokun, O. and Schubert, J., 2016, June. Theoretical Development on Morphology of Wellbore Toroidal Breakout. In *50th US Rock Mechanics/Geomechanics Symposium*. American Rock Mechanics Association.

2.2 Background on Borehole Breakouts

Extensive studies have been conducted on type- A breakout (Figs.2.1a and 2.1b); the breakout mode is primarily controlled by the tangential stress around the wellbore. Bell and Gough (1982) predicted that breakouts are spalled regions around the wellbore and the deepest depth align with the direction of the minimum horizontal in-situ stress; they envisioned a dog-eared breakout shape. Ewy and Cook (1990), Martin et al. (1994), Ewy et al. (1988) conducted laboratory experiments to confirm Bell and Gough's hypothesis. The triangular breakout section is often observed in some brittle geomaterials, like granite.

But generally, the breakout shapes are flat-bottomed and broad (Zoback et al. 1985); these authors assumed that the breakout shape follows the potential shear failure lines and confirmed their theory with some field observations. Similarly, Kulandar and Dean (1985) and Pollard and Aydin (1988) also supported the curvy nature of the failure surface around the borehole through some observed experiments. Other notable laboratory experiments and field observations that support the curved failure surfaces include the works of Cuss et al. 2003, Stacey and Jongh (1978), and Ortlepp (1978); there are other references that support this hypothesis, which we have not mentioned.

Propagation of shear fractures and/or extensile splitting cracks around the wellbore surface have been attributed to the cause of breakout. Fairhust and Cook (1966) and Horri and Nemat-Nasser (1985) suggested that splitting parallel to the direction of the maximum principal stress is the primary mode of macroscopic fracture of brittle rocks. Similarly, Mastin (1984) proposed that rock failure occurs by the propagation of the

extensional fractures, which initiate from intragranular fractures that extend between contact points of the grains. Many other studies that support the extensile splitting mechanism are Germanovich (1997), Germanovich and Dyskin (1999), Nemat-Nasser, and Horri (1982), Tang and Kou (1998). But Kenemy and Cook (1987), Ewy and Cook (1990), showed that macroscopic shear localization is the dominant failure mechanism around a pressure-supported borehole, while extensile splitting is the dominant failure mechanism around unsupported boreholes.

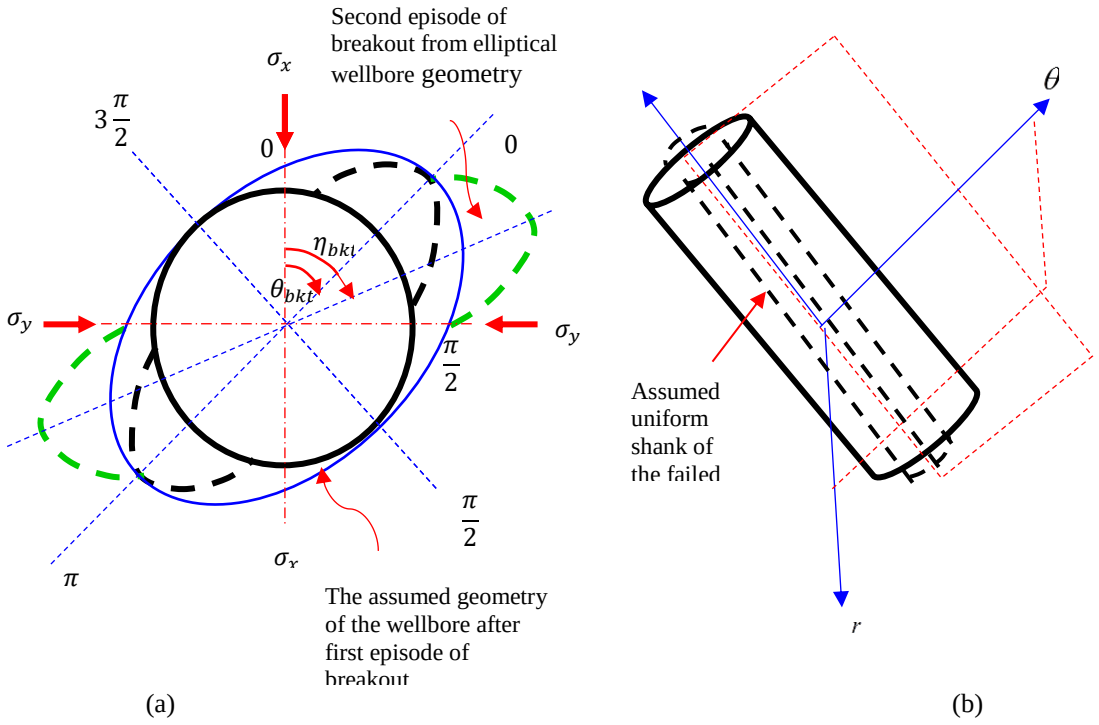

Fig. 2.1 (a). Plane view of the type-A breakout. (b) A 3D view of symmetric type-A breakout along an inclined wellbore.

Different breakout modes have been observed in experiments and the field. But many of the past studies have been centered on symmetric breakout occurrence in the horizontal plane, $r-\theta$ plane. However, Maury and Sauzay (1987), and Guenot and Santarelli (1988) projected that the failure around a borehole when the vertical stress is the maximum principal stress, and the tangential stress is the intermediate will appear as an O-ring (or a torus); this breakout mode is typically named type B according to Guenot.

With pure shear loading of the formation, the first breakout episode will not align with the direction of minimum horizontal insitu stress. For subsequent episodes, the breakout tends to turn forwards (to the right) in the direction of the shear stress; the degree of turning reduces as it approaches the direction of the minimum horizontal in-situ stress.

Maury (1992) later supported this assumption with some field observations. Perie and Goodman (1989) performed laboratory experiments that confirmed Guenot and Maury's projections, while Plump (1989) showed some field observations of the type B breakout. Maloney and Kaiser (1989) observed what seems to be the simultaneous occurrence of type-A and type-B breakouts in laboratory experiments.

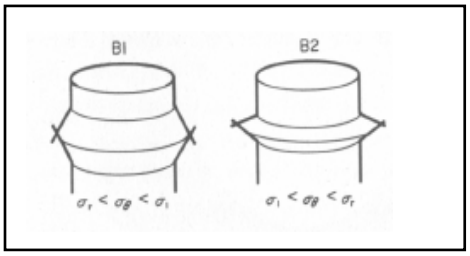

Fig. 2.2. Guenot and Maury's prediction of type-B breakout shape. (Maury 1992).

Based on the projections of Guenot and Maury (Fig. 2.2), and the experiments conducted by Perie and Goodman (Figs. 2.3a, and 2.3b), one may imagine that the deepest depth of type-B breakout will occur at the center of the specimen or the formation layer; it is worth noting that homogeneous samples were used in these experiments. From the field observations presented by Plump (Figs. 2.4a and 2.4b), it is evident that the location of the deepest depth depends on the vertical heterogeneity layout of the formation; and we strongly assume that horizontal planar heterogeneity can cause asymmetric type-A breakout, as observed by Zoback et al. (1985). Therefore, the impact of vertical heterogeneity layout on the morphology of breakouts, especially type-B, is one of the foci of this study.

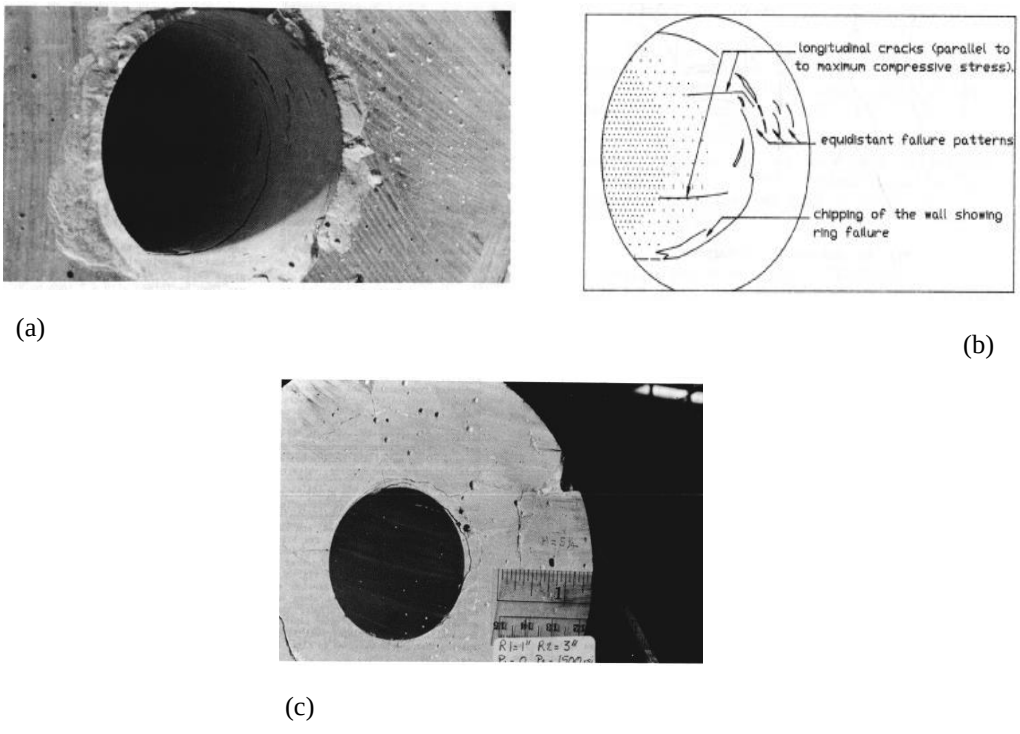

(a)

(b)

(c)

Fig. 2.3 (a) A view of the breakout experiment performed by Perie and Goodman. The failed zones appear as concentric arcs to the borehole. (b). A schematic illustration of the propagating cracks in the breakout experiment (c) A view of the propagating radial cracks and toroidal failure. Reprinted with the permission from ASME. (Perie and Goodman 1989).

Furthermore, we have developed a simple approach of predicting the shape of type-B breakout in heterogeneous formations. Finally, we developed a simple but generic model for estimating the volume of type-B breakouts.

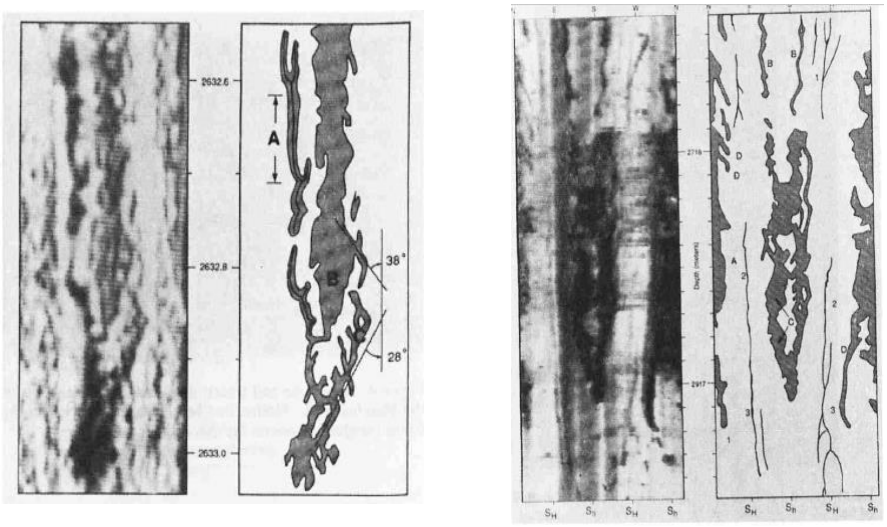

(a) (b)

Fig. 2.4 (a) Detail of the incipient breakout of inclined-segmented margins observed in a particular well located in southern North Sea. (b) Occurrence of different breakout modes in a particular well located in the southern North Sea.. (Plump 1989).

2.3 Theory on Shear Fracture Induced Toroidal Spalling

The dominant failure mechanism around pressure-supported wellbore is compressive shear. In determining the geometry of the breakout region, most authors use the shear failure theory. In this theory, failure occurs when the maximum principal stress at the point of interest exceeds the critical failure stress. From Mohr-Coulomb failure criterion, the failure stress is

$$\sigma_1 = \frac{2C_0 \cos\phi}{1-\sin\phi} + \sigma_3 \frac{1+\sin\phi}{1-\sin\phi} \quad \text{..... (2.1)}$$

For the occurrence of toroidal spalling, the maximum principal stress is the axial stress. To determine the geometry of the failed region, the stress distributions around the wellbore need to be known.

2.4 Stress Distributions Around Wellbore

Using plane strain approximation, the stresses around a circular wellbore are given by these Kirsch's equations:

$$\begin{aligned}\sigma_{rr} &= \frac{1}{2}\left(\sigma_x + \sigma_y\right)\left(1 - {r_D}^2\right) + \\ &\frac{1}{2}\left(\sigma_x - \sigma_y\right)\left(1 + 3{r_D}^4 - 4{r_D}^2\right)\cos 2\theta \\ &+ \sigma_{xy}\left(1 + 3{r_D}^4 - 4{r_D}^2\right)\sin 2\theta + {r_D}^2\left(p_w - p_0\right) \\ &+ \sigma_T\end{aligned} \quad \text{..... (2.2)}$$

$$\begin{aligned}\sigma_{\theta\theta} &= \frac{1}{2}\left(\sigma_x + \sigma_y\right)\left(1 + {r_D}^2\right) \\ &- \frac{1}{2}\left(\sigma_x - \sigma_y\right)\left(1 + 3{r_D}^4\right)\cos 2\theta \\ &- \sigma_{xy}\left(1 + 3{r_D}^4\right)\sin 2\theta - {r_D}^2\left(p_w - p_0\right) - \sigma_T\end{aligned} \quad \text{..... (2.3)}$$

$$\sigma_{r\theta} = \left\{\begin{array}{l}\left[\frac{1}{2}\left(\sigma_x - \sigma_y\right) + \sigma_{xy}\cos 2\theta\right] \\ \left(1 - 3{r_D}^4 + 2{r_D}^2\right)\end{array}\right\} \quad \text{..... (2.4)}$$

$$\begin{aligned}\sigma_z &= \sigma_{zz} - 2\nu\left(\sigma_x - \sigma_y\right){r_D}^2\cos 2\theta \\ &- 4\nu{r_D}^2\sigma_{xy}\sin 2\theta - \sigma_T\end{aligned} \quad \text{..... (2.5)}$$

$$\sigma_{\theta z} = \left[-\sigma_{xz} \sin\theta + \sigma_{yz} \cos\theta \right] \left(1 + {r_D}^2 \right) \quad \text{..... (2.6)}$$

Noting that $r_D = \frac{a}{r}$; where a is the radius of the wellbore and r is any radial distance from the center of the hole. For an elliptic wellbore, the stress distributions around the borehole are derived assuming small deformation; the stresses due to mechanical-polyaxial and thermal loadings of an elliptic hole in an infinite medium are

$$\sigma_{\varsigma\varsigma} = \sigma_{\varsigma\varsigma}^{(1)} + \sigma_{\varsigma\varsigma}^{(2)} + \sigma_{\varsigma\varsigma}^{(3)} + \sigma_{\varsigma\varsigma}^{(4)} + \sigma_{\varsigma\varsigma}^{(5)} - \sigma_T \quad \text{..... (2.7)}$$

$$\sigma_{\eta\eta} = \sigma_{\eta\eta}^{(1)} + \sigma_{\eta\eta}^{(2)} + \sigma_{\eta\eta}^{(3)} + \sigma_{\eta\eta}^{(4)} + \sigma_{\eta\eta}^{(5)} + \sigma_T \quad \text{..... (2.8)}$$

$$\sigma_{\varsigma\eta} = \sigma_{\varsigma\eta}^{(1)} + \sigma_{\varsigma\eta}^{(2)} + \sigma_{\varsigma\eta}^{(3)} + \sigma_{\varsigma\eta}^{(4)} + \sigma_{\varsigma\eta}^{(5)} - \sigma_T \quad \text{..... (2.9)}$$

$$\sigma_z = \sigma_{zz} + \nu\left(\sigma_{\varsigma\varsigma} + \sigma_{\eta\eta} \right) - \sigma_T \quad \text{..... (2.10)}$$

$$4\left(\sigma_{\varsigma\varsigma}^{(j)} - i\sigma_{\varsigma\eta}^{(j)}\right) =$$

$$\sigma_{m_j}\left\{e^{2\varsigma_0}\cos 2\left(\beta + k_j\right) + \left(1 - e^{2\varsigma_0 + i2\left(\beta + k_j\right)}\right)\coth\xi\right\}$$

$$+\sigma_{m_j}\left\{\begin{matrix} e^{2\varsigma_0}\cos 2\left(\beta + k_j\right) + \left(1 - e^{2\varsigma_0 - i2\left(\beta + k_j\right)}\right) \\ \coth\left(2\varsigma_0 - \xi\right)\end{matrix}\right\}$$

$$+\sigma_{m_j}\coth\left(2\varsigma_0 - \xi\right)\left\{\left(1 - e^{2\varsigma_0 + i2\left(\beta + k_j\right)}\right)\cos ech^2\xi\right\}$$

$$+\sigma_{m_j}\cos ech\left(2\varsigma_0 - \xi\right)\left\{-\left(\cosh 2\varsigma_0 - \cos 2\left(\beta + k_j\right)\right)\coth\xi\cos ech\,\xi\right.$$

$$\left.\begin{matrix} +2e^{2\varsigma_0}\cosh 2\left(\xi - \varsigma_0 - i\left(\beta + k_j\right)\right)\cos ech\,\xi \\ -e^{2\varsigma_0}\sinh 2\left(\xi - \varsigma_0 - i\left(\beta + k_j\right)\right)\cos ech\,\xi\coth\xi\end{matrix}\right\} \quad \text{..... (2.11)}$$

Where,

$$\sigma_{\varsigma\varsigma}^{(j)} + \sigma_{\eta\eta}^{(j)}$$

$$= \mathrm{Re}\left\{\sigma_{m_j}\left\{\begin{matrix} e^{2\varsigma_0}\cos 2\left(\beta + k_j\right) + \\ \left(1 - e^{2\varsigma_0 + i2\left(\beta + k_j\right)}\right)\coth\xi\end{matrix}\right\}\right\} \quad \text{..... (2.12)}$$

$$\xi = \zeta + i\eta \quad \text{..... (2.13)}$$

$$\sigma_T = \frac{E}{2(1-\nu)}\Delta T = \frac{E}{2(1-\nu)}\left(T_m - T_f\right) \quad \text{..... (2.14)}$$

For $j = 1$

$$\left.\begin{aligned} k_j &= 0 \\ \sigma m_j &= \sigma y \end{aligned}\right\} \quad \text{.....(2.15)}$$

For $j = 2$

$$\left.\begin{aligned} k_j &= \frac{\pi}{2} \\ \sigma m_j &= \sigma x \end{aligned}\right\} \quad \text{.....(2.16)}$$

For $j = 4$

$$\left.\begin{aligned} k_j &= \frac{\pi}{4} \\ \sigma m_j &= \sigma xy \end{aligned}\right\} \quad \text{.....(2.17)}$$

For $j = 5$

$$\left.\begin{aligned} k_j &= 3\frac{\pi}{4} \\ \sigma m_j &= -\sigma xy \end{aligned}\right\} \quad \text{.....(2.18)}$$

When $j = 3$, the hoops and the hyperbolic stresses are equal to the effective wellbore pressure.

2.5 Breakout Pattern Under Shear Fracture

During the rupture process, the breakout is formed by the simultaneous propagation of shear fractures both in the *r-z* and *r-θ* planes (Fig.2.5). The shear fractures in the *r-z* plane are parallel to each other (for each conjugate), but acute to the wellbore; the acuteness of the angle depends on the rock material. The stronger the rock, the more acute the angle. The acute angle is the called the fracture angle, ψ .

As the shear fractures propagate away from the wellbore wall into the formation, the conjugate shear fractures intersect at a location. The intersecting location is where the breakout has the deepest depth. For a homogeneous and isotropic formation, the conjugate shear fractures intersect at the center because the fracture angles are equal (Fig.2.6). But

when the formation is highly heterogeneous the intersecting point depends on the heterogeneity layout of the formation (Figs. 2.7a and 2.7b). Since breakout depth tends to increase with the magnitudes of the stress components acting near the wellbore, the vertical heterogeneity layout can also affect the magnitude of the deepest depth.

The failure in the r-θ plane determines the magnitude of the breakout width, although it is greatly controlled by the magnitude of the axial stress (for a vertical wellbore). The span of the failed zone depends greatly on the fracture angle(s). And the region bounded by the failure planes defines the shape of the breakout; the region is always toroidal.

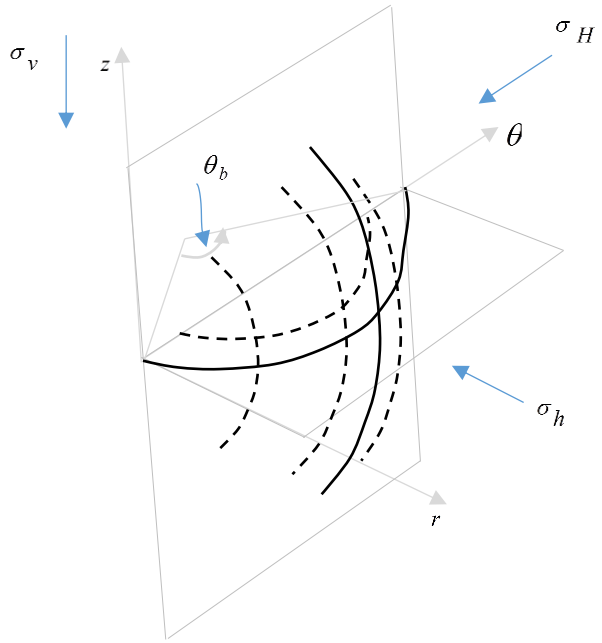

Fig.2.5. Longitudinal and radial shear fractures propagation.

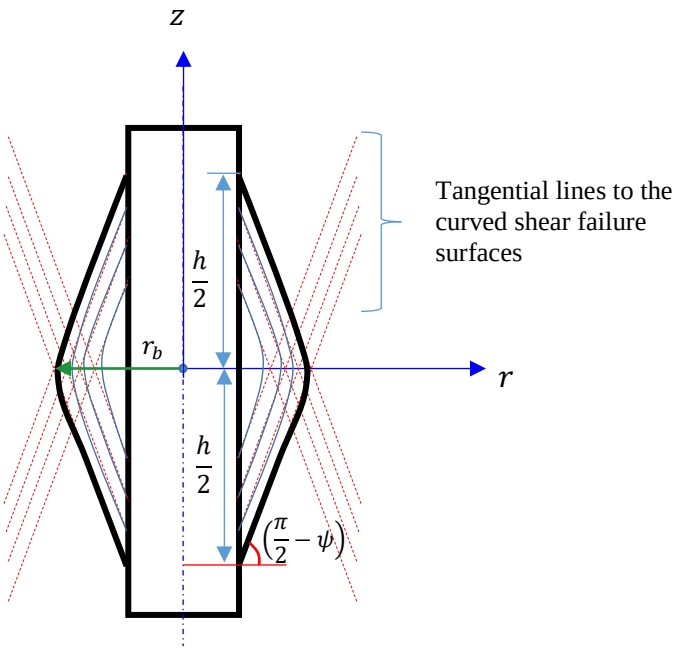

Fig.2.6. Shear fractures in the r-z plane for a homogeneous formation. The deepest depth occurs at the center of the formation.

Knowing the vertical heterogeneity layout of the formation or laboratory specimen, the location of the deepest breakout depth can be estimated by projecting straight lines, inclined to the borehole axis; the inclination angle is equal to the fracture angle.

From Mohr circle, the fracture angle is equal to

$$\psi = \frac{\pi}{4} - \frac{\phi}{2} \quad \text{.....(2.19)}$$

The intersection of these projected lines will give an approximate location of the deepest depth; then knowing the state of stress at that location, the breakout depth and width can be estimated. This approach reduces the number of computations needed to determine the breakout geometry.

In the following examples the fracture angle, Eq. (2.19), gives a good approximation of the inclination of the curvy shear failure lines at the wellbore interface.

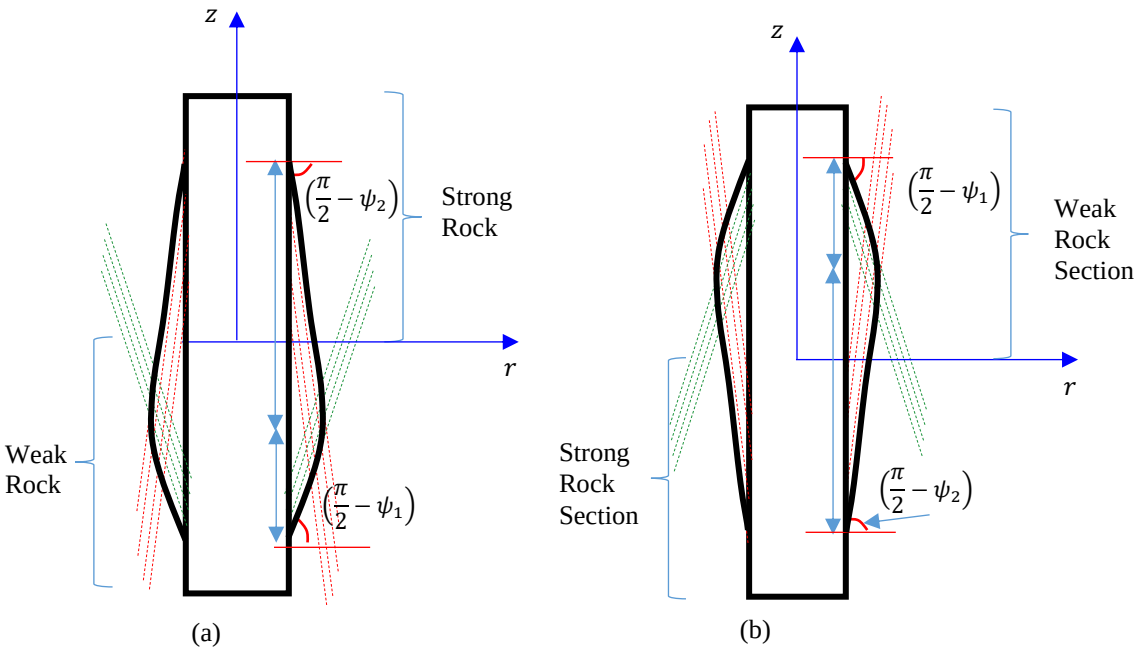

Fig.2.7. (a) Shear fractures in the r-z plane for a heterogeneous formation. The deepest depth occurs at a deeper location when the stronger zone is at the top of a weaker zone. (b) Shear fractures in the r-z plane for a heterogeneous formation. The deepest depth occurs at a shallower location when the weak zone is at top of a stronger zone.

2.6 Breakout Depth and Width

Knowing the location of the deepest depth, through the procedure given above, the breakout depth is calculated by first knowing the azimuth of the maximum compression. The azimuth of maximum compression aligns with the direction of the minimum horizontal in-situ stress, if the wellbore is vertical and its axes align with axes of the principal in-situ stresses.

When the wellbore axes are not aligned with the axes of the principal in-situ stresses, the direction of maximum compression can be determined by finding the angle that maximizes the hoops stress. In such a case, especially along inclined wells, the breakout episodes typically appear as shown in Fig.2.1a.

With the direction of the maximum compression known, the angle is substituted into the stress equations, Eq. (2.2) to Eq. (2.6) for circular wellbore geometry or Eq. (2.7) to Eq. (2.10) for elliptical wellbore geometry and the corresponding radial distance that makes the maximum principal stress equal to the critical failure stress at the point is calculated. This radial distance is the deepest breakout depth

For an elliptical wellbore geometry, the radial distance is calculated using the conversion equation

$$r_{b,k} = \frac{1}{\cos\left(\theta_{bt,k-1} - \theta_{bt,k}\right)} \sqrt{\frac{r_{b,k-1}^2 - r_{m,k-1}^2}{1 - \left(\tanh \varsigma_B\right)^2}} \quad \text{..... (2.20)}$$

$k = 1, 2 \ldots$ is the breakout episode. ς_B is the breakout depth in elliptical coordinate system, calculated through the procedure described earlier. When k is 1, the wellbore geometry prior to rupture is used. $\theta_{bt,k}$ is the direction of the maximum compression at breakout episode k. $r_{m,k}$ is the breakout depth in the direction of minimum compression. In some cases, the toroidal spalls appear in the direction of minimum compression; thus, the direction of minimum compression should be used in lieu of the maximum compression in the calculations.

At the wall of a circular wellbore, the stresses are

$$\sigma_{rr,w} = \left(p_w - p_0\right) \quad (2.21)$$

$$\sigma_{\theta\theta,w} = \left(\sigma_x + \sigma_y\right) - 2\left(\sigma_x - \sigma_y\right)\cos 2\theta - 4\sigma_{xy}\sin 2\theta - \left(p_w - p_0\right) \quad (2.22)$$

$$\sigma_{r\theta,w} = 0 \quad (2.23)$$

$$\sigma_{z,w} = \sigma_{zz} - 2\nu\left(\sigma_x - \sigma_y\right)\cos 2\theta - 4\nu\sigma_{xy}\sin 2\theta \quad (2.24)$$

$$\sigma_{\theta z} = 2\left[-\sigma_{xz}\sin\theta + \sigma_{yz}\cos\theta\right] \quad (2.25)$$

And the effective principal stresses are:

$$\sigma_1 = \frac{1}{2}\left\{\begin{array}{l}\left(\sigma_{z,w} + \sigma_{\theta\theta,w}\right) \\ + \sqrt{\left(\sigma_{\theta\theta,w} - \sigma_{z,w}\right)^2 + 4\sigma_{\theta z,w}{}^2}\end{array}\right\} \quad (2.26)$$

$$\sigma_2 = \frac{1}{2}\left\{\begin{array}{l}\left(\sigma_{z,w} + \sigma_{\theta\theta,w}\right) \\ - \sqrt{\left(\sigma_{\theta\theta,w} - \sigma_{z,w}\right)^2 + 4\sigma_{\theta z,w}{}^2}\end{array}\right\} \quad (2.27)$$

$$\sigma_3 = \left(p_w - p_0\right) \quad (2.28)$$

By equating the Eq. (2.26) and Eq. (2.1) the breakout width can be estimated. For vertical wellbores, the breakout width, θ_b, is

$$\theta_b = \frac{1}{2}\left\{\cos^{-1}\left(\frac{C}{\lambda}\right) - \omega\right\} \quad (2.29)$$

Where,

$$C = \sigma_x + \sigma_y$$
$$-\frac{2C_0 + (p_w - p_0)\left\{\sqrt{1+\mu^2}+\mu\right\}}{\sqrt{1+\mu^2}+\mu} - p_w - p_0 \quad \text{..... (2.30)}$$

$$\lambda = \sqrt{\left[\sigma_{zz} - 2\nu\left(\sigma_x - \sigma_y\right)\right]^2 + 16{\sigma_{xy}}^2} \quad \text{..... (2.31)}$$

$$\omega = \tan^{-1}\left\{\frac{4\sigma_{xy}}{\left[\sigma_{zz} - 2\nu\left(\sigma_x - \sigma_y\right)\right]}\right\} \quad \text{..... (2.32)}$$

And for an elliptical wellbore, the effective stresses at the wall are:

$$\sigma_{\eta\eta,w} = (p_w - p_0) \quad \text{..... (2.33)}$$

$$\sigma_{\varsigma\varsigma,w} = \begin{Bmatrix} (\sigma_x - \sigma_y)\cos 2\beta \\ +(p_w - p_0)\cos 2\eta - (p_w - p_0)\cosh 2\varsigma_0 \\ +2\sigma_{xy}\sin 2\beta + e^{2\varsigma_0}\left[\left(-\sigma_x + \sigma_y\right)\right]\cos 2(\beta - \eta)\Big\}^{\frac{1}{A}} \\ -2\sigma_{xy}\sin 2(\beta - \eta) + (2p_0 - \sigma_x - \sigma_y)\sinh 2\varsigma_0 \end{Bmatrix} \quad \text{..... (2.34)}$$

$$A = \frac{1}{\cos 2\eta - \cosh 2\varsigma_0} \quad \text{..... (2.35)}$$

$$\sigma_{\varsigma\eta,w} = 0 \quad \text{..... (2.36)}$$

$$\sigma_{z,w} = \sigma_{zz} + \nu(\sigma_{\eta\eta,w} + \sigma_{\varsigma\varsigma,w}) \quad \text{..... (2.37)}$$

Similarly, the breakout width around an elliptic wellbore is estimated through Eq. (2.38).

$$\theta_b = \frac{1}{2}\left\{\cos^{-1}\left(\frac{C}{\lambda}\right) - \omega\right\} \quad \text{..... (2.38)}$$

Where,

$$C = \sigma_{\varsigma\varsigma}{}^{c}\cosh 2\varsigma_0 + \nu\Big[\big(\sigma_x - \sigma_y\big)\cos 2\beta$$
$$-\big(p_{wc} - p_0\big)\cosh 2\varsigma_0 + 2\sigma_{xy}\sin 2\beta \Big] \quad \text{..... (2.39)}$$
$$+\Big(2p_0 - \sigma_x - \sigma_y\Big)\sinh 2\varsigma_0 - \sigma_{zz}\cosh 2\varsigma_0\Big]$$

$$\lambda = \sqrt{D^2 + B^2} \quad \text{..... (2.40)}$$

$$D = \sigma_{\varsigma\varsigma}{}^{c} - \sigma_{zz} + (1-\nu)\big(p_w - p_0\big)$$
$$+\nu e^{2\varsigma_0}\Big(\sigma_x - \sigma_y\Big)\cos 2\beta \quad \text{..... (2.41)}$$
$$+2\nu e^{2\varsigma_0}\sigma_{xy}\sin 2\beta$$

$$B = \nu e^{2\varsigma_0}\Big(\sigma_x - \sigma_y\Big)\sin 2\beta \quad \text{..... (2.42)}$$
$$-2\nu e^{2\varsigma_0}\sigma_{xy}\cos 2\beta$$

$$\omega = \tan^{-1}\left\{\frac{B}{D}\right\} \quad \text{..... (2.43)}$$

It should be noted that β is the breakout direction at episode *k-1*. $\sigma_{\tau\varsigma}{}^{c}$ is the critical failure stress.

2.7 Numerical Example of Type-B Breakout Pattern in a Homogeneous Formation

Considering a vertical well drilled in a normal faulting regime and its axes aligning with the orientations of the in-situ principal stresses; the cohesive strength of the rock is

Differential Depth (m)	σ_v (MPa)	σ_H (MPa)	σ_h (MPa)	r_b (m)	θ_b (rad)
0.000	87.73	29.24	26.14	0.1989	1.385
3.048	87.79	29.26	26.26	0.2062	1.354
6.096	87.86	29.29	26.56	0.23758	1.387
9.144	87.93	29.31	26.68	0.2540	1.347
12.192	88.00	29.33	26.81	0.2800	1.317
15.240	88.07	29.36	27.02	0.37099	1.312
18.288	88.14	29.38	27.10	0.4312	1.263
21.336	88.21	29.40	27.31	0.0922	1.256
24.384	88.28	29.43	27.38	0.09248	1.272
27.432	88.34	29.45	27.45	0.09275	1.153

Table 2.1. Breakout Depth and Width Variation with Depth.

Differential Depth (m)	$\theta_b/2$ (rad)	ψ (rad)
0.000	0.6925	0.5236
3.048	0.677	0.5236
6.096	0.6935	0.5236
9.144	0.6735	0.5236
12.192	0.6585	0.5236
15.240	0.656	0.5236
18.288	0.6315	0.5236
21.336	0.628	0.5236
24.384	0.636	0.5236
27.432	0.5765	0.5236

Table 2.2. Comparison between Fracture Angle Calculated from Mohr Circle and Inclination Angle of the Failure Lines at Wellbore Interface.

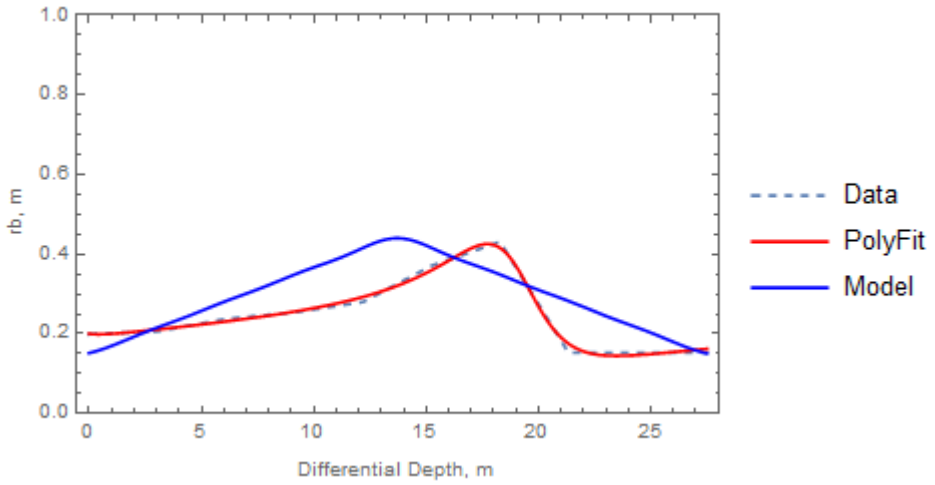

Fig. 2.8. Using the rational polynomial in fitting the data above. The solid orange line is the polynomial fit, while the dashed line is the data. The projected line is the solid blue line.

13.788 MPa (2000 psi), the Poisson ratio is 0.25, and the angle of internal friction is $\pi/6$ rad. The wellbore radius is 0.09144 m. (0.3ft.)

Despite the use of the rational polynomial, the fit is not good; but it is still a reasonable representation of the breakout pattern. Mohr-Coulomb failure criterion was used in estimating the breakout geometry and it is expected that the dimensions of the breakout may be larger than that predicted with Mogi-Coulomb failure criterion (Al-Ajmi and Zimmerman 2006). Despite this shortcoming, the breakout patterns estimated with the two criteria will look alike; the primary aim of this study is to confirm the assumed breakout pattern. Rational polynomials are known to fit any arbitrary data very well; thus using the polynomial function:

$$f(z)=\frac{a_0+a_1z+a_2z^2+a_3z^3+a_4z^4+a_5z^5}{1+b_1z+b_2z^2+b_3z^3+b_4z^4+b_5z^5} \quad \text{.....(2.44)}$$

To construct the triangular breakout pattern that locates the depth of maximum breakout, Fourier series is used:

$$f(z)=\begin{cases} z\tan\psi_1 & 0<z<a_m \\ (L-z)\tan\psi_2 & a_m<z<L \end{cases} \quad \text{..... (2.45)}$$

$$a_m=\frac{L\tan\psi_2}{\tan\psi_1+\tan\psi_2} \quad \text{..... (2.46)}$$

Where, L is the thickness of the formation or length of the laboratory specimen:

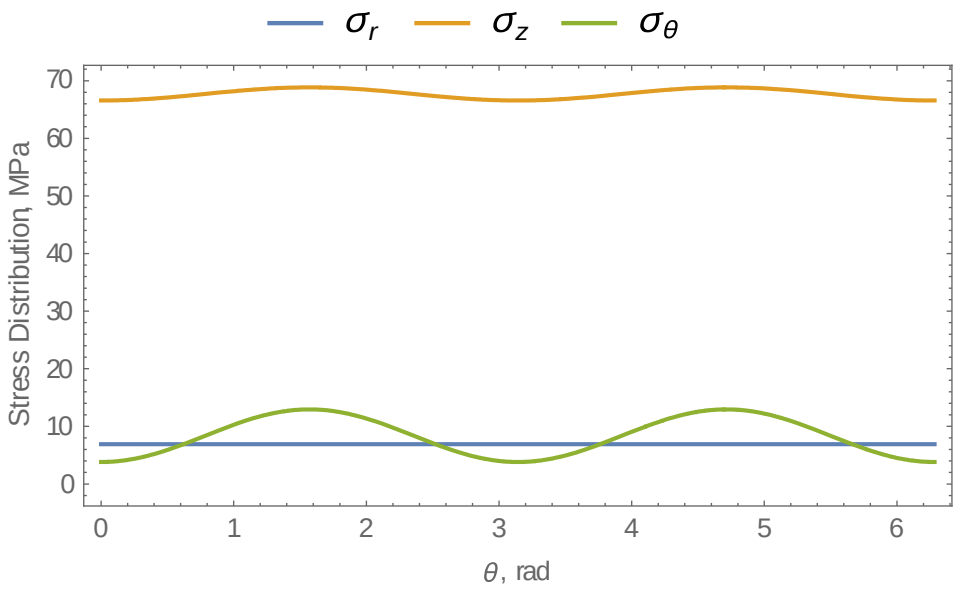

Fig. 2.9. Effective stress distribution at the wellbore wall. It is evident from the plot that breakout direction is at the azimuth of minimum horizontal in-situ stress.

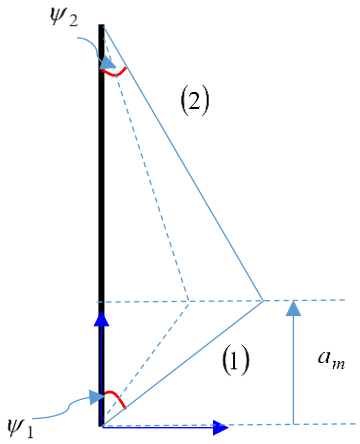

Fig. 2.10. A schematic illustration of the projected straight lines. After determining the maximum break depth location with the fracture angle, the dashed lines illustrate the adjusted projection lines.

The Fourier coefficients are:

$$a_0 = \frac{{a_m}^2 \tan\psi_1 + (L - a_m)^2 \tan\psi_2}{2L} \quad \text{..... (2.47)}$$

$$a_n = \frac{1}{2\pi^2 n^2}\left\{\left(L\left(\cos\left(\frac{a_m \pi n}{L}\right) - 1\right)\right.\right.$$

$$\left.\left. + a_m \pi n \sin\left(\frac{a_m \pi n}{L}\right)\right)\tan\psi_1 + (-L\cos(n\pi)\right. \quad \text{..... (2.48)}$$

$$\left. + L\cos\left(\frac{a_m \pi n}{L}\right) - (L - a_m) n\pi \sin\left(\frac{a_m \pi n}{L}\right)\right)\tan\psi_2\Bigg\}$$

$$b_n = \frac{1}{\pi^2 n^2}\{-L\sin(n\pi)\tan\psi_2$$
$$+L\sin\left(\frac{a_m\pi n}{L}\right)\left(\tan\psi_1+\tan\psi_2\right) \quad \text{..... (2.49)}$$
$$-n\pi\cos\left(\frac{a_m\pi n}{L}\right)\left(a_m\tan\psi_1-(L-a_m)\tan\psi_2\right)\}$$

The Fourier series representing the projected breakout pattern is

$$f(z)=a_0+\sum_{n=1}^{\infty}a_n\cos\left(\frac{zn\pi}{L}\right)+b_n\sin\left(\frac{zn\pi}{L}\right) \quad \text{..... (2.50)}$$

2.8 Numerical Example of Type-B Breakout Pattern in a Heterogeneous Formation

In this case, the formation strength is decreasing with depth, the variations of the rock properties with depth are shown in Table 3;

$$\phi=\frac{\pi}{6}-j\frac{\pi}{100} \quad \text{.....(2.51)}$$

the internal friction angle decreases with depth according to Eq. (2.51). The well inclination angle is 22.5^0; the overburden remains the same as in Table. 1.

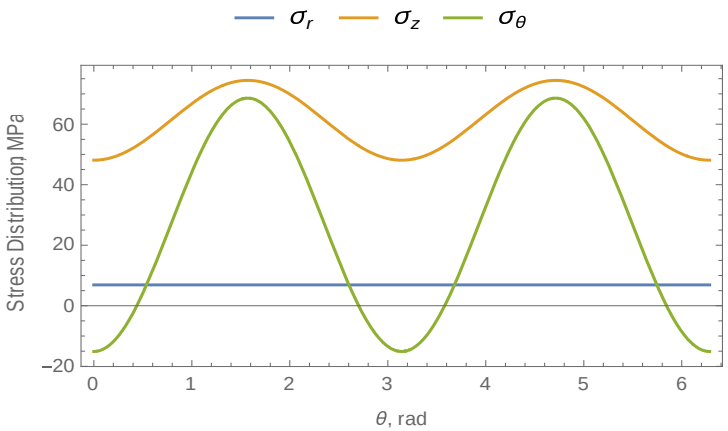

Fig. 2.11. Effective stress distributions at the wellbore wall.

Differential Depth (m)	σ_H (MPa)	σ_h (MPa)	ν	C_0 (MPa)	r_b (m)	θ_b (rad)
0.000	29.53	26.29	0.25	18.62	0.091	0.329
3.048	31.15	26.40	0.24	17.93	0.091	0.348
6.096	32.82	26.49	0.23	17.24	0.091	0.395
9.144	34.54	26.64	0.22	16.55	0.091	0.422
12.192	36.30	26.84	0.21	15.86	0.094	0.446
15.240	39.96	26.90	0.20	15.17	0.100	0.873
18.288	40.93	27.04	0.19	14.48	0.403	0.727
21.336	41.35	27.31	0.18	13.79	0.237	0.595
24.384	41.95	27.38	0.17	13.10	0.145	0.57
27.432	43.94	27.45	0.16	12.41	0.127	0.53

Table 2.3. Breakout Depth and Width Variation with Depth.

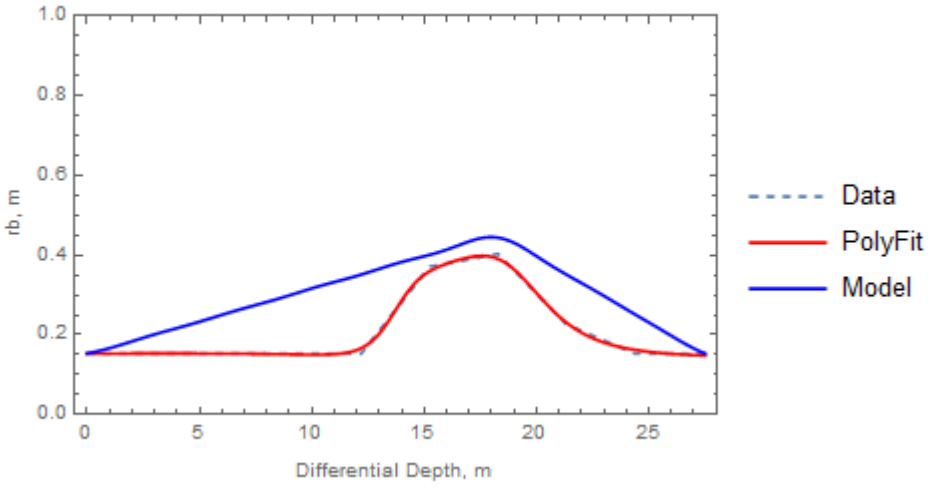

Fig. 2.12. The area under the projected-lines over estimates the volume of sand produced.

2.9 Theory on Extensile Fracture Induced Toroidal Spalling

Kenemy and Cook (1990) and Ewy and Cook (1990) showed that macroscopic splitting is the dominant mode of failure around unsupported or poorly supported borehole. And Jaeger and Hoskins (1966) had shown earlier that this mode of failure is independent of the loading direction (tensile or compressive loading). Failure by extensile splitting starts by the growth of micro cracks (transgranular fracture propagation or disintegration of the grain boundaries), breaking of the cementation between the sand grains or the growth of an existing crack in the rock.

The criterion on which the cracks propagate around the wellbore has received a lot of contributions. Erdogan and Sih (1963), Besterfield et al. (1990), Chang and Mear (1995), Porterla and Aliabadi (1991) assumed that the cracks will tend to extend in the direction perpendicular to the maximum principal stress. Sih (1973) assumed that the crack will propagate along the path that minimizes the potential energy density. The paths taking by these two criteria are almost similar as shown by the experiments performed by Erdogan and Sih. Other criteria include local symmetry (Stone and Babuska 1997) and maximum energy release rate.

But the impact of material properties on the fracture path has been suppressed in the maximum principal stress criterion. Therefore, the minimum potential energy criterion will be used in this analysis.

For breakout to occur, many extensile cracks will need to propagate simultaneously. To reduce the complexity, the dynamic forces associated with the interaction and motions of these cracks have been suppressed. Also, we assumed that each

of the cracks propagate through one end only. And the longitudinal and radial cracks propagate in their respectively planes without any intra-planar interactions.

2.10 Breakout Pattern Under Extensile Splitting

Far away from the wellbore wall, the stress intensity factors (modes I and II) are small, such that the cracks located in that region will not propagate, for a given loading condition. As the wellbore geometry changes, the stress state around the hole changes also. Consequently, the stress intensity factors distributions around the borehole are altered as well.

The initial cracks generated concentrate at the azimuth of maximum compression and propagate towards the wellbore wall. This propagation path is as a result of the stress distributions around the wellbore; the cracks want to propagate with minimum strain energy.

Considering cracks *A* and *B* in Fig. 2.13a, located at distance x_h from the wellbore wall; and they are the set of cracks satisfying the lower bound of $\sigma_{rr}{}^{c} \geq \frac{0.1l_0}{2x_h}\sigma_{\theta\theta}$; where l_0 is the original length of the crack. This simply means that the unstable crack growth is suppressed at this location (Germanovich and Dyskin 2000). Therefore, the sets of these cracks give the location of the deepest breakout depth in the $r-\theta$ plane. And the intersections of the cracks' paths with the borehole boundary yield the breakout width (Fig. 2.13c).

Similarly, in the *r-z* plane, the intersection of the paths of the propagating cracks C and D (Fig 13b) with the wellbore wall define the height of the failed region. And cracks C and D also satisfy the lower bound $\sigma_{rr}{}^{C} \geq \frac{0.1l_0}{2z_h}\sigma_z$.

The tangential stress at location (1) in Fig. 2.13a, is greater than that at location (2), therefore, the tendency for cracks to extend towards the wellbore is evident. Conversely, the radial stress at (1) is less than that at (2), thus, the tendency for the unstable extension of cracks close to (1) to be suppressed is limited; although, cracks tend to propagate with more stability close to the wellbore wall (Germanovich and Dyskin 2000).

In the same vein, the axial stress driving the growth of the longitudinal cracks is greater at location (1) than at (2) (Fig. 2.13b). While the axial stress at (3) is greater than that at (1). With this in mind, the reader can have a preliminary view of the paths the longitudinal cracks can take.

The interactions among the multitude of cracks generated in each plane is not as severe as the interaction between the cracks and the borehole interface, especially in the $r-\theta$ plane. But these interplays are averaged and the dipole asymptotic method is mostly used to capture the interaction between the borehole and the representative crack (Freij-Ayoub 1996 and Germanovich and Dyskin 2000).

Using the dipole asymptotic method, Germanovich and Dyskin derived the stress intensity factor for the mode I propagation of cracks A and B in the $r-\theta$ plane as

$$K_{I,r\theta} = \frac{2\sqrt{\pi}}{\sqrt{R_c \sin\delta\,(3-\cos\delta)}}\left\{(F+\Delta F)\frac{3\cos\delta-1}{2\pi}\right.$$
$$\left.-(\sigma_{rr}+\Delta\sigma_{rr})R_c \sin\delta\cos\frac{\delta}{2}\right\} \quad \text{.....(2.52)}$$

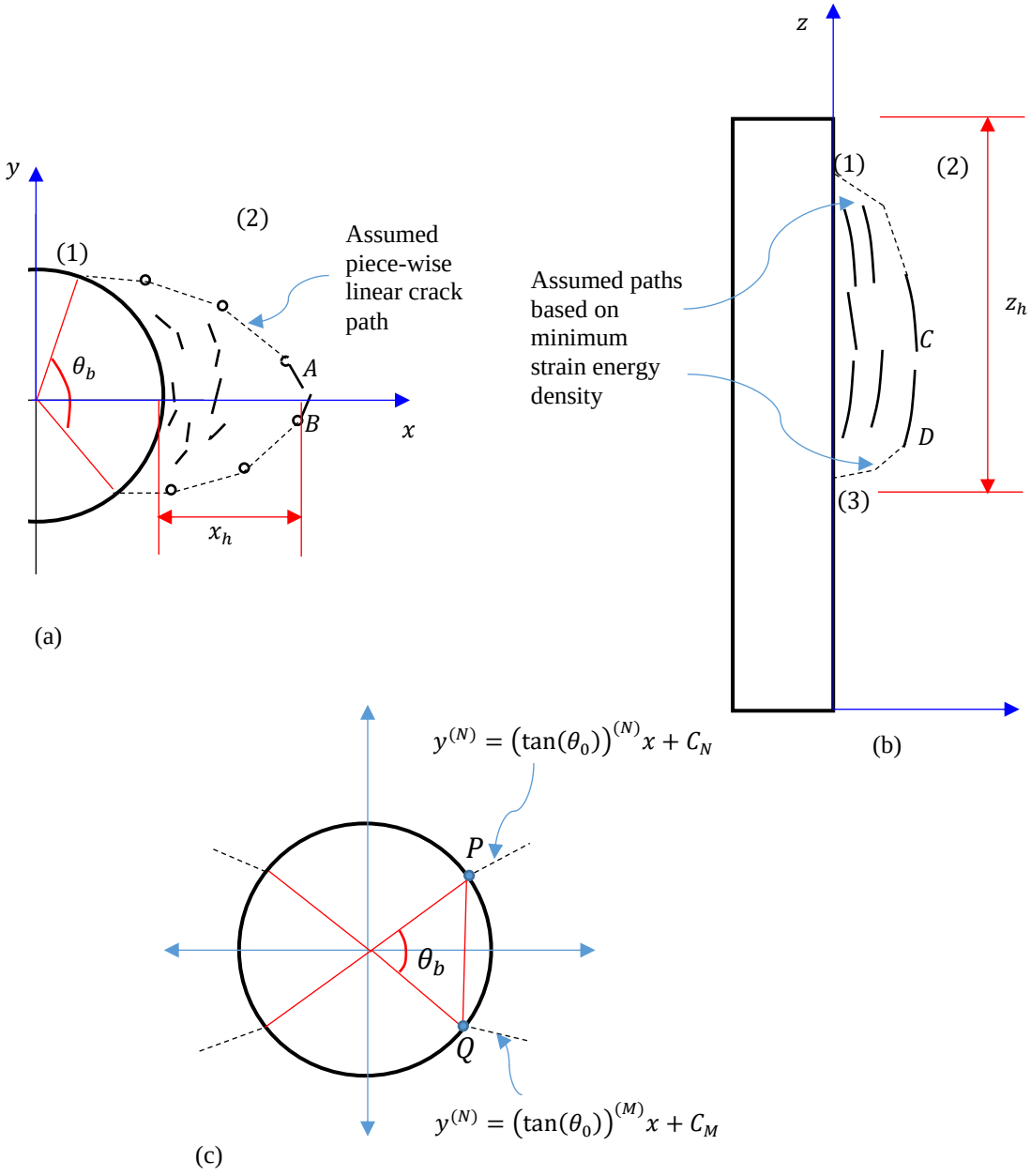

Fig. 2.13. (a) A schematic representation of the radial crack path. It is assumed that symmetric deformation occurs at the other end of the borehole. (b) A schematic representation of the longitudinal cracks' paths. The cracks are located at the azimuth of maximum compression. (c) The intersections of the last line segments with the borehole geometry (points P and Q) yield the breakout width. This is done by solving a system of algebraic equations.

Where,

$$F+\Delta F=l_0\{(\sigma_{\theta\theta}+\Delta\sigma_{\theta\theta})-(\sigma_{rr}+\Delta\sigma_{rr})\}\frac{2}{3\pi} \quad \text{..... (2.53)}$$

and,

$$\sigma_{\theta\theta}+\Delta\sigma_{\theta\theta}=\frac{1}{2\left(m-\xi_h{}^2\right)^3}\left\{2\xi_h{}^6+\begin{bmatrix}\left(1+\lambda_{r\theta}\right)\left(m^2+1\right)\\-2\left(2-\lambda_{r\theta}\right)m\end{bmatrix}\xi_h{}^4\right.$$

$$+\left[\left(-5\lambda_{r\theta}-1\right)m^2+3+\left(\lambda_{r\theta}+1\right)m^3+\left(7\lambda_{r\theta}-5\right)m-3\lambda_{r\theta}\right]\xi_h{}^2 \quad \text{..... (2.54)}$$

$$\left.\left(1+\lambda_{r\theta}\right)m^3-\left(1-\lambda_{r\theta}\left(m-2m^2\right)\right)\right\}$$

$$\sigma_{rr}+\Delta\sigma_{rr}=\frac{1-\xi_h{}^2}{2\left(m-\xi_h{}^2\right)^3}\left\{2\xi_h{}^4+\begin{bmatrix}-\left(1+\lambda_{r\theta}\right)m^2+2m\\+3\left(1-\lambda_{r\theta}\right)\end{bmatrix}\xi_h{}^2\right. \quad \text{..... (2.55)}$$

$$\left.-\left(\lambda_{r\theta}+1\right)m^3-2\left(1-\lambda_{r\theta}\right)m^2+\left(1-\lambda_{r\theta}\right)m\right\}$$

$$\left.\begin{aligned}&m=\frac{a-b}{a+b};\\&\xi_h=\frac{1}{2}\left[c+\sqrt{c^2-4m}\right];\\&c=1+m+\frac{x}{R};\\&R=\frac{a+b}{2};\\&\lambda_{r\theta}=\frac{\sigma_h}{\sigma_H}\\&\delta=\frac{l}{R_C}\end{aligned}\right\} \quad \text{..... (2.56)}$$

and for C and D in the $r-z$ plane, the mode I stress intensity factor is

$$K_{I,rz} = \frac{F}{\sqrt{\pi l}} - \sigma_{rr}\sqrt{\pi l} + \frac{3Fl^{3/2}}{2x^2\sqrt{\pi}} - \frac{3l^2}{4z^2}\sigma_{rr}\sqrt{\pi l} \quad \text{..... (2.57)}$$

Where,

$$F = l_0\{\sigma_z - \sigma_{rr}\}\frac{2}{3\pi} \quad \text{..... (2.58)}$$

In the *r*-*z* plane, the crack generated stresses are neglected in the study. $F + \Delta F$ is the sum of the wedging forces due to the undisturbed stress field and that caused by the crack generated stress. The superposition of these stresses are based on the assumption that the deformation is small.

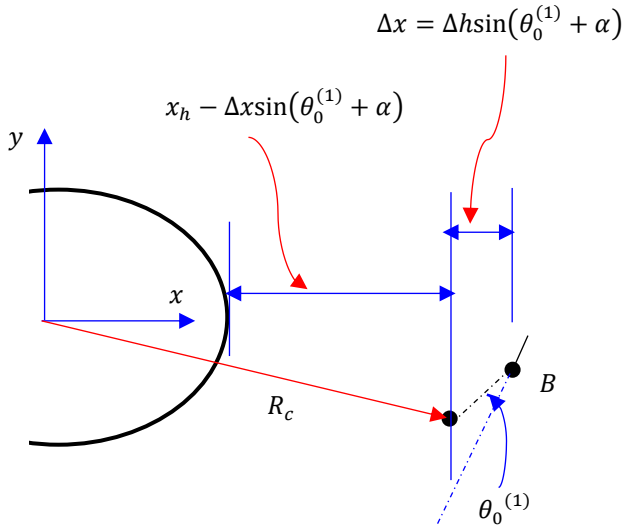

Fig. 2.14. Schematic illustration of the path of the propagating radial crack.

It should be noted that the radial stress can be replaced with the hyperbolic stress and the tangential stress with the elliptic stress when the wellbore is elliptic in shape.

The radius of curvature, R_C, is the sum of the curvature of the wellbore and the distance of the propagating crack tip to the borehole boundary (Fig. 2.14).

$$R_C = \frac{2ab^2}{a^2+b^2} + x \quad \text{..... (2.59)}$$

Knowing the mode I stress intensity factor, the mode II stress intensity factor can be approximately determined from the simple elliptic relation

$$\left(\frac{K_I}{K_{Ic}}\right)^2 + \left(\frac{K_{II}}{K_{IIc}}\right)^2 = 1 \quad \text{..... (2.60)}$$

K_{IIc} and K_{Ic} are determined from experiments; they are the fracture toughness for mode I and II respectively. In many cases, they are assumed to be equal (Sun and Jin 2012).

With the stress intensity factor known, the strain energy density factor S, introduced by Sih (1973) can be determined. The strain energy density factor is a vector field; it provides a knowledge of the mixed mode crack extension in that it specifies the crack extension direction and the mixed-mode material fracture toughness at each point in the field.

$$\begin{aligned} S = {} & \frac{K_I{}^2}{16G\pi}\{(\kappa-\cos\theta)(1+\cos\theta)\} \\ & + \frac{K_I K_{II}}{8G\pi}\sin\theta\{2\cos\theta-(\kappa-1)\} \\ & + \frac{K_{II}{}^2}{8G\pi}\begin{Bmatrix}(\kappa+1)(1-\cos\theta) \\ +(1+\cos\theta)(3\cos\theta-1)\end{Bmatrix} \end{aligned} \quad \text{..... (2.61)}$$

For plane strain condition, $\kappa = 3 - 4\nu$.

By finding the value of $\theta = \theta_0$ that minimizes the strain energy density factor; i.e.

$$\left.\begin{aligned} \frac{\partial S}{\partial \theta} &= 0 \text{ at } \theta = \theta_0 \\ \frac{\partial^2 S}{\partial \theta^2} &= 0 \text{ at } \theta = \theta_0 \end{aligned}\right\} \quad \text{..... (2.62)}$$

The fracture initiation condition is then characterized by

$$S(\theta_0) = S_{cr} \quad \text{..... (2.63)}$$

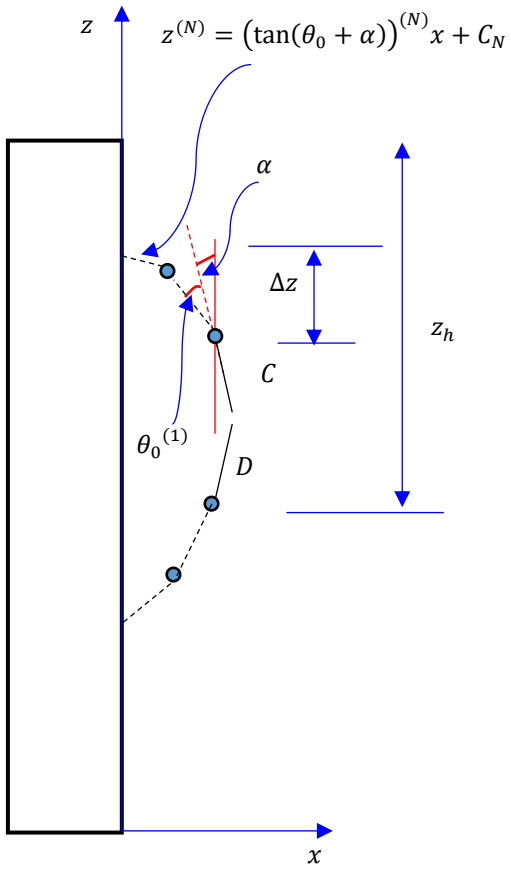

Fig. 2.15. Schematic illustration of the paths of the propagating longitudinal cracks.

2.11 Algorithm for Determining the Path of the Propagating Cracks

i. Determine the location of the cracks that satisfy the lower bound of this criterion:

$$\sigma_{rr}{}^{c} \geq \frac{0.1l_0}{x_h}\sigma_{\theta\theta} \text{ for } r-\theta \text{ plane and } \sigma_{rr}{}^{c} \geq \frac{0.1l_0}{z_h}\sigma_z \text{ for } r-z \text{ plane}$$

ii. Choose the step size Δx or Δz depending on the plane of interest.

iii. Compute the crack initiation angle, $\theta_0{}^{(1)}$

iv. Compute the minimum strain energy density factor at the current location, $S\left(\theta_0{}^{(1)}\right) = S_{cr}$

v. Compute the strain energy density factor, S, at the current location; if $S < S_{cr}$, no extension, then stop. But if $S > S_{cr}$, extend the path in the direction of $\theta_0{}^{(1)}$ by Δx or Δz, depending on the plane of interest.

vi. At the new position, compute the crack initiation angle $\theta_0{}^{(2)}$

vii. Compute the new minimum strain energy density factor, $S\left(\theta_0{}^{(2)}\right) = S_{cr}$

viii. Compute the strain energy density factor, S, at this point, based on the new length of the crack and radius of curvature; if $S < S_{cr}$, no extension, then stop. But if $S > S_{cr}$, extend the path in the direction of $\theta_0{}^{(1)}$ by Δx or Δz, depending on the plane of interest.

ix. Repeat the steps until the path intersects the borehole boundary

x. Find the intersecting points between the equations of the last piece-wise linear paths and the equations defining the geometry of the borehole (circle or ellipse or straight line or hyperbola); see Figs. 2.13c. and 2.15.

The values of z_h and x_h are obtained by simultaneously solving Eqs. (2.64) and (2.65)

$$\sigma_{rr}\left(x_h, z_h\right) = \frac{0.1 l_0}{x_h}\sigma_{\theta\theta}\left(x_h, z_h\right) \quad \text{.....(2.64)}$$

$$\sigma_{rr}\left(x_h, z_h\right) \geq \frac{0.1 l_0}{z_h}\sigma_z\left(x_h, z_h\right) \quad \text{.....(2.65)}$$

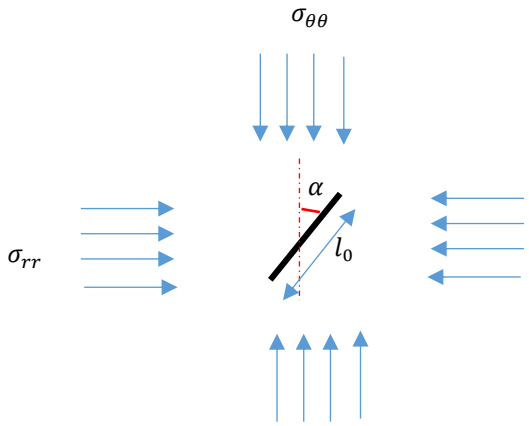

Fig. 2.16. Standing crack under compression loading, in the vicinity of a circular borehole, (in an infinite medium) under polyaxial loading, propagating through a wedging force.

2.12 Numerical Example of Type-B Breakout Pattern Formed Through Extensile Splitting in a Homogeneous Formation

Using the same values of the rock properties provided in Section 2.8; and assuming the in-situ stresses vary linearly with depth (upwards) according to these relations

$$\left.\begin{aligned}\sigma_v &= 88.6(1-0.001z)\text{MPa}\\ \sigma_H &= 29.53(1-0.001z)\text{MPa}\\ \sigma_h &= 26.29(1-0.001z)\text{MPa}\end{aligned}\right\} \quad \text{..... (2.66)}$$

The fracture toughness (modes I and II) of the shale formation are assumed to be 41.37 MPa, the elastic shear modulus is 5.6GPa.

Determining the values of z_h and x_h, the location of the cracks that define the maximum failure extent:

From Eqs. (2.2) to (2.5), substituting $r = a + x$; the values of x_h and z_h are 0.1634m and 269.36m respectively; the size of the initial crack was assumed to be 0.0253m. The calculated distances simply show that the cracks below 269.36m from the top of the formation and 0.163m away from the borehole boundary will not propagate. But the formation section is just 27.43m thick; therefore all the cracks within a distance of 0.1634m from the borehole boundary will propagate and have unstable growth when the critical length of the cracks are reached.

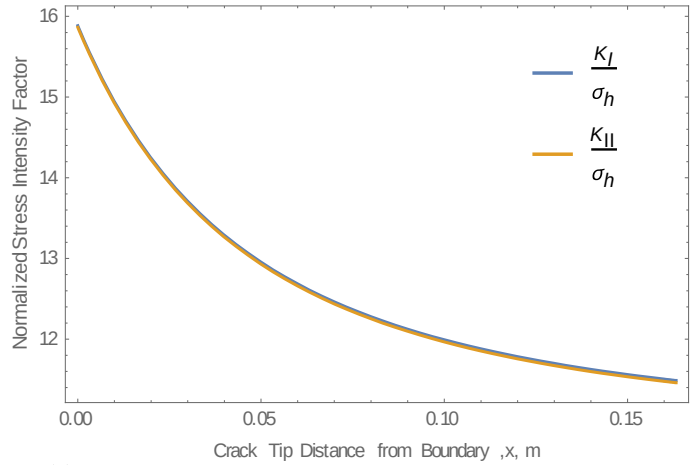

(a)

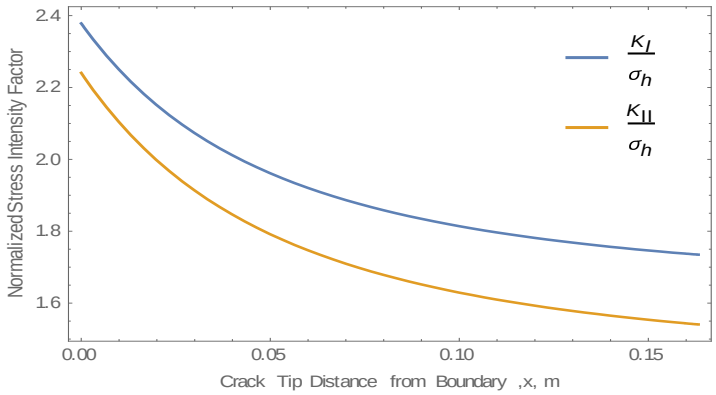

(b)

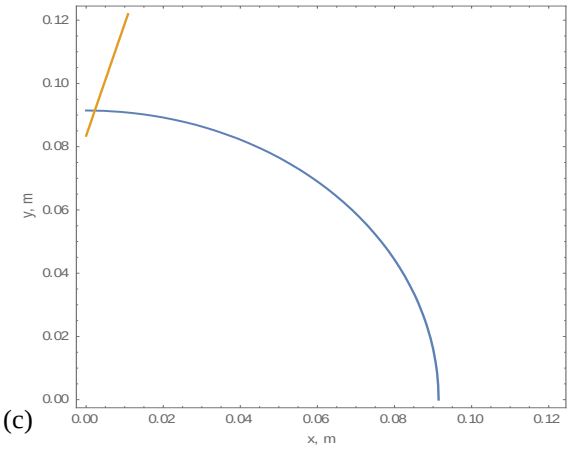

(c)

Fig.2.17. (a) The stress intensity factors distribution from the tip of the initial crack to the borehole boundary ($r-\theta$) (b) The stress intensity factors distribution from the tip of the crack to the borehole boundary after the crack has increased in length (the first step size) ($r-\theta$ plane). (c) Estimation of the breakout width; only the quadrant is shown since symmetry is applicable. The breakout width in this case is almost 180^0.

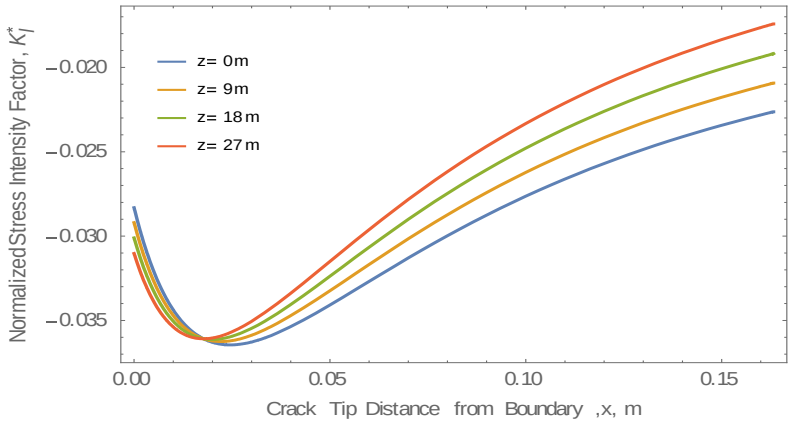

(a).

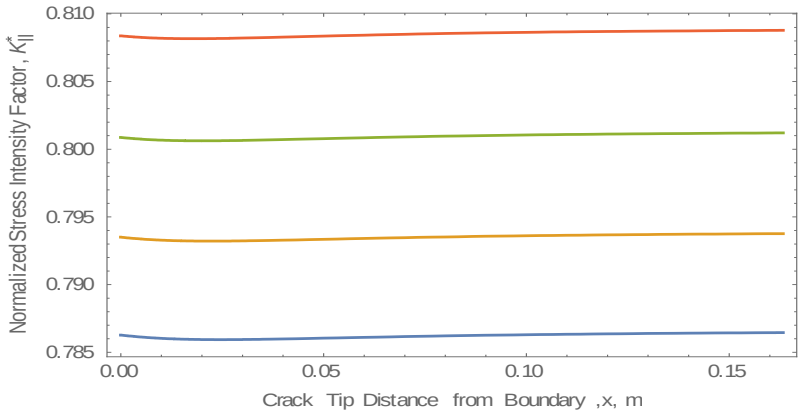

(b)

Fig.2.18 (a) Mode I stress intensity factor distribution from the tip of the initial crack to the borehole boundary (r – z plane). (b) Mode II stress intensity factor distribution from the tip of the initial crack to the borehole boundary (r –z plane). (c) Mode I stress intensity factor distribution from the tip of the crack to the borehole boundary after the length has increased (r –z plane) (d) Mode II stress intensity factor distribution from the tip of the crack to the borehole boundary after the length has increased (r – z plane).

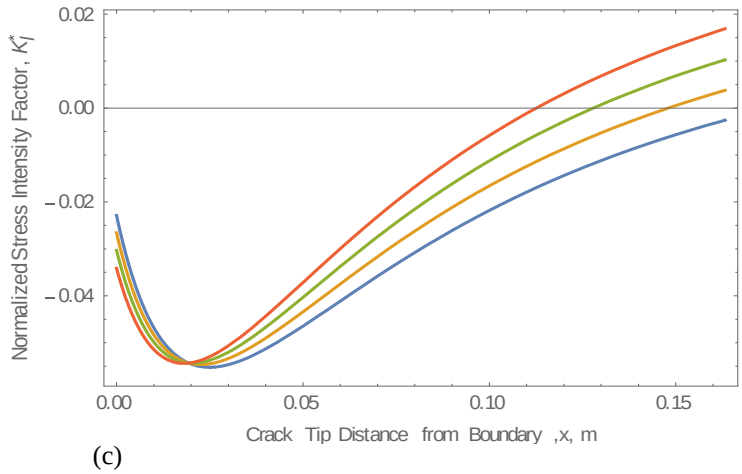

(c)

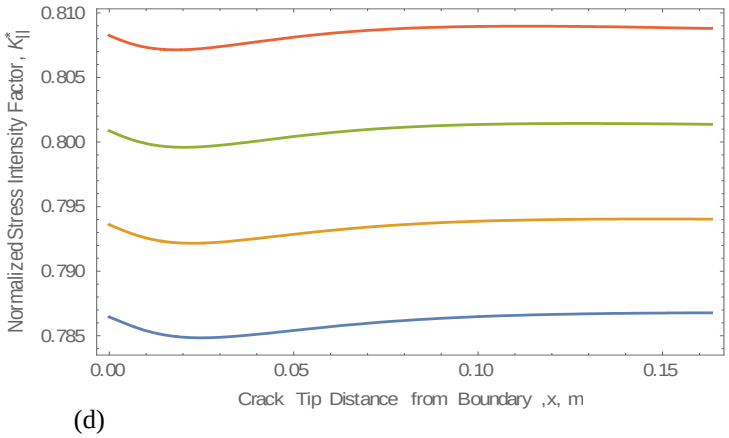

(d)

Fig.2.18 Continued

As observed in Figs. 2.18a to 2.18d, the crack tends to propagate through mode II—shear. This observation is not often seen, as cracks would want to propagate through mode I.

The failed region in the $r - z$ plane is very small, centered at the middle of the formation.

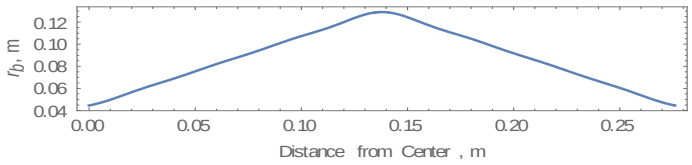

Fig.2.19. Breakout pattern in the $r-z$ plane.

2.13 Breakout Volume

The volume of sand produced can be determined by rotating the breakout pattern in the $r-z$ plane through the z-axis by the angle substended in the $r-\theta$ plane. The volume generated is

$$V = \frac{\theta_b}{2\pi}\int_{z_0}^{z} \pi\left(f(z)^{-1}\right)^2 dz \quad \text{..... (2.67)}$$

Fourier series can be used to track the trajectory of the propagating cracks, as illustrated in Section 2.4. The inverse of the Fourier function is used in determining the volume of sand produced. Alternatively, a simpler function, which can be easily inverted, may be used to define the trajectories of the propagating extensile cracks or shear fractures.

2.14 Summary

Knowing the breakout azimuth and location of the intersection of the projected shear fractures, the breakout volume can be approximately determined; this approach saves a lot of computation efforts. Even when the breakout depths and widths are calculated for each depth location, using regression analysis in fitting the curve can be an

arduous task. From the numerical experiments conducted, it was observed that this theory works, although it can over predict the failed region.

In the same vein, trajectories of the propagating extensile cracks define the breakout pattern; although this statement is self-evident, the toroidal nature of type-B breakout is born from it. Using minimum strain energy criterion, the trajectories of the extensile cracks will form a torus-like shape. For a thick formation, the torus may not form at the center even if the formation is homogeneous; the location of the outer-bounds of the propagating cracks strongly depends on the rock properties and the distribution of the radial or hyperbolic and axial stresses; this is contrary to the shear-fracture induced failure theory, which predicts that the deepest breakout depth will always occur at the center of a homogeneous formation.

In a homogeneous formation, the fracture angles are the same for both propagating shear fractures, and the two failure lines will definitely meet at the center. When the formation is heterogeneous, the intersecting location depends greatly on the degree of vertical heterogeneity layout of the formation. If the upper layer is softer than the lower layer, the shear fracture lines will intersect at the upper layer. And if the layout is reversed, the two lines will intersect at the lower layer; in a nutshell, irrespective of the layout, the two lines will intersect in the softer layer.

3. ESTIMATING CAVING SIZE DURING WELLBORE BREAKOUT

3.1 Scope

Estimation of caving size during breakout process is very essential when predicting the potential for borehole bridging during blowout, or investigating any associated risks during underbalanced drilling or production operations. In this work, we present a rigorous approach for estimating the geometrical dimensions of caving produced during wellbore breakout; we assumed a rectangular plate in this framework. Using dipole and beam asymptotic analyses, stress intensity factors at the tips of a single representative crack, close to the wellbore boundary are derived; the new stress intensity factors are based on the frameworks developed by Dsykin and Germanovich. Furthermore, we applied plate buckling theory to determine the limiting buckling length and width of the plate, while the thickness of the plate is determined using shear-dilatancy theory.

3.2 Damage Initiation Around Wellbore

Fracture mechanics-based approaches give more insights into the accumulation of micro-cracks and extensive crack growth around the borehole, which lead to the formation of breakout. This study focuses on wing-crack growth and its interaction with the free surface. The buckling of wing-cracks that propagate sub-parallel to the direction of the major principal stress direction causes the formation of wellbore breakout. Landau and Lifshitz (1959) developed a critical buckling length for a slender plate compressed from both ends, but not subjected to any lateral loading. This solution has often been used to predict the buckling length of unstable wing cracks. However, we present in this paper a

more comprehensive derivation of the buckling length, considering the impact of the wellbore pressure support.

Regions surrounding wellbores are not devoid of damage. The excavation of a hole in the rock initiates damaged zones around the near-wellbore region, especially in the direction of maximum compression (Fig.3.1). Knowing the extent of damage around the wellbore prior to the onset of the breakout process is important in order to adequately predict the size of cavings.

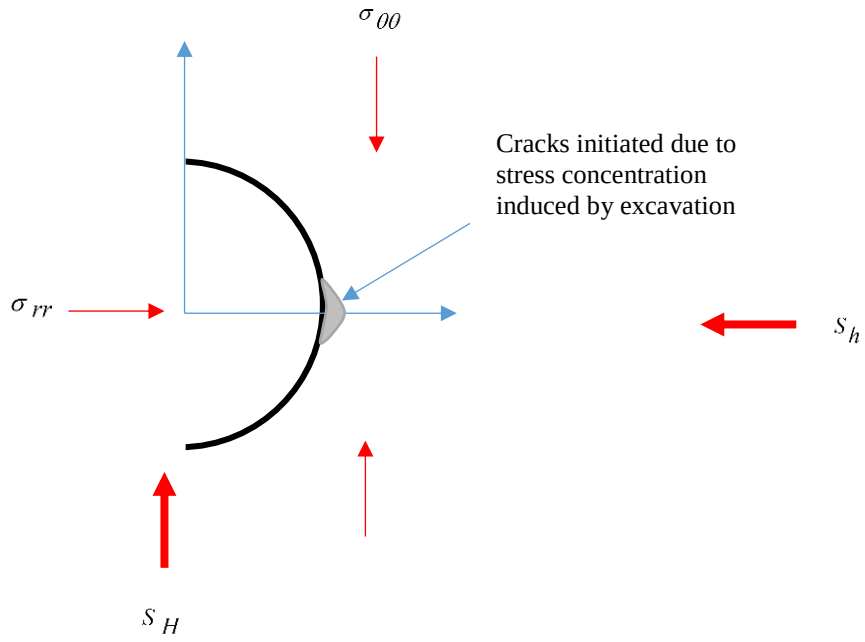

Fig. 3.1. Damaged state around the wellbore prior to the stable propagation of the standing initial cracks.

In past studies, some authors characterize the size of the damaged region by the use of a critical stress or strain state (Morita 2016, Papanastasiou and Vardoulakis 1992, 1994, and Vardoulakis and Sulem 1995); post peak softening law is often required to introduce the damage effect. Zou et al. (1996) degraded the Young's modulus of the failed zone. Muhlhaus and Vardoulakis (1987) and Cheatham (1993) used continuum damage mechanics to characterize the damaged zones. Shao et al. (1994) analyzed the borehole failure using stress-induced micro-cracking, treating the rock as a nonlinear elastic anisotropic material. Detournay (1986) used Galin's approximation to define the plastic zone. Nawrocki and Dusseault (1995) used radius dependent Young's modulus to define the non-linear behavior of the near-well region.

In this study, we first present a background on failure mechanism around the wellbore, considering the interactions between the micro-cracks and the boundary surface. Second, we present a method, based on shear-dilatancy effect, to determine the initial size of the representative micro-crack prior to the onset of breakout. Although Germanovich and Dyskin (1999) have derived the stress intensity factors at the tip of the growing representative micro-crack, which interacts with the boundary surface using the dipole and beam asymptotic approximations, we extended the model by incorporating the influence of lateral stress on the stress intensity factors for the beam asymptotic approximation. Finally, we derived the buckling lengths of the separated slender rock-layer, formed as the representative micro-crack propagates around the wellbore by using plate bending theory. In this study, the influence of the wellbore pressure is considered, unlike the previous model by Landau and Lifwitz that disregarded lateral loading of the slender plate.

One of the benefits of this study is appreciated when predicting the potential for self-killing of a blowing well.

3.3 Failure Mechanism and Wing-Crack Model

Failure is initiated by the increase in the compressive stress concentration acting parallel to the boundary. As the stress reaches a critical value, the tensile fractures will be generated, growing towards the direction of the applied load (Figs. 3.2). Experiments conducted by Brace and Bombolakis (1963), Hoek and Bieniawski (1964), Nemat-Nasser and Horii (1982), and Ewy and Cook (1990) confirmed the growth of the cracks toward the compression in a stable manner.

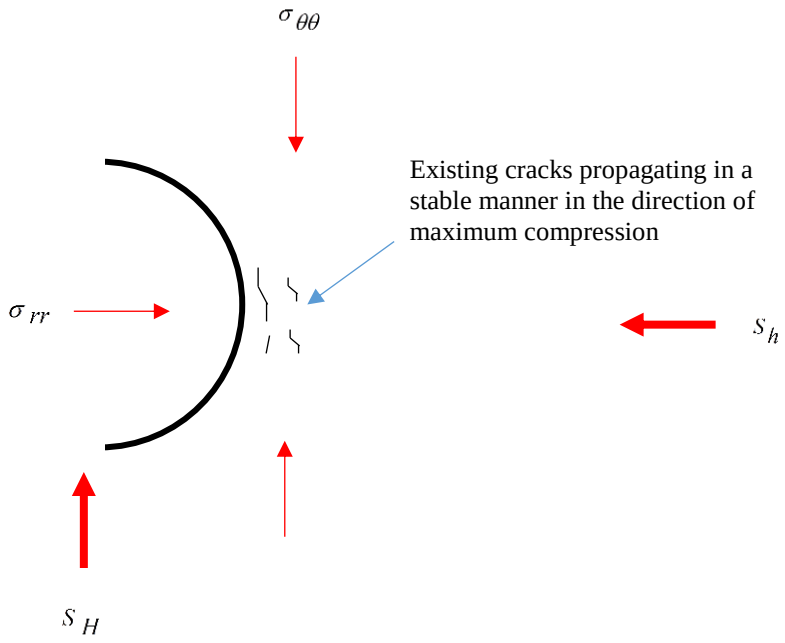

Fig. 3.2. Existing cracks propagating towards the direction of the maximum compressive force in the horizontal plane.

As the stable crack growth continues, the influence of the boundary amplifies its growth, such that as it reaches a critical length the growth becomes unstable. Thus, the crack rapidly increases its length and separates a thin layer from the rock mass. When the length of the slender layer reaches a limiting value it buckles**;** and the process repeats itself, and eventually the failure ends. Results from many experiments confirm this progression. In addition, the stress concentration zone around the borehole reduces as the failure progresses; this factor also helps to stabilize the borehole.

During the rupture process, cracks propagate both in the vertical and horizontal planes; a schematic is shown in Fig. 3.3.

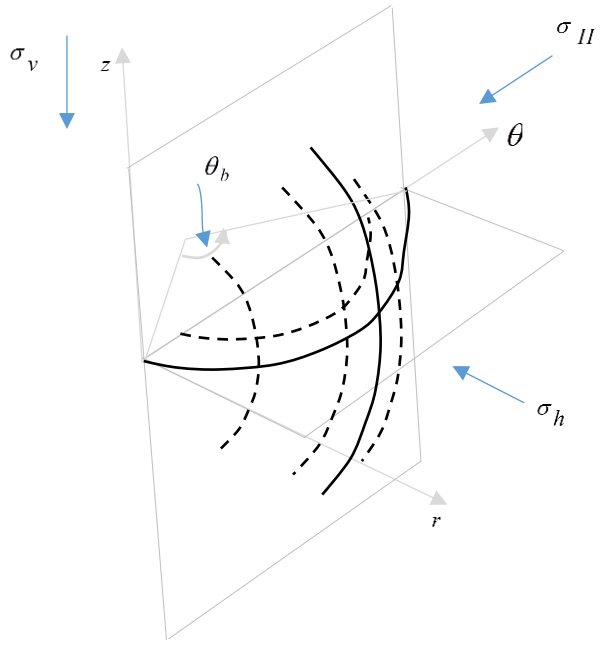

Fig.3.3. Propagation of cracks in the vertical and horizontal planes.

For simplification, we disregarded the interactions between the propagating cracks in the horizontal and vertical planes in this analysis. But the interactions among inter-planar propagating cracks can be represented by considering the average crack within the group, i.e. the crack with the average initial size and average distance from the boundary. Germanovich and Dyskin (1999) performed a finite element modeling that indicates that the average value for the factor accounting for the friction and influence of the curvature of the secondary cracks is $\bar{\beta} = 2/3\pi$.

Following the work of Fairhurst and Cook (1966), the propagation of the pre-existing crack is driven by pair of concentrated forces. Assuming the crack to be rectilinear and makes an angle α with the direction of the compressive force, the value of these forces (per unit length of the inclined contact area) is equal to the horizontal projection of the shear force that tends to displace the opposite faces of the crack.

Germanovich and Dyskin (2000), Germanovich et al. (1994), and Dyskin and Germanovich (1991) derived the wedging force that drives the opening of the crack faces; considering the influence of the lateral stress (radial stress for a circular borehole), the wedge force is

$$F = 2\,a_0\left(\sigma_{\theta\theta} - \sigma_{rr}\right)\beta(\alpha) \quad \text{..... (3.1)}$$

$2a_0$ is the initial size of the crack, $\sigma_{\theta\theta}$ is the hoops stress, σ_{rr} is the back pressure (radial stress for a circular wellbore), and $\beta(\alpha) = \sin 2\alpha \cos\alpha(1 - \tan\alpha\ \tan\mu)$. By using a single crack that represents the whole pre-existing cracks, which also considers the interactions among the micro-cracks, the factor $\beta = \bar{\beta} = 2/3\pi$.

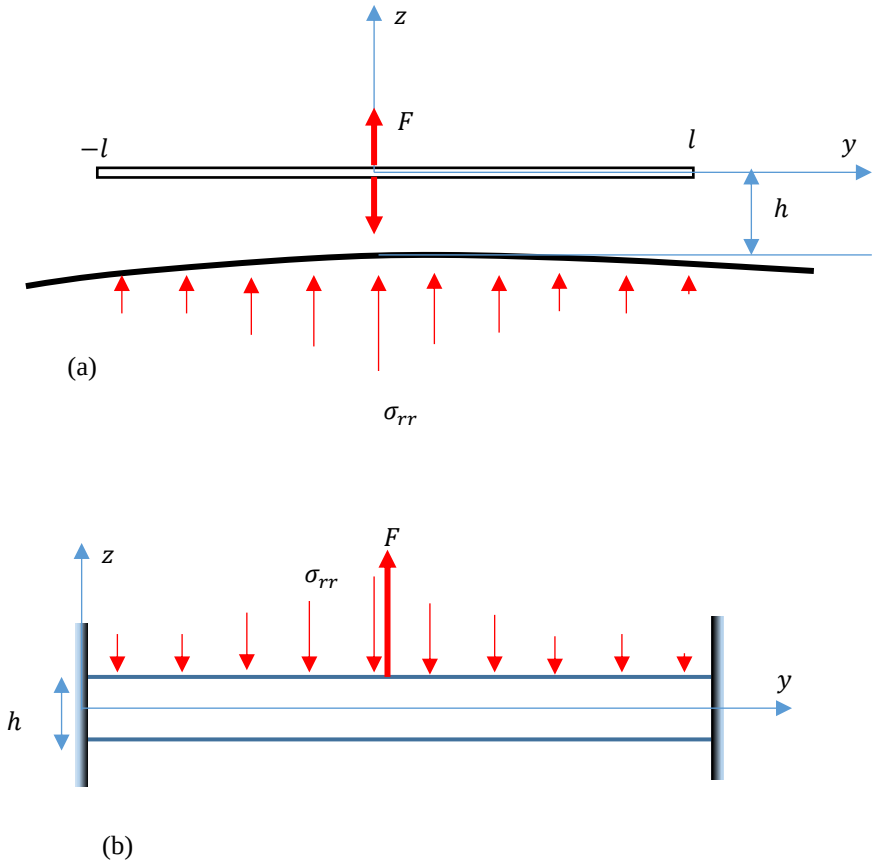

Fig. 3.4. (a) Schematic of the forces acting on the slender rock layer (b) a representation of the foregoing problem by beam asymptotic.

From extensive analysis by Germanovich and Dyskin (2000), the influences of crack and boundary curvatures are not significant as the crack propagates near the boundary surface. The stress intensity factor of a propagating crack near a flat boundary surface based on dipole asymptotic method is:

$$K_I = \frac{F}{\sqrt{\pi\, l}} - \sigma_{rr}\sqrt{\pi\, l} + \frac{3Fl^{3/2}}{2h^2\sqrt{\pi}} - \frac{3l^2}{4h^2}\sigma_{rr}\sqrt{\pi\, l} \quad \text{..... (3.2)}$$

But in the case where the length of the crack is much greater than the distance between the crack and the boundary surface, the dipole asymptotic method fails. In this case, beam asymptotic is used (Fig. 4). Interpolating between the two asymptotic methods, the mode-1 stress intensity factor is

$$K_I = \frac{F}{\sqrt{\pi l}} - \sigma_{rr}\sqrt{\pi l} + \left\{\frac{3Fl^{3/2}}{2h^2\sqrt{\pi}} - \frac{3l^2}{4h^2}\sigma_{rr}\sqrt{\pi l}\right\}\frac{1}{1+a_1 l^n} + \frac{0.483a_1 Fl^{n+1}}{\left(1+a_1 l^n\right)h^{3/2}} - K_{BM} \quad \text{..... (3.3a)}$$

where,

$$K_{BM} = \frac{1.932a_1 l^n}{\left(1+a_1 l^n\right)h^{3/2}}\frac{1}{l}\int_0^l y*\left\{1/2\int_0^l \sigma_{rr}\,dy - \left(1-1/\lambda_y\right)\int_0^y \sigma_{rr}\,dy\right\}dy \quad \text{..... (3.3b)}$$

Equation (3.3b) accounts for the influence of lateral stress on the stress intensity factor for the beam asymptotic approximation of the foregoing problem. The average bending moment acting on the whole length of the slender plate is used in equation (3.3b).

The model-2 stress intensity factor is only significant when the beam asymptotic approximation is valid (i.e. when the length of the crack is sufficiently greater than the distance to the boundary surface, *h*).

$$K_{II} = \frac{0.3765a_2 Fl^{n+1}}{\left(1+a_2 l^n\right)h^{3/2}} - K_{BN} \quad \text{..... (3.4a)}$$

$$K_{BN} = \frac{1.506a_2 l^n}{\left(1+a_2 l^n\right)h^{3/2}}\frac{1}{l}\int_0^l y*\left\{1/2\int_0^l \sigma_{rr}\,dy - \left(1-1/\lambda_y\right)\int_0^y \sigma_{rr}\,dy\right\}dy \quad \text{..... (3.4b)}$$

Matching the analytical model with the numerical experiment conducted by Dyskin et al. (1998), and Germanovich and Grekov (1998), the model parameters are $a_1 = 1.78$, $a_2 = 1.81$, and $n = 1.5$. The unstable crack growth starts at the point where K_I is minimum (Fig. 3.5).

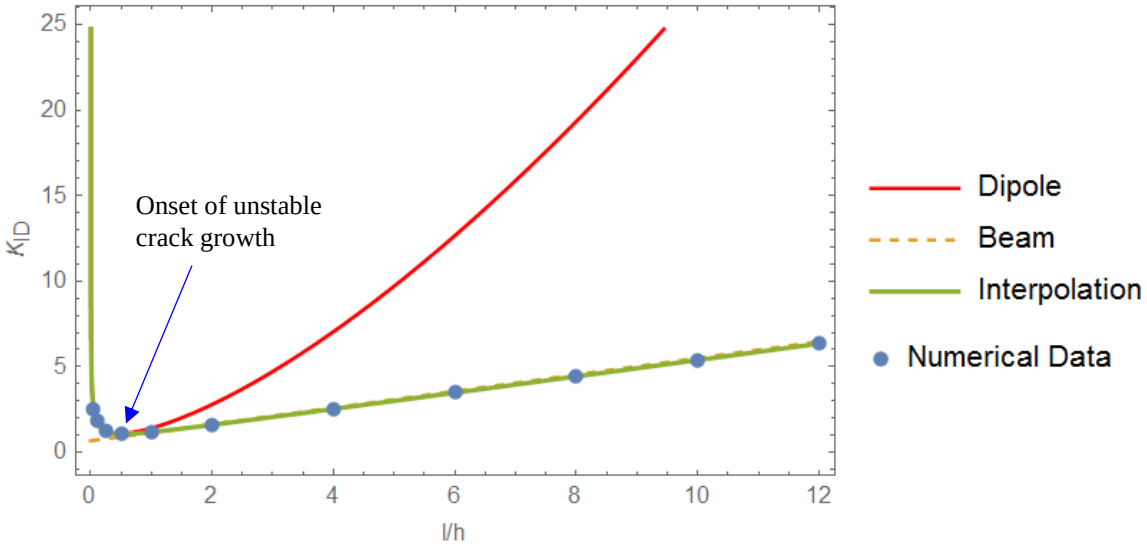

Fig. 3.5. Comparing mode-1 stress intensity factor with numerical data; back stress is zero in this case.

Mathematically, the critical length at which the unstable crack propagation starts is determined from the stationary condition; the half length of the crack that satisfies the stationary condition:

$$\frac{\partial K_I}{\partial l} = 0 \quad \text{..... (3.5)}$$

Without including the contribution of the lateral stress concentration due to excavation, Dyskin and Germanovich (1991) showed that the critical length at which unstable growth starts is

$$l_{cr} = \frac{\sqrt{2}}{3} h \quad \text{.....(3.6)}$$

The critical stress corresponding to the onset of unstable crack growth is determined by substituting the critical length expression derived from equation (4) into the Irwin (1957) crack propagation equation

$$K_I = K_{IC} \quad \text{.....(3.7)}$$

When the influence of the lateral stress is disregarded, (Dyskin and Germanovich 1991) derived the critical stress as

$$\sigma_{\theta c} = \frac{\sqrt[4]{2} K_{IC} \sqrt{3\pi h}}{8 a_0 \overline{\beta}} \quad \text{.....(3.8)}$$

It should be noted that if the length of the stress concentration zone around the borehole is less than the critical length for unstable growth, unstable crack propagation will never occur, only stable crack growth. Furthermore, sufficient back stress can suppress the unstable crack growth even if other favorable conditions for rapid crack growth exists: the crack length is greater than the critical length (equation 5), and the length of the stress concentration zone is large.

3.4 Initial Size of the Representative Pre-Existing Crack

A single crack is used to represent the pre-existing micro-cracks. The interaction existing among the micro-cracks is factored in using averaged $\bar{\beta} = 2/3\pi$. From Fig. 3.6, the initial length of the existing representative crack is determined as

$$2a_0 = 2\left(r_w + \frac{H}{2}\right)\theta_0 \quad \text{.....(3.9)}$$

And the position of representative crack is simply, $h = \frac{H}{2}$. θ_0 may be determined by using the critical stress condition; i.e. the angle θ that satisfies this condition:

$$\theta_0 : \sigma_{\theta\theta}(h) = \sigma_{\theta\theta}{}^{C}(h) \quad \text{.....(3.10)}$$

Alternatively, zero volumetric strain due to second order effects can be used to determine

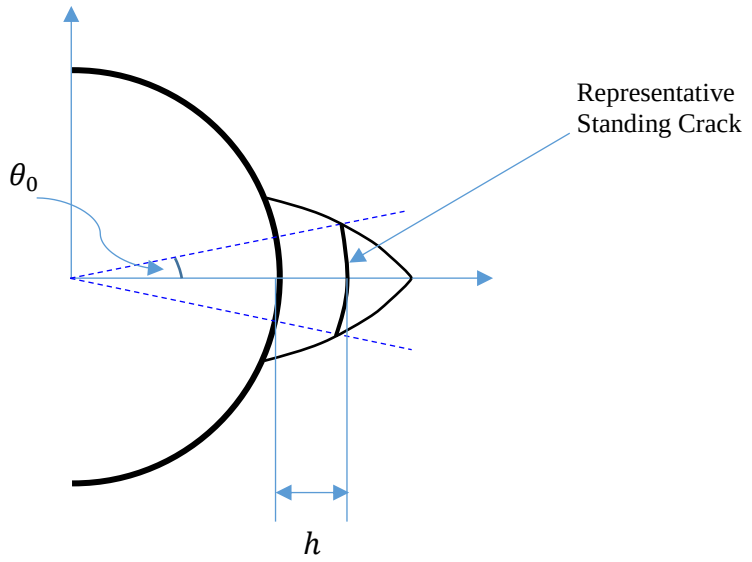

Fig. 3.6. Size of the representative pre-existing crack (enlarged size) in the horizontal plane.

θ_0 :

$\theta_0 : d\psi(h) = 0$ .....(3.11a)

As derived by Oyedokun and Schubert (2017), the volumetric strain due to second order effect (dilatancy effect) in an isotropic material body under polyaxial loading is

$$d\psi = \frac{\sigma_m}{K} + \frac{\alpha_4}{4KG^2}\left\{\begin{array}{l}(\sigma_1-\sigma_2)^2\left[\frac{(\sigma_1-\sigma_2)}{(\sigma_1-\sigma_2)^*}\right]^{2n} + (\sigma_1-\sigma_3)^2\left[\frac{(\sigma_1-\sigma_3)}{(\sigma_1-\sigma_3)^*}\right]^{2n} \\ -(\sigma_1-\sigma_2)(\sigma_1-\sigma_3)\left[\frac{(\sigma_1-\sigma_2)}{(\sigma_1-\sigma_2)^*}\right]^{n}\left[\frac{(\sigma_1-\sigma_3)}{(\sigma_1-\sigma_3)^*}\right]^{n}\end{array}\right\} \quad \text{..... (3.11b)}$$

σ_m is the mean normal stress, α_4 and *n* are empirical constants that are determined from experiment, *K,* is the bulk modulus of the material body, and *G* is the shear modulus of the material body.

3.5 Buckling Lengths of the Growing Slender Rock Layer

The slender rock layer separated from the rest of the rock mass can be characterized as a plate. A plate has its planform dimensions larger than its thickness, and it is also subjected to loads that can cause deformation and strectching. To further simplify the foregoing problem, the wellbore fluid is assumed to diffuse into the growing micro-crack, without having any significant impact on the growth of the micro-crack. The influence of the vertical stress in disregarded when considering the buckling tendency through the hoops stress. Thus, the slender rock layer is treated as a simply-supported plate

under uniaxial compression (Fig. 3.7). As derived by Reddy (2007), the critical buckling load for an isotropic rectangular plate under in-plane uniaxial compression is

$$\sigma_{\theta c} = \frac{\pi^2 D}{L_B^2}\left(1+\frac{L_B^2}{t_B^2}\right)^2 \quad \text{.....(3.12)}$$

where, $D = \frac{E\,h^3}{12\,(1-\nu^2)}$ is the bending stiffness of the slender plate,

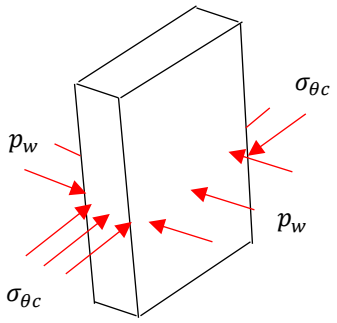

Fig. 3.7. Free body diagram showing the force system acting on the plate as viewed in the horizontal plane.

In the vertical plane, the slender rock layer is also treated as a simply supported plate under uniaxial compression through the critical vertical stress. In this plane, the critical stress is in the vertical direction. Based on the assumption that the wellbore fluid diffuses into the growing crack, the influence of the pressure forces on the buckling of the vertical plate is assumed to be negligible. These forces act in the transverse orientation to the loading direction and will counteract each other (Fig. 3.8). Hence, the thickness of the plate at the buckling condition is determined by solving for t_B in Eq. 3.13. It is obvious

that both equations (3.12) and (3.13) would need to be solved simultaneously to determine the geometry of the plate. From the foregoing analysis, the plate is presumed to have a rectangular shape, as an approximation; from field and laboratory studies, the plates are often irregular in shape.

$$\sigma_{vc} = \frac{\pi^2 D}{t_B^2}\left(1+\frac{t_B^2}{L_B^2}\right)^2 \quad \text{..... (3.13)}$$

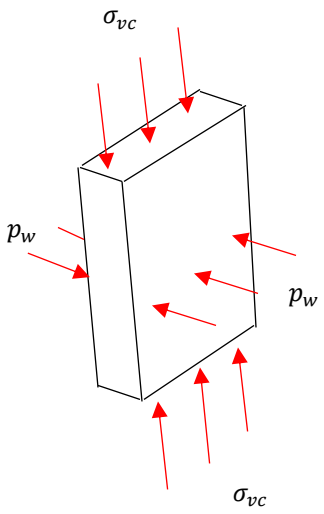

Fig. 3.8. Free body diagram showing the force system acting on the plate as viewed in the vertical plane.

This analysis presents a more rigorous approach for estimating the limiting buckling length of the growing slender layer, than that proposed by Landau and Lifshitz (1959), who approximated the slender layer as a square-plate strip.

$$l_B = \pi\, h \sqrt{\frac{E}{k_T \Delta\sigma_{cr}\left(1-\nu^2\right)}} \quad \text{..... (3.14)}$$

Dyskin et al. proposed that the critical buckling stress can be approximated as

$$\Delta\sigma_{cr} = \sigma_{\theta c} \cong 2\frac{a}{b}\max\left(\sigma_{xx}, \sigma_{yy}\right) \quad \text{..... (3.15)}$$

3.6 Breakout Width Estimation

As derived in above the buckling length of the slender rock layer generated as a result of the propagation of the representative crack in the first borehole failure episode will determine the breakout width. And from Fig. 3.9, the breakout width can be estimated through the relation

$$\frac{1}{2}\theta_{\mathrm{B}} = \frac{L_B}{\left(r_w + \frac{H}{2}\right)} \quad \text{..... (3.16)}$$

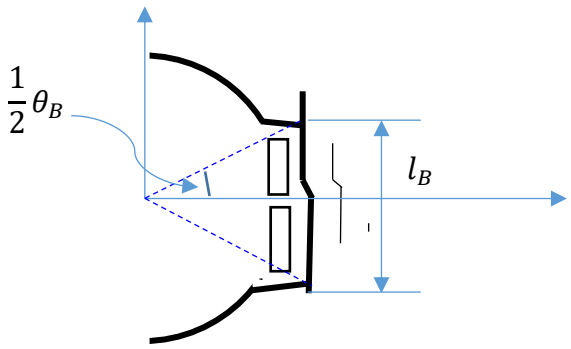

Fig. 3.9. Buckled rock plate as viewed in the horizontal plane.

3.7 Numerical Analyses

Parametric studies on the plate-strip model, proposed by Landau and Lidwitz (1959), are conducted, considering the effects of the mechanical properties of the rock, in-situ stress loadings, and wellbore geometry on the limiting buckling length of the slender plate. Furthermore, the influence of the back stress on the borehole failure is emphasized; two synthetic cases are used. Finally, the relationship between the limiting buckling length and thickness of the plate is investigated for varying values of wellbore pressure, in-situ stress, and position of the representative standing crack to the boundary surface.

3.7.1 Parametric Studies on 1-D Plate Strip Approximation

3.7.1.1 Effect of Plain Strain Young's Modulus on Caving Size

For a given state of stress around a borehole, as the plain strain Young's modulus of the rock increases, the caving size increases (Fig. 3.10a). This suggest that the breakout width in sandstone is expected to be wider than shale, assuming all other parameters are the same. For example, considering a case where $\Delta\sigma_{cr}$ is 7500 psi and h is 0.1inch, the variation of the caving size is shown in Fig 3.10b.

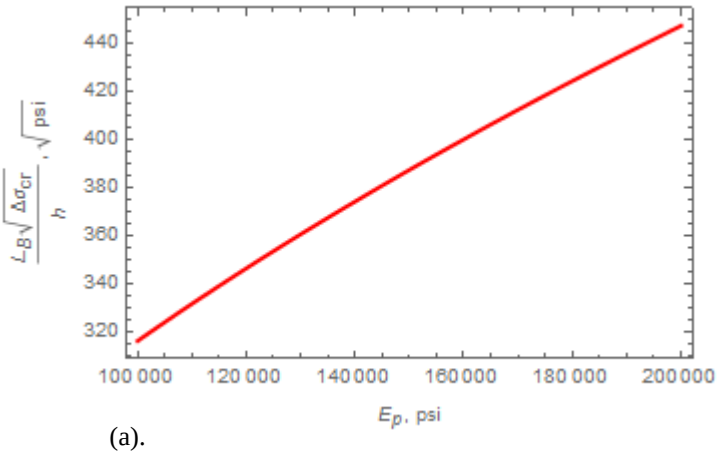

(a).

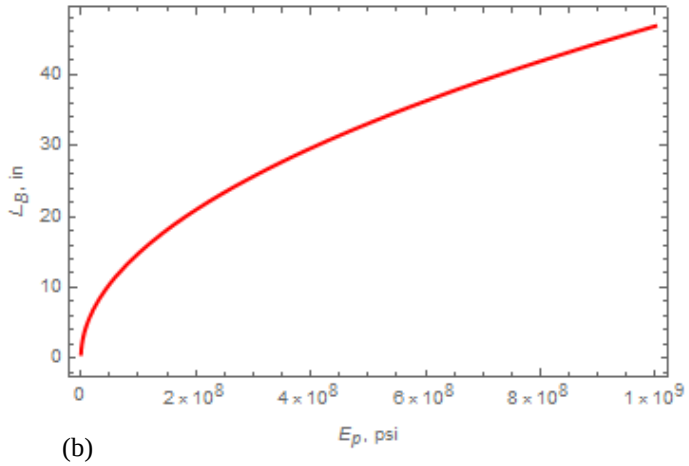

(b)

Fig.3.10 (a) Variation of caving size on plane strain Young's modulus (b). Variation of caving size on plane strain Young's modulus, an example case.

3.7.1.2 Effect of In-situ Stress Loading and Well Angles on Caving Size

Increase in the in-situ stress reduces the size of the caving, as shown in Fig. 3.11a. In the example shown below, it is evident that large caving size will be produced in a vertical well than in a horizontal well under the same in-situ stress loading (Fig. 3.11b). On the other hand, the azimuth of the well contributes to the increase in caving size, as it

increases from 0 to $\frac{\pi}{2}$. An increase in pore pressure reduces the effective stress, hence increases the caving size.

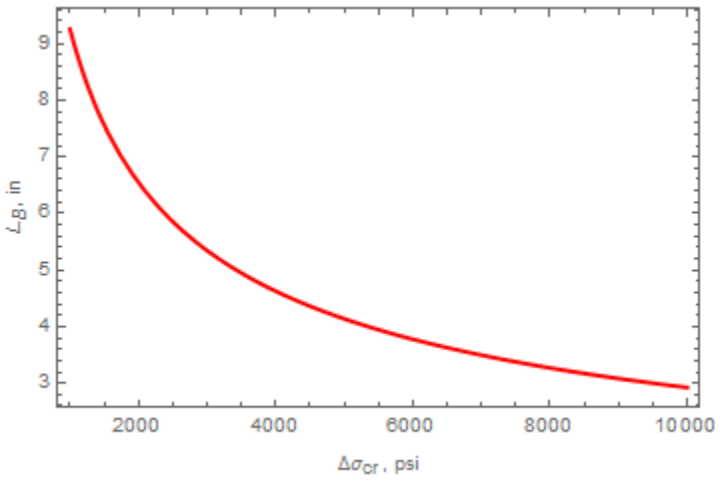

(a)

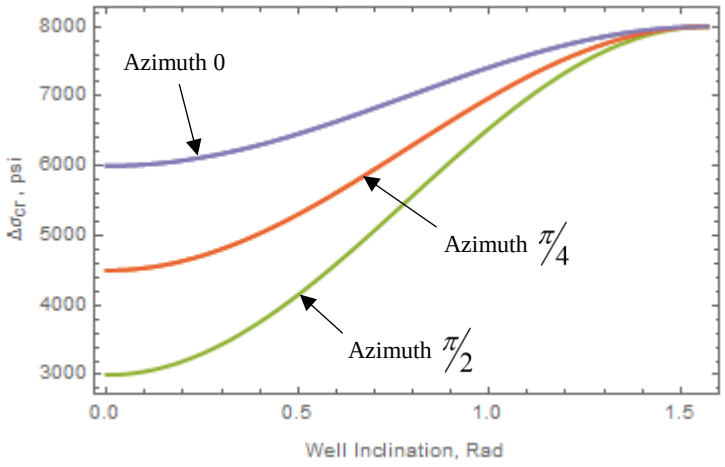

(b)

Fig. 3.11 (a) Variation of caving size with buckling stress. (b).Variation of buckling stress with well angles.

3.7.1.3 Effect of Wellbore Shape on Caving Size

The ellipticity index of the wellbore can severely affect the caving size, since the buckling stress increases with increase in the ellipticity index. Considering the case of a vertical well aligned with the directions of the in-situ stresses, and $\Delta\sigma_{cr}$ is 7500 psi and h is 0.1inch. a is half the major axis and b is half the minor axis.

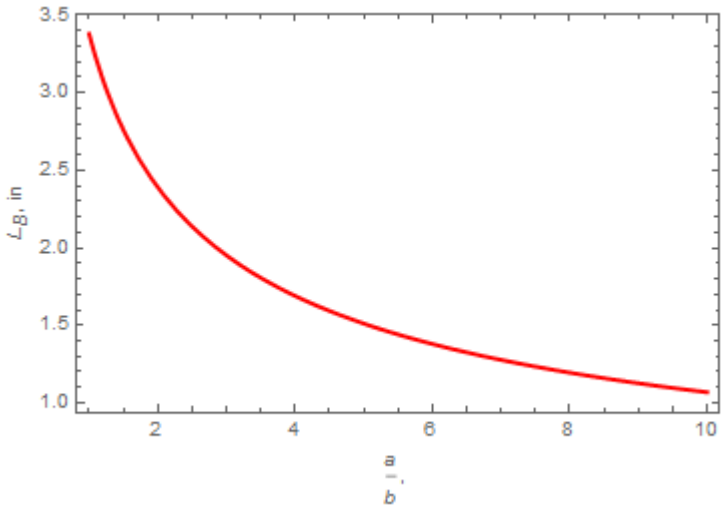

Fig. 3.12.Variation of caving size with borehole shape.

3.7.2 Parametric Studies on Rectangular Plate Approximation

As the size of the initial damage region around the wellbore (at the onset of borehole failure) increases, the size of caving produced during the breakout process

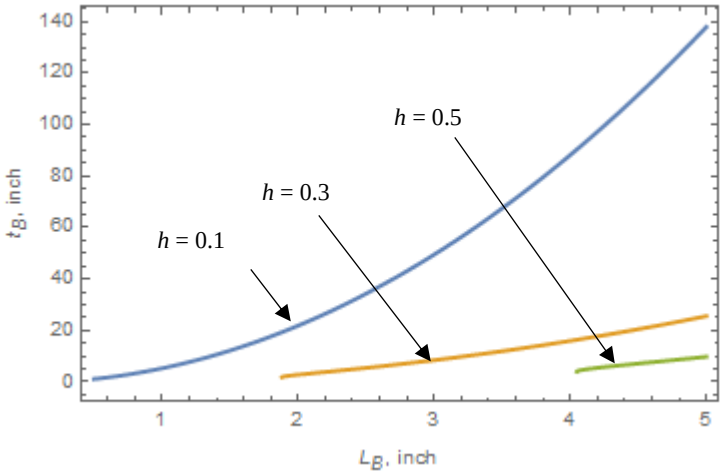

Fig. 3.13.Influence of the initial damage state on the size of caving produced. In this example case, the Elastic modulus of the formation is taken to be 145 Kpsi, Poisson ratio and Vertical stress are assumed to be 0.3 and 4000 psi respectively.

reduces (Fig. 13). This observation is in agreement with the findings of Germanovich and Dyskin (1999).

Based on the selected synthetic data, the minimum buckling length when h = 0.3in. is 1.8in. and the corresponding thickness of the plate is 0.1in. Thus, as observed in the figure, each limiting buckling thickness has its corresponding limiting buckling length, assuming all other parameters remain constant.

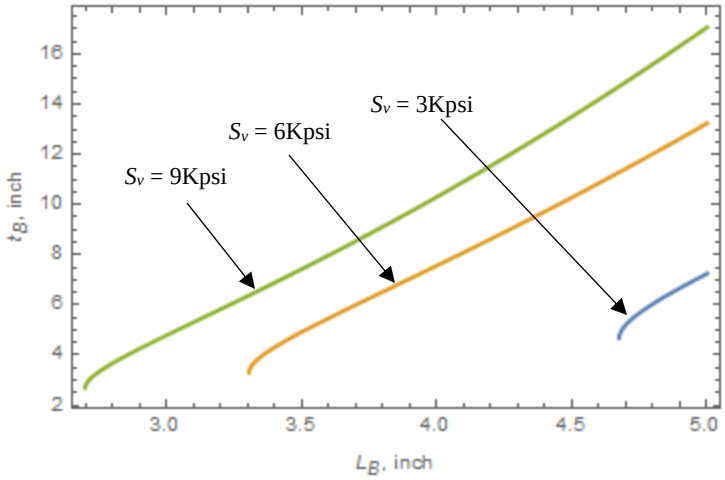

Fig. 3.14.Influence of in-situ stress loading on the size of caving produced. In this example case, *h*, Poisson ratio and elastic modulus are assumed to be 0.5in., 0.3, and 145Kpsi respectively.

In a normal faulting regime, in-situ stress increases with depth. From Fig. 3.14, it is expected that small cavings will be produced at deeper locations.

3.7.3 Effect of Back Stress on Unstable Crack Growth

The radial stress, which is termed back stress, acting on the propagating crack near the wellbore can significantly affect the size of caving produced and the failure process. As the length of the propagating crack increases, both the hoops and back stresses increase. But a small value of the back stress is sufficient enough to halt the unstable growth of the crack; Dyskin and Germanovich (1991) showed that the back stress required to stop the unstable crack growth is related to the hoops stress through

$$\sigma_{rr,c} = 0.199\frac{a_0}{h}\sigma_{\theta\theta} \quad \text{..... (3.17)}$$

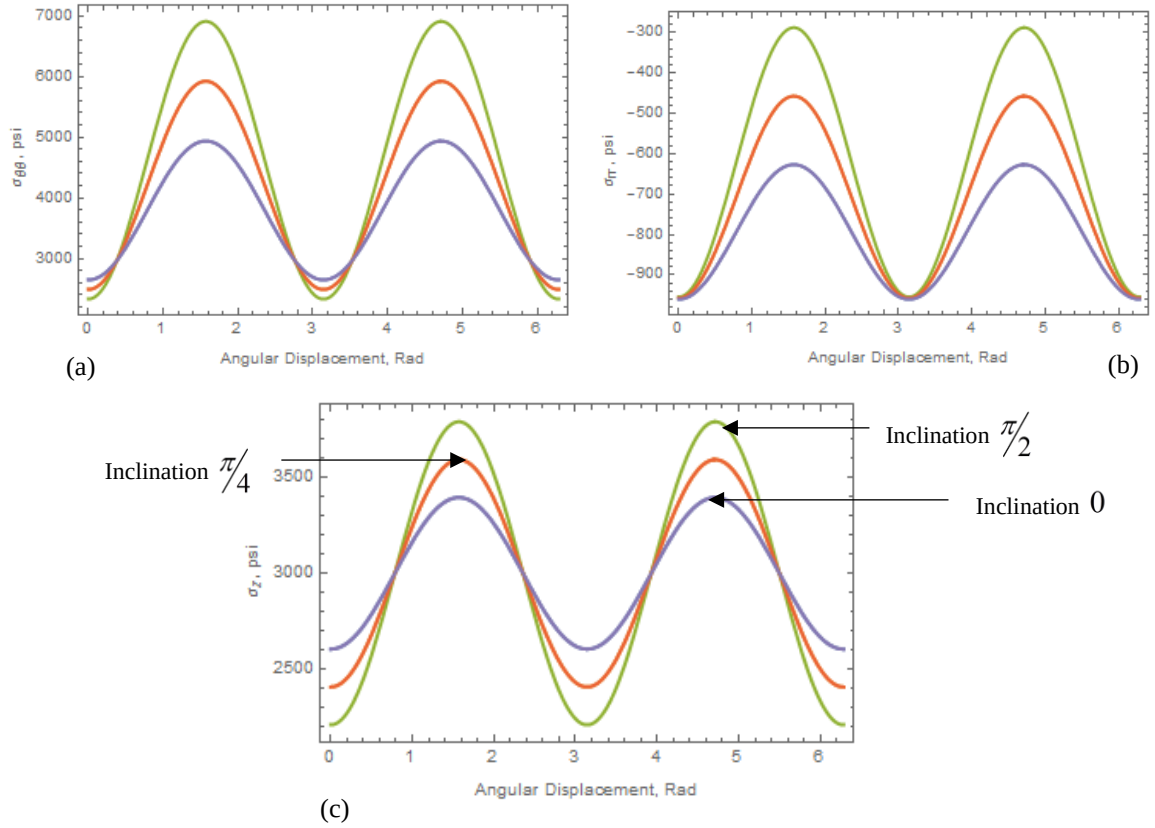

Fig. 3.15. Variation of (a) hoops stress, (b) radial stress, and (c) vertical stress around a circular wellbore with well angles. In this case A, the well azimuth is zero.

The authors assumed constant back stress in their numerical analyses to determine this empirical relation. In the synthetic cases below, the impacts of back stress is highlighted. As shown in Figs. 3.15 and 3.16 both the hoops and radial stresses increase as the inclination angle of the well increases, as well as the distance to the borehole reduces; the data in Tables 3.6 and 3.7 were used in plotting the curves in Figs. 3.15 and 3.16 respectively.

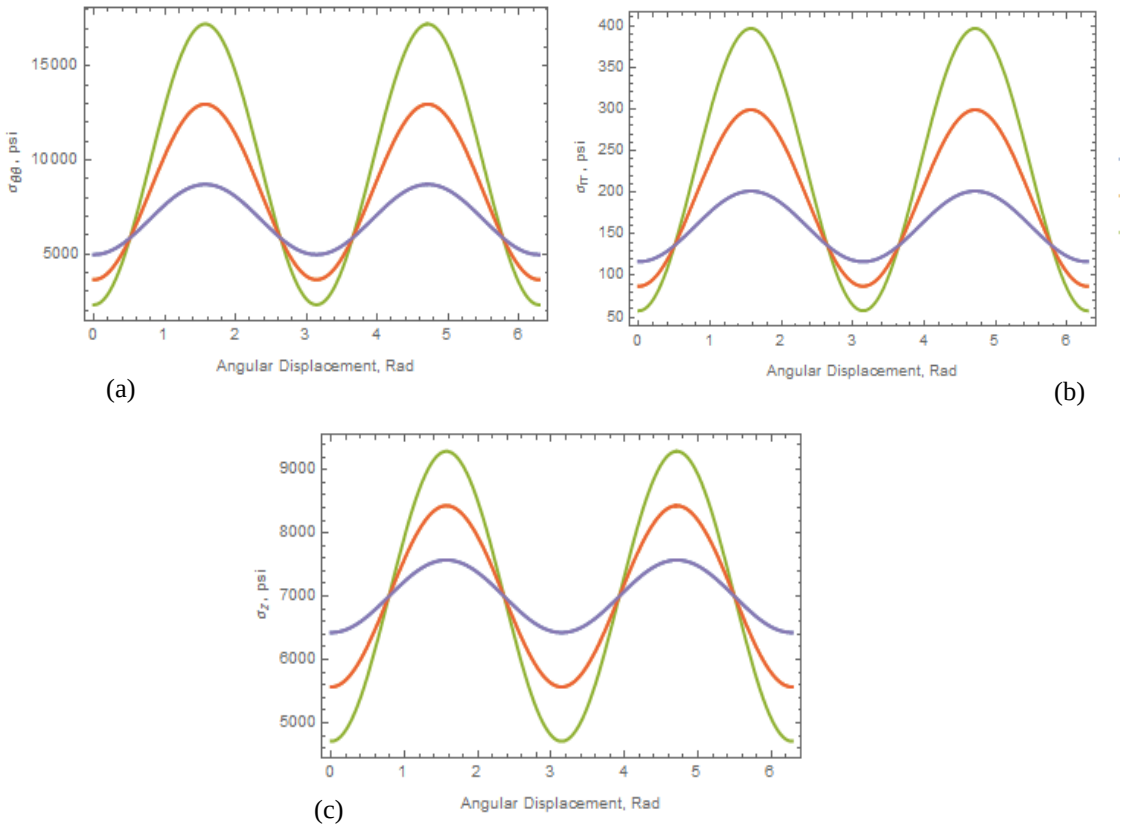

Fig. 3.16. Variation of (a) hoops stress, (b) radial stress, and (c) vertical stress around a circular wellbore with well angles. In this case B, the well azimuth is zero.

Vertical Stress, psi	9000
Minimum Horizontal Stress, psi	7000
Max. Horizontal Stress, psi	8500
Pore Pressure, psi	6000
Wellbore Pressure, psi	4000
Poisson Ratio	0.3
Wellbore Diameter, in	8.5
Distance of Crack to Boundary, *h*, in	1

Table 3.1. Stress state and mechanical properties of the formation for case A

Vertical Stress, psi	9000
Minimum Horizontal Stress, psi	5000
Max. Horizontal Stress, psi	6500
Pore Pressure, psi	2000
Wellbore Pressure, psi	2000
Poisson Ratio	0.3
Wellbore Diameter, in	8.5
Distance of Crack to Boundary, *h*, in	0.1

Table 3.2. Stress state and mechanical properties of the formation for case B

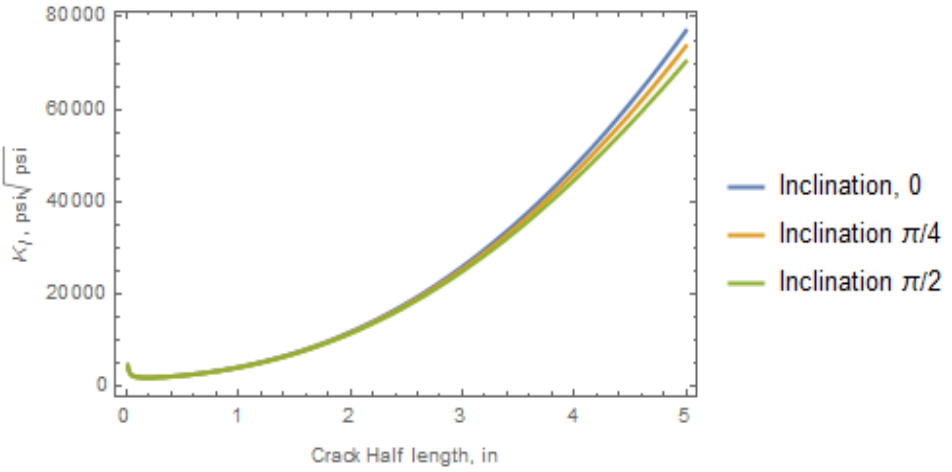

Fig. 3.17. Crack propagation in Case A.

A very low wellbore pressure will support the growth of unstable crack growth; this is no news, as many past studies on shear failure theory have shown that the borehole will have wider failure extent as the wellbore pressure falls below the critical collapse pressure.

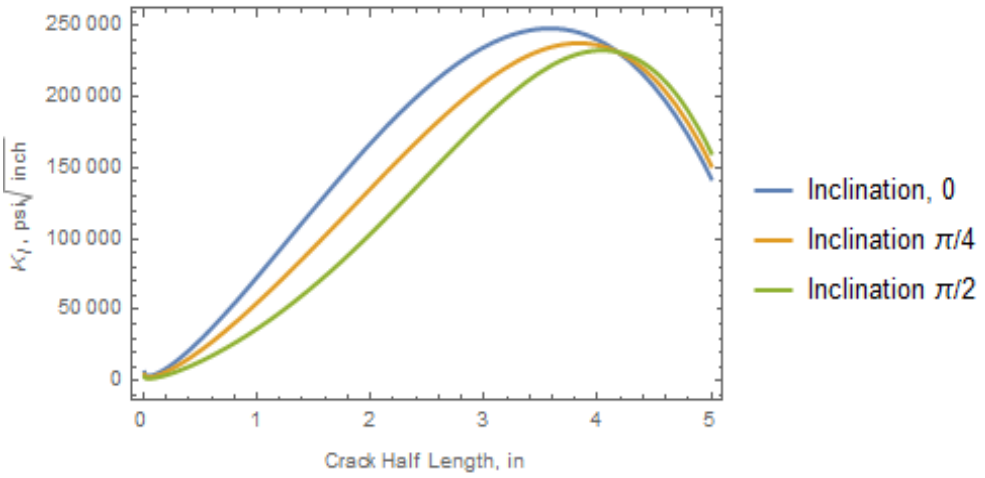

Fig. 3.18. Crack propagation and arrest in Case B.

From Fig. 3.17, the crack located at distance 1 inch from the wellbore boundary will propagate unstably, consequently, suggesting that the breakout depth is greater than 1 inch at this location. But in case B, the unstable crack propagation was halted after the crack has propagated a relatively distance around the borehole. The unstable propagation of crack around a vertical well will first be halted, as shown in Fig. 18. The implication of Fig. 18 is that borehole collapse potential increases with increase in well angle, although the size of cavings produced in highly deviated wells reduces with borehole inclination.

3.8 Summary

This paper presents a rigorous approach for estimating the geometry of caving produced during wellbore breakout. We assumed the geometry of the caving to be rectangular in shape, which is a reasonable approximation to the irregular-angular plates

often observed in the field. From extensive parametric studies conducted, the following conclusions are drawn:

1. As the size of initial damage region around the wellbore, prior to the onset of borehole failure, increases, the size of caving producible during the breakout process reduces.
2. As the wellbore shape changes from circular to elliptical, the size of caving producible reduces.
3. Assuming all other parameters remain the same, the size of caving reduces as the well inclination angle increases. But the potential for borehole failure increases with well inclination angle.

4. DEVELOPMENT OF AN ENERGY-CONSISTENT EROSION CONSTITUTIVE RELATION FOR DEFORMABLE POROUS MEDIA

4.1 Scope

In this paper an erosion constitutive law based on virtual power principle is derived. The law overcomes the limitation of the pressure gradient phenomenological constitutive law, currently being used in the industry today; it is valid for both rigid and mobile porous media. When the rigid porous medium assumption is made, the proposed constitutive law reduces to the form of the pressure-gradient phenomenological model; hence, the empirical parameter often called spatial frequency of erosion starter points is linked to physico-mechanical parameters. The study further developed constitutive equations of the damaged region around the wellbore during the erosion process. When the borehole is created in an isotropic elastic medium, the near well region is often damaged; the degree of damage greatly depends on the magnitudes of the in-situ stresses and the confining pressure. Plasticity theories, which are often used to describe the inelastic response of the damaged zone does not characterize the damage itself. But in this study, the nonlinear elastic and inelastic behaviors of the damaged zone are modeled using continuum damage theory. The generation of micro-cracks, which is a physical characterization of damage of the material, reduces its load bearing capacity. We further proved that the proposed constitutive law satisfies the principle of frame indifference if and only if the angular and linear momentum laws are satisfied. The proposed constitutive law and governing equations can be used to rigorously model reservoir and wellbore erosions during controlled and uncontrolled production of oil and gas.

4.2 Background on Wellbore Erosion

Solid particles (especially sand) production can be a nightmare during oil and gas production from unconsolidated sandstone formations; it erodes and damages subsurface and surface equipment. On the other hand, sand production around the producing well interval increases the production rate of the reservoir fluids. In addition, catastrophic sand production can help to bridge a blowing well. Hence, sand production can be "a menace or a hero", depending on the prevailing situation.

With 70% of oil reserves located in such formations, extensive research studies have been conducted to understand sand production mechanisms. Bratli and Risnes (1981), Perkins and Weingarten (1988), Vaziri (1988), and Morita et al. (1989) addressed the sand production as a wellbore stability problem, predicting the onset of sanding. But in recent years, starting with the work of Vardoulakis et al. 1996, sand production has since been treated as a three-phase fluid flow problem. Three-phase erosion kinetic equations, coupled with an erosion constitutive law define the tensile-sanding problem when geomechanical aspects of the problem are disregarded (Vardoulakis et al. 2000 and Scheuermann et al. 2001). Some other studies have coupled mechanical damage of the rock with sand erosion (Papamichos 2004, Stavropoulou et al. 1998, and Gravanis et al. 2016). Other studies on sand erosion are: a field study by Papamichos and Malmanger (2001), an experimental study by Papamichos (2006), and theoretical studies with modified erosion constitutive laws by Papamichos and Stavropoulou (1998), Wan et al. (2002), Wang et al. (2004), Vardoulakis and Papamichos (2003a and 2003b).

In all the past sand erosion studies, phenomenological erosion constitutive laws either based on filtration theories of Einstein (1937), Iwasaki (1937), and Sakthivadivel and Irmay (1966) or driven by pore pressure gradient. In a recent study by Papamichos (2010), the constitutive laws based on theories of filtration of fines through a coarse solid matrix and porosity diffusion models (Vardoulakis and Papamichos 2003a) do not agree with experiments. Only the phenomenological constitutive law driven by pressure gradient agrees with the experiment.

But in this study an erosion constitutive law based on virtual power principle is derived. The law overcomes the limitation of the pressure gradient phenomenological constitutive law; it is valid for both rigid and mobile porous media. When the rigid porous medium assumption is made, the proposed constitutive law reduces to the form of the pressure-gradient phenomenological model; hence, the empirical parameter often called spatial frequency of erosion starter points is linked to physico-mechanical parameters.

The study further developed constitutive equations of the damaged region around the wellbore, prior to erosion occurrence and during the erosion process. When the borehole is created in an isotropic elastic medium, the near well region is often damaged; the degree of damage greatly depends on the magnitudes of the in-situ stresses and the confining pressure. Plasticity theories are often used to describe the inelastic response of the damaged zone; this approach does not characterize the damage itself. But in this study, the nonlinear elastic and inelastic behaviors of the damaged zone are modeled using continuum damage theory. The generation of micro-cracks, which is a physical characterization of damage of the material, reduces its load bearing capacity. Many

authors have proposed different physical definition of damage: Rousselier (1981) proposed porosity as damage variable, Mudry (1983) used the radius of cavities and Lemaitre and Chaboche (1985) defined the damage variable as the relative area of micro-cracks and intersections of cavities in any plane oriented by its normal. And as stated by Kachanov (1986), the choice of the damage parameter can be by physical microstructural analysis or by direct generalization of experimental data. Lemaitre (1985), Lee et al. (1985), Celentano et al. (2004), Nichols and Abell (2003), Nichols and Totoev (1999), Voyiadjis and Kattan (1999, 2009), Voyiadjis (1988), and Voyiadjis (2011) used a more rational approach based on energy: the damage variable is defined as the ratio of the difference in the elastic moduli to the damaged modulus. In this approach, a damage function, and a generalized thermodynamic force associated with the damage are often derived. And using consistency condition and mathematical optimization technique, the relationship between damage and the strain is developed.

Introduction of effective stress concept by Kackanov (1958) pioneered continuum damage mechanics. And several engineering failure analyses have been conducted by many authors through this theory. Krajcinovic (1983, 1985), Krajcinovic and Foneksa (1981), Ju and Lee (1991), and Ju and Chen (1994a and 1994b) worked on the brittle fracture of engineering materials. And Lemaitre (1985 and 1986), Chaboche (1979, 1981, 1988a, and1988b), and Chow and Wang (1987) applied the theory to ductile failure of engineering materials. Similarly, the effective stress concept will be used in this study to characterize the impacts of damage on the elastic properties of the formations.

And when the damaged rock formation is being eroded, the elastic properties of the formation are further degraded. Therefore, the damage variable is assumed to be the superposition of the erosion induced porosity and the total volumetric strain due to mechanical damage. Papamichos et al. (2001) conducted experimental studies that confirmed that the volumetric strain change describes a second order effect, which Lord Kelvin (1875) and Reiner (1947) had identified to be the cause of cracking in rocks. Similarly, Brace et al. (1966) had performed similar experiments and had showed that the volumetric strain due to cracking is equal to the induced porosity in the damaged material body. Therefore, the superposition of the two induced porosities is reasonable, as supported by these experiments.

Both erosion and mechanical damage of the rock due to stress concentration are coupled through the damage variable. This simply means that since stress concentration leads to reduced strength of the rock against the seepage forces, the amount of grains leaving the rock matrix increases. And as the erosion process proceeds, the strength of the rock reduces. The reduction in the strength of the rock can lead to shear failure of the rock; thus, increasing the volume of solid particles being transported into the borehole. As the borehole diameter increases, because of shear failure and erosion, the stress concentration around the enlarged borehole section also increases. But if rock compaction exceeds cracking, thence, the degree of damage of the region around the wellbore reduces. Consequently, the erosion potential around the borehole should reduce, although an increased borehole diameter increases the seepage forces acting on the grains.

In summary, the main objectives of this article are: (1) to develop a comprehensive erosion constitutive relation for deformable porous media and (2) to determine the critical erosion hydraulic gradient.

4.3 Erosion Constitutive Law for Deformable Porous Media

4.3.1 Definition of Terms

Following Vardoulakis et al. (1996) three-phase erosion kinetic model, the bulk erosion-induced porosity at the current configuration of the porous material body is defined as

$$\phi = \frac{\mathrm{dV_v}}{\mathrm{dV}} \quad \text{..... (4.1)}$$

where $\mathrm{dV_v}$ is the volume of interconnected voids created by erosion only and dV is the representative volume element. The concentration of solid grains leaving the matrix of the rock due to erosion is

$$c = \frac{\mathrm{dV_{fs}}}{\mathrm{dV_v}} \quad \text{..... (4.2)}$$

$\mathrm{dV_{fs}}$ is the volume of the fluidized particles, and the bulk density of the fluidized particles and fluid mixture is

$$\bar{\rho} = c\rho_s + (1-c)\rho_f \quad \text{..... (4.3)}$$

As derived by Oyedokun and Schubert (2017), the volumetric strain due to the second order effects in an isotropic elastic material body, which is subjected to polyaxial loading is

$$d\psi = \frac{\sigma_m}{K} + \frac{\alpha_4}{4KG^2}\left\{\begin{array}{l}(\sigma_1-\sigma_2)^2\left[\dfrac{(\sigma_1-\sigma_2)}{(\sigma_1-\sigma_2)^*}\right]^{2n} + (\sigma_1-\sigma_3)^2\left[\dfrac{(\sigma_1-\sigma_3)}{(\sigma_1-\sigma_3)^*}\right]^{2n} \\ -(\sigma_1-\sigma_2)(\sigma_1-\sigma_3)\left[\dfrac{(\sigma_1-\sigma_2)}{(\sigma_1-\sigma_2)^*}\right]^{n}\left[\dfrac{(\sigma_1-\sigma_3)}{(\sigma_1-\sigma_3)^*}\right]^{n}\end{array}\right\} \quad \text{..... (4.4)}$$

σ_m is the mean normal stress, α_4 and n are empirical constants that are determined from experiment, K, is the bulk modulus of the material body, and G is the shear modulus of the material body.

The damage variable is thus defined as

$$D = \phi + d\psi \quad \text{..... (4.5)}$$

4.3.2 Derivation of the Energy-Consistent Erosion Constitutive Law

Consider a part Ω_0 in the reference configuration of a material body, B. After time t, the material body has a different configuration, B_t, due to a homogeneous motion; the new configuration of the part, Ω_t, also follows the same motion as the region B_t. The removal of the material points in the deformed configuration is not described by the smooth function $\chi_s(\boldsymbol{X}, t)$ that maps a material point in the reference configuration to the corresponding spatial point in the deformed configuration; the mapping is one-to-one. Erosion process transports the particle occupying the spatial point through a different mapping function, which is not a subject of discussion in this article.

The removal of solid-grains from the matrix by erosion occurs through a shearing action (Partheniades 1965, Zreik et al. 1998, Mehta 1991, and Khilar et al. 1985).

Therefore, the resistive power against erosion of the matrix in the current configuration is proposed as

$$\frac{d}{dt}\int_{\Omega_t} \mathbf{T}.\mathbf{I}\,\rho_S \delta\phi \, d\Omega \quad \text{..... (4.6)}$$

T is the total shearing resistive force against the removal of the grains, in the current/deformed configuration; this stress measure is the Cauchy stress. From linearized Mohr-Coulomb failure theory (Jaeger and Cook 1979), the shear strength can be represented as the superposition of the cohesion and frictional strength of the rock:

$$\mathbf{T} = \mathbf{C} + \boldsymbol{\sigma} \tan\varphi \quad \text{..... (4.7)}$$

C is the cohesive strength of the rock, $\boldsymbol{\sigma}$ is the effective normal stress acting on the grains, and φ is the angle of internal friction. The rate of work done in removing δc concentration of particles across the boundary of the material body in the current configuration is

$$\int_{\Gamma_t} \left(p - p_C\right)\rho_S \, \delta c \, \mathbf{v}_S . \mathbf{n} \, d\Gamma \quad \text{..... (4.8)}$$

where p_C is the critical pressure required to unseat the grains, and the velocity of the fluidized particles is $\mathbf{v}_S$. It should be noted that the difference between the prevailing fluid pressure and the critical erosion pressure is equal to the difference of the fluid Cauchy stress and the critical erosion Cauchy stress; mathematically this is represented as

$$p - p_C = \mathbf{T}^f - \mathbf{T}_c^f \quad \text{..... (4.9)}$$

The inertial power expended due to the removal of δc concentration of the particles across the boundary of the material body in the current configuration is

$$\frac{d}{dt}\int_{\Omega_t}\frac{\rho_s}{2}\delta c\,\mathbf{v}_s^2\,d\Omega \quad \text{..... (4.10)}$$

Proposition 1. The Cauchy stress difference is equal to the pressure difference

Proof. The Cauchy stress of the fluid is defined as

$$\mathbf{T}^f = -p\mathbf{I} + 2\mu_e\mathbf{D}^f \quad \text{..... (4.11)}$$

The assumption is that the fluid behavior is Newtonian; even when the concentration of fluidized particles in the void space is greater than zero, an effective viscosity, μ_e, which is based on linear mixture of the different species in the flow stream, is used, and the behavior of the non-Newtonian fluid can be represented by the equivalent-Newtonian stress. Suppose the critical Cauchy stress that initiates erosion is defined as

$$\mathbf{T}_c^f = -p_c\mathbf{I} + 2\mu_e^c\hat{\mathbf{D}}_c^f\left(\mathbf{D}^f\right) \quad \text{..... (4.12)}$$

where $p_c, \mu_e^c,$ and $\mathbf{D}_c{}^f$ are the critical erosion pressure, critical-equivalent viscosity of the fluid, and the critical strain rate function of the fluid.

Material constitutive law are based on dynamical processes. Letting the constitutive class of the fluid be defined by $\mathbb{C}$. By considering a simple kinematical constraint such that

$$\gamma(\bullet):\mathrm{Lin}^+ \to \Re \quad \text{..... (4.13)}$$

Where $\mathrm{Lin} = \{\text{all linear transformations on } \Re^3\}$, and $\mathrm{Lin}^+ = \{\mathbf{L} \in \mathrm{Lin}, \det(\mathbf{L}) > 0\ \}$. The dynamical process $(\chi_f, \mathbf{T}^f) \in \mathbb{C}$ satisfies $\gamma(\mathbf{F}^f) = 0$. The constraint axiom of a material body is that, if $(\chi_f, \mathbf{T}^f) \in \mathbb{C}$ then $(\chi_f, \mathbf{T}^f + \mathbf{N}^f) \in \mathbb{C}$, where $\mathbf{D}^f.\mathbf{N}^f = 0$, for all $\mathbf{D}^f$ consistent with the constraint $\gamma(\mathbf{F}^f) = 0$. It is noted that stress power associated with a process $(\chi_f, \mathbf{T}^f)$ is $\mathbf{T}^f.\mathbf{D}^f$**.** In the same vein, for the dynamical process $(\chi_f, \mathbf{T}^f + \mathbf{N}^f)$,

the stress power should be $(\mathbf{T}^f + \mathbf{N}^f).\mathbf{D}^f$**.** For the constraint axiom of the material body to be valid, it thus implies that $(\mathbf{T}^f + \mathbf{N}^f).\mathbf{D}^f = \mathbf{T}^f.\mathbf{D}^f$. Consequently, it can be inferred that **N** does no work for allowable motions. Considering the idea that

$$\frac{d}{dt}\gamma(\mathbf{F}^f) = 0 \quad \text{..... (4.14)}$$

Assuming incompressibility,

$$\gamma(\mathbf{F}^f) = \det(\mathbf{F}^f) - 1 \quad \text{..... (4.15)}$$

Hence,

$$\frac{d}{dt}\gamma(\mathbf{F}^f) = \det(\mathbf{F}^f)\,\mathrm{tr}\left[\dot{\mathbf{F}}^f\left(\mathbf{F}^f\right)^{-1}\right] = \det(\mathbf{F}^f)\left(\mathbf{D}^f.\mathbf{I}\right) \quad \text{..... (4.16)}$$

for all admissible $\mathbf{D}^f$. It thus implies that $\mathbf{D}^f.\pi\mathbf{I} = 0$, where π is an arbitrary scalar value. Hence, $\{\mathbf{N}^f\} = \{\pi\mathbf{I}\}$. Knowing the constraint $\mathrm{tr}(\mathbf{D}^f) = 0$, thus implies incompressibility. Therefore, $(\chi_f, \mathbf{T}^f) \in \mathbb{C} \Longrightarrow (\chi_f, \mathbf{T}^f - \pi\mathbf{I}) \in \mathbb{C}$ for all $\pi \in \Re$. The implication of this conclusion is that two incompressible fluids, which are undergoing the same dynamical process, are equivalent if and only if their dissipative powers are the same. As a consequence of this constraint and conclusion, it thus implies that $2\mu_e\mathbf{D}^f = 2\mu_e^c\,\widehat{\mathbf{D}}_c{}^f$, $\forall\ \mathbf{D}^f \neq 0$.

Also, when the fluid constitutive class is Eulerian, the proposition above holds; there is no need to prove that, as Eq. 4.9 defines the statement.

Power Balance. Thus from the foregoing, the total power required to remove δc concentration of particles from the matrix of the porous material should be equal to the rate of work done in creating $\delta\phi$ porosity in the matrix plus the inertial power expended

in transporting δc concentration of particles away from the matrix, and the power expended by the conventional body force. Mathematically, this law can be expressed in the current configuration of the material body as

$$\int_{\Omega_t} \delta c\, \mathbf{b}_0 . \mathbf{v}_s \, \mathrm{d}\Omega + \frac{d}{dt}\int_{\Omega_t} \frac{\rho_s}{2} \delta c\, \mathbf{v}_s^2 \, \mathrm{d}\Omega + \frac{d}{dt}\int_{\Omega_t} \mathbf{T}.\mathbf{I}\rho_s \delta\phi \, \mathrm{d}\Omega = \int_{\Omega_t} \left(p - p_c\right)\rho_s \delta c\, \mathbf{v}_s . \mathbf{n} \mathrm{d}\Gamma \quad \text{..... (4.17)}$$

It should be noted that the conservation equation above is not limited to a rigid porous medium. If the velocity of the matrix is $\mathbf{v}_m$, the relative velocity of the fluidized particles is thus

$$\mathbf{v}_s = \mathbf{v}_{s,a} + \mathbf{v}_m \quad \text{..... (4.18)}$$

$\mathbf{v}_{s,a}$ is the absolute particle velocity.

Proposition 2. The proposed power balance law is frame indifferent if and only if the linear and angular momentum laws are satisfied

Proof. A basic principle underlying any physical law is that it must be frame-indifferent. The Cauchy stress $\tilde{\mathbf{T}}$ in a different frame is related to the Cauchy stress in the "old" frame through

$$\tilde{\mathbf{T}} = \mathbf{Q}\mathbf{T}\mathbf{Q}^T \quad \text{..... (4.19)}$$

Q(t) is a rotation tensor. There has been some controversies as to whether only rotations or all orthogonal tensors should be used when referring to the frame-indifference principle. Truesdell and Noll (1965) stated that the tensor should be an orthogonal tensor, while Chadwick (1976) and Gurtin (1981) argued that it should be a rotation. As concluded by Murdoch (2003), we also claim that the tensor should be a rotation tensor.

In the same vein, the outward unit normal vector is also transformed accordingly as

$$\tilde{\mathbf{n}} = \mathbf{Q}\mathbf{n} \quad \text{..... (4.20)}$$

The velocity is known not to be frame-indifferent, and its transformation is

$$\tilde{\mathbf{v}}_S = \mathbf{Q}\mathbf{v}_S + \dot{\mathbf{y}} + \dot{\mathbf{Q}}\chi_S \quad \text{..... (4.21)}$$

$\mathbf{y}(t)$ is a spatial point at each fixed time *t*. By substituting equations (4.19) into (4.17) yields

$$\begin{aligned}\frac{d}{dt}\int_{\tilde{\Omega}_t} \tilde{\mathbf{T}}.\mathbf{I}\tilde{\rho}_S\delta\tilde{\phi}\,\mathrm{d}\Omega &= \frac{d}{dt}\int_{\Omega_t} \mathbf{Q}\mathbf{T}\mathbf{Q}^{\mathrm{T}}.\mathbf{Q}\mathbf{Q}^{\mathrm{T}}\rho_S\delta\phi\,\mathrm{d}\Omega \\ &= \frac{d}{dt}\int_{\Omega_t} \mathbf{T}.\mathbf{I}\rho_S\delta\phi\,\mathrm{d}\Omega\end{aligned} \quad \text{..... (4.22)}$$

Noting that, $\tilde{\rho}_s = \rho_s$ and $\tilde{\phi} = \phi$. Similarly, substituting equations (4.20) and (4.21) into (4.17) yields

$$\begin{aligned}&\int_{\tilde{\Gamma}_t}\left(\tilde{p}-\tilde{p}_C\right)\tilde{\rho}_S\,\delta\tilde{c}\,\tilde{\mathbf{v}}_S.\tilde{\mathbf{n}}\,\mathrm{d}\Gamma - \frac{d}{dt}\int_{\tilde{\Omega}_t}\frac{\tilde{\rho}_S}{2}\delta\tilde{c}\,\tilde{\mathbf{v}}_s^2\,\mathrm{d}\Omega - \int_{\Omega_t}\delta c\,\mathbf{b}_0.\mathbf{v}_S\,\mathrm{d}\Omega \\ &= \int_{\Gamma_t}\left(p-p_C\right)\rho_S\,\delta c\,\mathbf{n}.\left[\mathbf{v}_S+\mathbf{Q}^{\mathrm{T}}\,\dot{\mathbf{y}}+\mathbf{Q}^{\mathrm{T}}\dot{\mathbf{Q}}\,\chi_S\right]\mathrm{d}\Gamma + \int_{\Omega_t}\delta c\,\mathbf{b}.\left[\mathbf{v}_S+\mathbf{Q}^{\mathrm{T}}\,\dot{\mathbf{y}}+\mathbf{Q}^{\mathrm{T}}\dot{\mathbf{Q}}\,\chi_S\right]\mathrm{d}\Omega \\ &= \int_{\Gamma_t}\left(p-p_C\right)\rho_S\,\delta c\,\mathbf{n}.\left[\mathbf{v}_S+\mathbf{w}_S\right]\mathrm{d}\Gamma + \int_{\Omega_t}\delta c\,\mathbf{b}.\left[\mathbf{v}_S+\mathbf{w}_S\right]\mathrm{d}\Omega\end{aligned} \quad \text{(4.23)}$$

where, $\mathbf{w}_s = \mathbf{Q}^{\mathrm{T}}\,\dot{\mathbf{y}} + \mathbf{Q}^{\mathrm{T}}\dot{\mathbf{Q}}\,\chi_s$ is a rigid velocity field and **b** is the generalized body force; noting that $\mathbf{Q}^{\mathrm{T}}\dot{\mathbf{Q}}$ is a skew tensor. Let

$$\tilde{W}\left(\tilde{p},\tilde{\mathbf{v}}_S\right) = \int_{\tilde{\Gamma}_t}\left(\tilde{p}-\tilde{p}_C\right)\tilde{\rho}_S\,\delta\tilde{c}\,\tilde{\mathbf{v}}_S.\tilde{\mathbf{n}}\,\mathrm{d}\Gamma + \int_{\tilde{\Omega}_t}\delta\tilde{c}\,\tilde{\mathbf{b}}.\tilde{\mathbf{v}}_s\,\mathrm{d}\Omega \quad \text{..... (4.24)}$$

$$W\left(p,\mathbf{v}_S\right) = \int_{\Gamma_t}\left(p-p_C\right)\rho_S\,\delta c\,\mathbf{n}.\mathbf{v}_s\,\mathrm{d}\Gamma + \int_{\Omega_t}\delta c\,\mathbf{b}.\mathbf{v}_s\,\mathrm{d}\Omega \quad \text{..... (4.25)}$$

and

$$W_g\left(p,\mathbf{w}_S\right)=\int_{\Gamma_t}\left(p-p_C\right)\rho_S\,\delta c\,\mathbf{n}\,.\,\mathbf{w}_s\,\mathrm{d}\Gamma+\int_{\Omega_t}\delta c\,\mathbf{b}.\,\mathbf{w}_s\,\mathrm{d}\Omega \quad \text{..... (4.26)}$$

For frame indifference, it is required that

$$W\left(p,\mathbf{v}_S\right)=\tilde{W}\left(p,\tilde{\mathbf{v}}_S\right) \quad \text{..... (4.27)}$$

But from Eq. 4.21,

$$\tilde{W}\left(p,\tilde{\mathbf{v}}_S\right)=W\left(p,\mathbf{v}_S\right)+W_g\left(p,\mathbf{w}_S\right) \quad \text{..... (4.28)}$$

By letting $\boldsymbol{\alpha}=\mathbf{Q}^{\mathrm{T}}\dot{\mathbf{y}}$ and $\boldsymbol{\lambda}$ denoting the axial vector corresponding to the skew tensor $\mathbf{Q}^{\mathrm{T}}\dot{\mathbf{Q}}$, then

$$W_g\left(p,\mathbf{w}_S\right)=\int_{\Gamma_t}\rho_S\,\delta c\left\{\Delta\mathbf{T}^f\mathbf{n}\,.\,\boldsymbol{\alpha}+\boldsymbol{\lambda}\,.\left(\Delta\mathbf{T}^f\mathbf{n}\times\mathbf{r}\right)\right\}\mathrm{d}\Gamma+\int_{\Omega_t}\delta c\left\{\mathbf{b}\,.\,\boldsymbol{\alpha}+\boldsymbol{\lambda}\,.\left(\mathbf{b}\times\mathbf{r}\right)\right\}\mathrm{d}\Omega \quad (4.29)$$

From the balances of linear and angular momentum, the power expended on the sub-region Ω_t over the rigid velocity field $\mathbf{w}_s$ is zero, if and only if the linear and angular momentum balances are satisfied and **n** is the inward unit normal vector fields on $\partial\Omega_t(=\Gamma_t)$, but outward unit normal vector field on the fluid domain . Consequently, the proposed balance law will be frame-indifferent.

Remark. From the foregoing, it is evident that the impact of fluid viscosity in an erosion process, especially when the particles are loose is insignificant. The pressure difference across the grain is more significant; this is the same conclusion drawn by Papamichos (2010) in his experimental and theoretical studies. In the event the particles are not loose, then erosion potential increases as the viscosity of the fluid increases. On the contrary, if the power supply to the system remains the same, the flow velocity reduces and the erosion

potential reduces. These two phenomena counteract each other, and the dominant effect wins.

Using Reynolds transport and divergence theorems, Eq. 4.15 becomes

$$\int_{\Omega_0}\left\{\frac{\partial}{\partial t}\left(\mathbf{T}_m\mathbf{F}^{-T}.\mathbf{I}\,\rho_s\frac{\delta\Phi}{\det(\mathbf{F})}\det(\mathbf{F})\right)+\mathbf{T}_m\mathbf{F}^{-T}.\mathbf{I}\,\rho_s\delta\Phi\,\mathrm{tr}(\mathbf{L})\right\}\det(\mathbf{F})\,d\Omega$$
$$=\int_{\Omega_0}\nabla.\left[\left(p-p_C\right)\rho_s\delta C\,\mathbf{v}_s\right]\det(\mathbf{F})\,d\Omega-\int_{\Omega_0}\delta C\,\mathbf{b}.\mathbf{v}_s\det(\mathbf{F})\,d\Omega \quad \text{..... (4.30)}$$

F is the deformation gradient and $\mathbf{T}_m$ is the material description of the Cauchy stress **T**. The porosity of the porous medium referenced to the deformed configuration is related to the undeformed configuration through the relation $\delta\phi = \det(\mathbf{F})\,\delta\Phi$, for any arbitrary volume of the continuum. Similarly, the first Piola-Kirchhoff stress, **S**, is related to the Cauchy stress $\mathbf{T}_m$ through the relation $\mathbf{S} = \det(\mathbf{F})\mathbf{T}_m\mathbf{F}^{-T}$; by substituting this relation in Eq. 4.30, yields

$$\int_{\Omega_0}\frac{\partial}{\partial t}\left(\mathbf{S}.\mathbf{I}\,\rho_s\frac{\delta\Phi}{\det(\mathbf{F})}\right)\det(\mathbf{F})+\mathbf{S}.\mathbf{I}\,\rho_s\delta\Phi\,\mathrm{tr}(\mathbf{L})\;d\Omega$$
$$=\int_{\Omega_0}\nabla.\left[\left(p-p_C\right)\rho_s\delta C\,\mathbf{v}_s\right]\det(\mathbf{F})\,d\Omega-\int_{\Omega_0}\delta C\,\mathbf{b}.\mathbf{v}_s\det(\mathbf{F})\,d\Omega \quad \text{..... (4.31)}$$

Since Eq. 4.30 is valid for any arbitrary volume of the continuum, the local form of the erosion constitutive equation is,

$$\frac{\partial}{\partial t}\left(\mathbf{S}.\mathbf{I}\,\rho_s\frac{\delta\Phi}{\det(\mathbf{F})}\right)=\nabla.\left[\left(p-p_C\right)\rho_s\delta C\,\mathbf{v}_s\right]-\mathbf{S}.\mathbf{I}\,\rho_s\frac{\delta\Phi}{\det(\mathbf{F})}\mathrm{tr}(\mathbf{L})-\delta C\,\mathbf{b}.\mathbf{v}_s \quad \text{..... (4.32)}$$

And assuming the density of the solid grain is constant, which is valid for geomaterials, the erosion constitutive equation becomes

$$\frac{\partial}{\partial \mathrm{t}}\left(\rho_{\mathrm{S}}\Phi\right)=\frac{1}{\mathbf{S.I}}\begin{Bmatrix}\nabla.\left[\left(p-p_{C}\right)\rho_{\mathrm{S}}\delta C\,\mathbf{v}_{S}\right]\det\left(\mathbf{F}\right)-\mathbf{S.I}\,\rho_{\mathrm{S}}\delta\Phi\,\mathrm{tr}(\mathbf{L})\\-\delta C\,\mathbf{b}.\mathbf{v}_{S}\det\left(\mathbf{F}\right)-\delta\Phi\rho_{\mathrm{S}}\dfrac{\partial}{\partial \mathrm{t}}\left(\dfrac{\mathbf{S.I}}{\det\left(\mathbf{F}\right)}\right)\det\left(\mathbf{F}\right)\end{Bmatrix} \quad \text{..... (4.33)}$$

For an isochoric erosion process, time independent shear strength, $\frac{\partial S}{\partial t}=0$, rigid/immobile porous matrix, and neglecting the power expended by the generalized body force, Eq. 4.33 reduces to the form of the phenomenological model proposed by Papamichos (2004); supposing the initial concentration of particles in the void space is zero

$$\frac{\partial\Phi}{\partial \mathrm{t}}=\frac{1}{\mathbf{S.I}}\nabla.\left[\left(p-p_{C}\right)C\,\mathbf{v}_{S}\right] \quad \text{..... (4.34)}$$

By comparing Papamichos' phenomenological model,

$$\frac{\partial\Phi}{\partial \mathrm{t}}=\lambda_{p}\nabla\left(p-p_{C}\right) \quad \text{..... (4.35)}$$

with Eq. 4.32, it is obvious that the erosion starter parameter, which is

$$\lambda_{p}=\frac{C\,\mathbf{v}_{S}}{\mathbf{S.I}} \quad \text{..... (4.36)}$$

is valid, if and only if there is no spatial variation of the concentration of the fluidized particles and velocity of the fluidized particles is also spatially independent. This rigorous derivation has shown the deficiency in the phenomenological model; some of the authors highlighted in the introduction made λ_p a function of porosity, to capture other inherent nonlinearities. But near the boundary (borehole wall), where the concentration of the fluidized particles and flow velocity are almost constant, the phenomenological model will be valid.

4.4 Derivation of Critical Erosion Hydraulic Gradient

To account for the pressure drops due to shearing action between the fluid and the fluidized particles and non-Darcy flow behavior around the wellbore, Brinkman (1947) and Forchheimer modifications of Darcy's law are introduced respectively

$$\mathbf{v}_{\mathrm{f}} = -\frac{k}{\eta\bar{\rho}}\left\{\nabla p - \bar{\rho}g - \eta\bar{\rho}\nabla\cdot\nabla\left(\frac{\mathbf{v}_{\mathrm{f}}}{D}\right) - \beta_F \bar{\rho}\,\mathbf{v}_{\mathrm{f}}{}^2\right\} \quad \text{..... (4.37)}$$

D is the total porosity in the matrix, due to both erosion and mechanical damage. According to Brinkman, the drag force on a spherical particle, considering the influence of other surrounding particles on the particle, is

$$\mathbf{F}_{\mathrm{d}} = 3\pi\eta\bar{\rho}\mathbf{v}_{\mathrm{f}} d_p\left\{1+\alpha\frac{d_p}{2}+\alpha^2\frac{d_p{}^2}{12}\right\} \quad \text{..... (4.38)}$$

and the force due to pressure differential across the grain is

$$\mathbf{F}_{\mathrm{p}} = -\frac{4}{3}\pi\frac{d_p{}^3}{8}\nabla p \quad \text{..... (4.39)}$$

Thus, the total force acting to unseat the grain is $\mathbf{F_T} = \mathbf{F}_{\mathrm{d}} + \mathbf{F}_{\mathrm{p}}$.

The virtual power required to force the grain out of the rock matrix should be equal to the restraining power, provided energy dissipated due to cracking, sliding, or rolling of the grains are neglected,

$$\mathbf{S}\cdot N_C A_C \vec{\mathbf{n}}\,\delta\mathbf{v}_{\mathrm{s}} = \mathbf{F}_T\cdot\delta\mathbf{v}_{\mathrm{s}} \quad \text{..... (4.40)}$$

Eq.4.39 assumes that all contact areas with the particle are equal. A_C is the contact area between two particles, as shown in Fig. 4.1.

Therefore, substituting equations 4.37, 4.38, and 4.39 into 4.40, the critical erosion hydraulic gradient is

$$\left|\nabla p_c\right| = \left| \frac{1}{\frac{1}{6}\pi \mathrm{d_p}^3} \left(\mathrm{S} N_c A_c - \mathrm{F_d} \right) \right| + \rho_s g \quad \text{..... (4.41)}$$

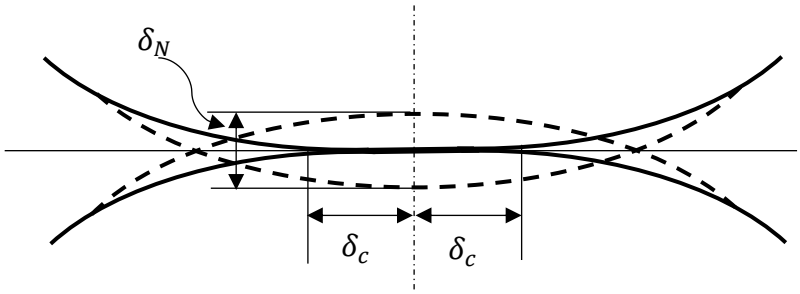

Fig. 4.1. Geometry of two spherical particles elastically deforming in contact. The dashed line represents the undeformed surface of each particle.

$$A_c = \pi \delta_c{}^2 \quad \text{..... (4.42)}$$

Where the radius of contact is

$$\delta_c = \sqrt{\frac{d_p}{2} \delta_N} \quad \text{..... (4.43)}$$

And using Betti reciprocity theorem, the normal overlap is

$$\delta_N = \frac{\sigma d_p (1 - 2\nu)}{E} \quad \text{..... (4.44)}$$

Considering an application to the petroleum industry, where the erosion of the borehole is severe due to high pressure gradient. As the diameter of the wellbore increases, the drag forces acting on the intact grains increases; also, the stress concentration around the wellbore increases. But depending on the degree of damage on the shear strength of the matrix, the critical erosion hydraulic gradient can either increase or decrease. Farther into the formation, where erosion has not occurred, and the second order effects are negligibly compared to the compaction of the matrix, erosion potential is significantly low because the critical hydraulic gradient will increase. Even nearer to the borehole wall, where erosion potential can be high, if compaction rate is faster than the rate of erosion, the critical hydraulic gradient will increase. This could be the reason why erosion-induced sand production will not continue indefinitely.

4.5 Three-Phase Erosion Governing Equations

The mass-balance equations for the three phases in the foregoing problem are fluid, fluidized-particles, and the solid skeleton. Considering the solid skeleton, the mass balance for this species in the porous medium is

$$\frac{\partial}{\partial t}(1-\Phi)\rho_S + \nabla\cdot(1-\Phi)\rho_S\vec{v}_m = -\dot{m} \quad \text{..... (4.45)}$$

Similarly, the mass-balance equation for the fluidized particles is

$$\frac{\partial}{\partial t}c\Phi\rho_S + \nabla\cdot c\rho_S\vec{v}_f - \nabla\cdot\left(\mathbf{D}_p\nabla\Phi c\rho_S\right) = \dot{m} \quad \text{..... (4.46)}$$

$\boldsymbol{D}_p$ is the dispersion tensor, which will be very significant when considering axial erosion along the wellbore. $\dot{m}$ is the net mass rate of eroded particles; in the event the deposition of the particles in the porous medium is significant, the deposition rate will be subtracted

from the erosion mass rate. In this study, the mass of particles deposited back into the porous medium is insignificant. Finally, the mass balance for the fluid phase is

$$\frac{\partial}{\partial t}(1-c)\Phi\rho_{\mathrm{f}} + \nabla.(1-c)\rho_{\mathrm{f}}\mathbf{v}_{\mathrm{f}} = 0 \quad \text{..... (4.47)}$$

The fluidized particles and the fluid are assumed to have the same velocity, thus ignoring any slip between these species.

Disregarding energy dissipation due to plastic deformation of the grains, but considering energy dissipation due to elastic damage, the constitutive relations between the effective stresses acting on the grains of the porous rock and strains are written in compact form as

$$\sigma_{ij} = 2G(1-D)^2\varepsilon_{ij} + \frac{E_0(1-D)^2}{(1-\nu)(1-2\nu)}\varepsilon_{kk}\delta_{ij} - bp\delta_{ij} \quad \text{..... (4.48)}$$

Damage due to dilatancy effect is usually smaller compared to massive damage caused by erosion of the grains of the matrix; thus it may be disregarded. But in a case where the dilatancy effect is highly significant, the superposition of the damage variables is proposed.

Based on the significant erosion of the matrix, the permeability of the matrix will not be isotropic after damage. In this framework, the simple relation between permeability and porosity, Carman-Kozeny relation, is used

$$k = k_0\frac{\Phi^3}{(1-\Phi)^2} \quad \text{..... (4.49)}$$

Furthermore, as the erosion front moves into the formation, the cohesive strength of the rock reduces with time. And to account for the change in the cohesion of the rock, the

cohesive strength of the rock is treated as a stiffness modulus between contacting grains; hence the cohesive strength of the rock reduces at the same rate as the Young's modulus.

From equation (4.33), the mass generation rate per unit density of the fluidized-solid particles is

$$\frac{\dot{m}}{\rho_S} = \frac{\partial}{\partial \mathrm{t}}(\Phi) = \frac{1}{\mathbf{S.I}} \begin{Bmatrix} \nabla . \lfloor (p - p_c) \delta C \, \mathbf{v}_S \rfloor \det(\mathbf{F}) - \mathbf{S.I} \, \delta\Phi \, \mathrm{tr}(\mathbf{L}) \\ - \delta C \dfrac{\mathbf{b}}{\rho_{\mathrm{S}}} . \mathbf{v}_S \det(\mathbf{F}) - \delta\Phi \dfrac{\partial}{\partial \mathrm{t}} \left(\dfrac{\mathbf{S.I}}{\det(\mathbf{F})} \right) \det(\mathbf{F}) \end{Bmatrix} \quad \text{..... (4.50)}$$

By combining equations (4.45) to (450) and including the fluid velocity relation given in equation (4.37), gives the governing equations for the three-phase erosion kinetic problem. Depending on the state of the formation and the reservoir response, different boundary conditions exist, but for blowout during the drilling phase, the reservoir is assumed to be infinite acting. Typical boundary and initial conditions during the uncontrolled production of hydrocarbons are as follows:

Inner Boundary Conditions for Erosion around a Borehole:

$$\left[\rho_S c + \rho_{\mathrm{f}} (1-c)\right] v_{\mathrm{fxo}} - \rho_{w,zo} v_{\mathrm{zo}} = \frac{1}{L} \int_0^L \frac{\partial}{\partial t} \{ \rho_W(z) V_W \} dz \quad \text{..... (4.51)}$$

$$p(x = r_W, t) = p_{bW} \quad \text{..... (4.52)}$$

$$C\Phi(x = r_W, t) = \theta_0 \quad \text{..... (4.53)}$$

$\rho_{w,zo}$ is the density of the fluid at the wellbore surface and L is the length of the borehole. Depending on the pressure condition at the surface, the density value can be a mixture of solids, gas, and liquid phases, since gas will come out of solution if the pressure is below the bubble-point of the oil. Or if the reservoir fluid is gas, then the density of the gas

changes with pressure and temperature (this is significant for deepwater operations). v_{zo} is the velocity at which the wellbore slurry exits; the assumption here is that both solid and fluid phases have the same velocity.

$$v_{f,xo} = \frac{1+\sqrt{1-4\left(-\frac{k}{\eta\bar{\rho}}\frac{\Delta p}{r_t}+\frac{k}{\eta}g\right)\frac{k}{\eta}\beta_F}}{\frac{2k}{\eta}\beta_F} \quad \text{..... (4.54)}$$

is the sand-face velocity of the fluid. Assuming the pressure wave front is uniform, and noting that its speed will be greater than the velocity of the erosion front (Fig. 4.2), the fluid particles at the front move at Darcy's velocity. Furthermore, since the pressure gradient in the epsilon neighborhood of the front will not be significant, erosion cannot occur.

Outer Boundary Conditions for Erosion around a Borehole:

$$C(x_{\mathrm{Re}},t)=0 \quad \text{..... (4.55)}$$

$$p(x_{\mathrm{Re}},t)=p_i \quad \text{..... (4.56)}$$

$$\Phi(x_{\mathrm{Re}},t)=\Phi_0 \quad \text{..... (4.57)}$$

Initial Conditions for Fluid Flow in a Producing Reservoir:

$$C(x,0)=0 \quad \text{..... (4.58)}$$

$$p(x,0)=p_i \quad \text{..... (4.59)}$$

$$\Phi(x_{\mathrm{Re}},t)=\Phi_0 \quad \text{..... (4.60)}$$

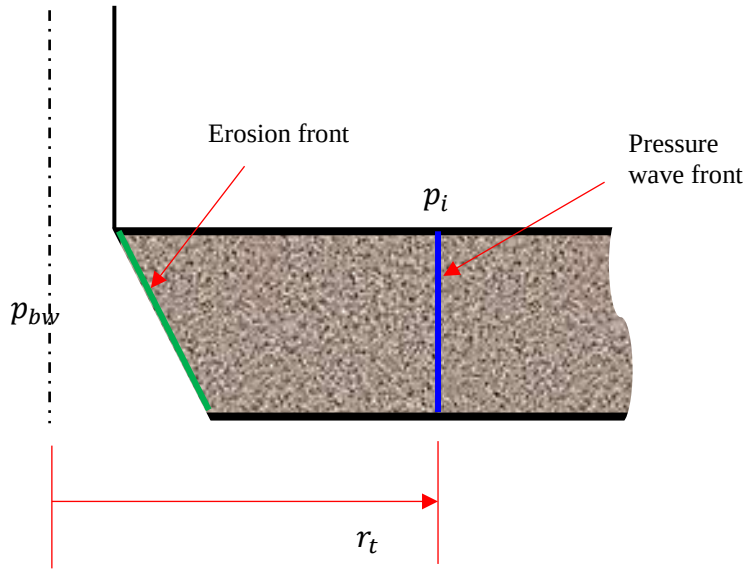

Fig 4.2. Pressure wave and erosion fronts during radial erosion.

4.6 Critical Observations from the Proposed Erosion Constitutive Relation

From the proposed erosion constitutive relation, the following points, which agree with experimental findings, can be deduced by inspection:

a. Prior to significant erosion of the matrix, the sand-rate increases with the same profile as the fluid velocity; this is the transient state of the sand production process.

b. As sand production increases, the formation will respond by compacting.

c. The compaction of the eroding formation reduces the erosion rate, det (**F**) <1, and also the rate of compaction further influences the reduction in erosion rate.

d. For constant fluid flux (which is not realistic in long eroding-reservoir in the field), the mass rate has a relatively linear relationship with the fluid-flux. This linear relationship is projected to occur when the erosion front is thin (a sharp interface).
e. The increment in sand rate with applied stress is assumed to be link to significant second-order effects, which reduce the critical hydraulic gradient and increase permeability to flow. Consequently, increasing the resultant hydraulic gradient (this is a non-linear coupling as observed in experiments by Papamichos, 2010).

4.7 Numerical Application

Axial erosion around a wellbore section is simulated using the derived erosion equations above. In this example, the matrix is assumed to be subjected to an isochoric deformation and that no cohesion exists among the grains. The example couples fluid flow in an open channel (wellbore) and a porous medium (Fig. 4.3). The fluid flow in the channel is described by Navier-Stokes equation and a Forchheimer-corrected version of the Brinkman-correction of the Darcy's equation is used in the porous medium. The viscous effects around the boundary of the open-channel and the porous medium cause some disturbances around the borehole, which can initiate erosion around the regions near the borehole wall.

Axial erosion often occurs in perforation channels, which are enhanced-conduits for the production of hydrocarbons into the wellbore. Perforation erosion is a big problem in the petroleum industry and it has attracted the attention of many researchers. But most of their solutions are based on empirical models, which are limited in their applications. In the same vein, axial erosion also occurs along the wellbore wall during uncontrolled

(well blowouts) or controlled production of oil and gas. This example is expected to shed more light into the mechanisms for axial erosion.

Model Parameter	Value/ Expression	Description
Φ_0	0.4	Initial porosity
k_0	2.9608E-13m^2	Initial permeability
ρ_s	2650 kg/m^3	Density of solid particles
ρ_w	980 kg/m^3	Density of pristine fluid
C_0	0 mol./m^3	Initial concentration of particles in the void space
C_s	1 mol./m^3	Normalized concentration of the fluidized particles
μ_f	0.001 Pa.s	Viscosity of pristine fluid
D_L	3.56 E-6 m^2/s	Molecular diffusion
S_V	5.5158E7 Pa	Vertical stress
S_H	4.8263 E7 Pa	Maximum horizontal stress
S_h	4.1369 E7 Pa	Minimum horizontal stress
C_F	$\frac{1.75}{\sqrt{150\Phi^3}}$	Friction coefficient

Table 4.1. Model parameters for axial erosion simulation.

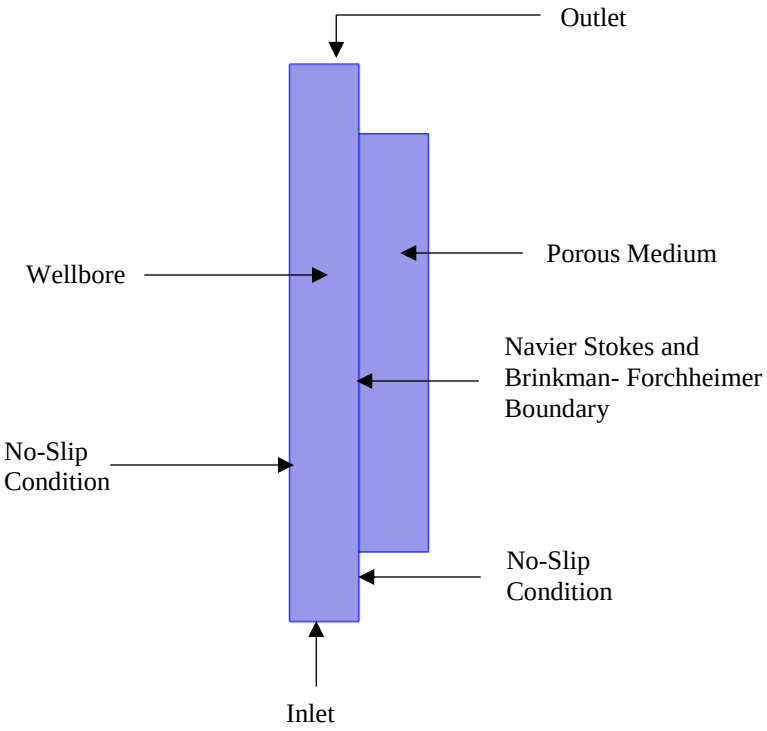

Fig. 4.3. Model domain and boundary conditions notation.

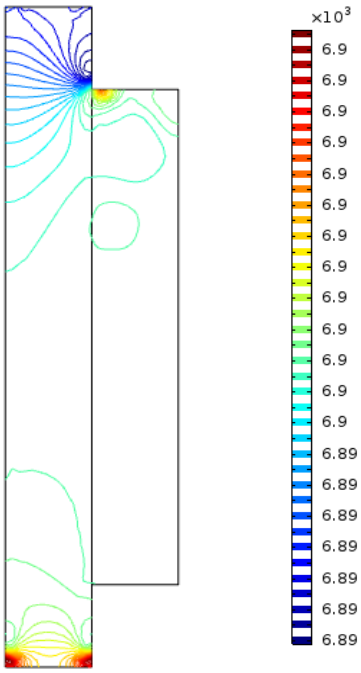

Fig.4.4. Pressure (in KPa) distribution in the open-channel and porous medium at the onset of erosion.

The computational domain is a small section of the wellbore, and the other porous medium at the left hand side of the wellbore subdomain has been omitted in this simulation, since the objective of the simulation is to investigate the erosion potential around the wellbore. In this example, the pressure difference across the section is 6.89MPa (1000 psi) and the inlet velocity is 200 cm/s; the other model parameters are listed in Table 4.1.

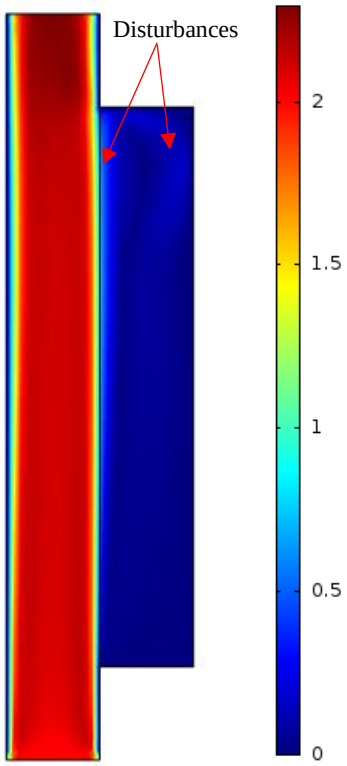

Fig.4.5. Velocity (in m/s) distribution in the open-channel and porous medium at the onset of erosion.

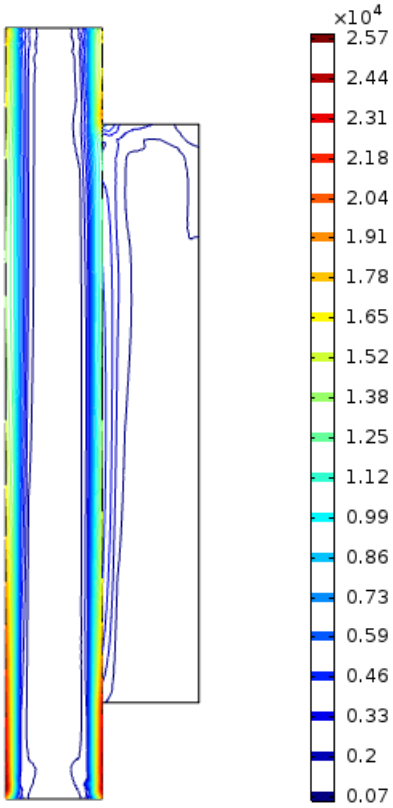

Fig.4.6. Shear rate (in 1/s) distribution in the open-channel and porous medium at the onset of erosion.

Fig. 4.5 shows the disturbances at the boundary of the open channel and the porous medium. This observation agrees with the proposition of Vardoulakis et al. (2000); they argued that near the boundary of the open channel and the porous medium, Darcy's law will not be valid. Furthermore, Fig. 4.6 shows the shear rate distribution at the onset of erosion. Farther into the porous medium the shearing rate reduces as a result of low disturbance; the shear rate profile is continuous across the boundary.

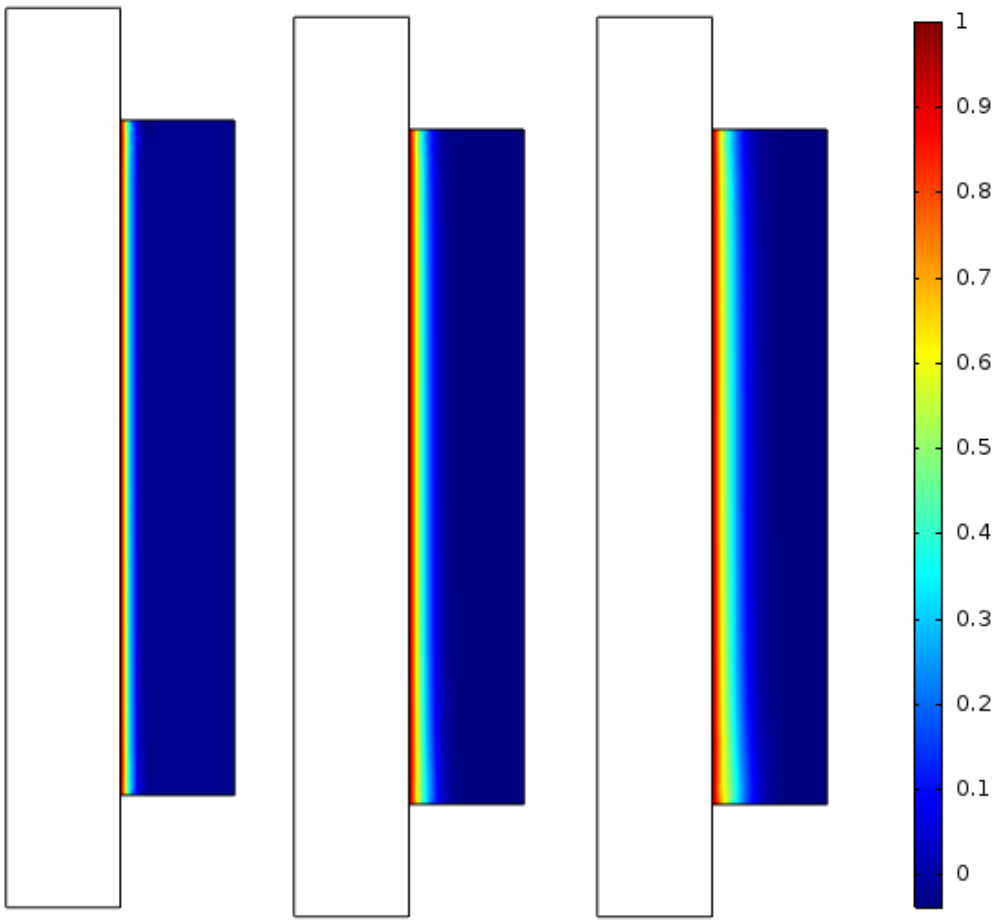

Fig.4.7. Distribution of fluidized particles concentration (in mol. /m^3) in the porous medium during the erosion process at times (a) 3s, (b) 10s, and (c) 20s.

The erosion front in this case is uniform because the pressure and velocity distributions at the front are almost uniform (Figs. 4.7 and 4.8). In a case where the pressure and velocity distributions are not uniform, also the erosion front will not be uniform.

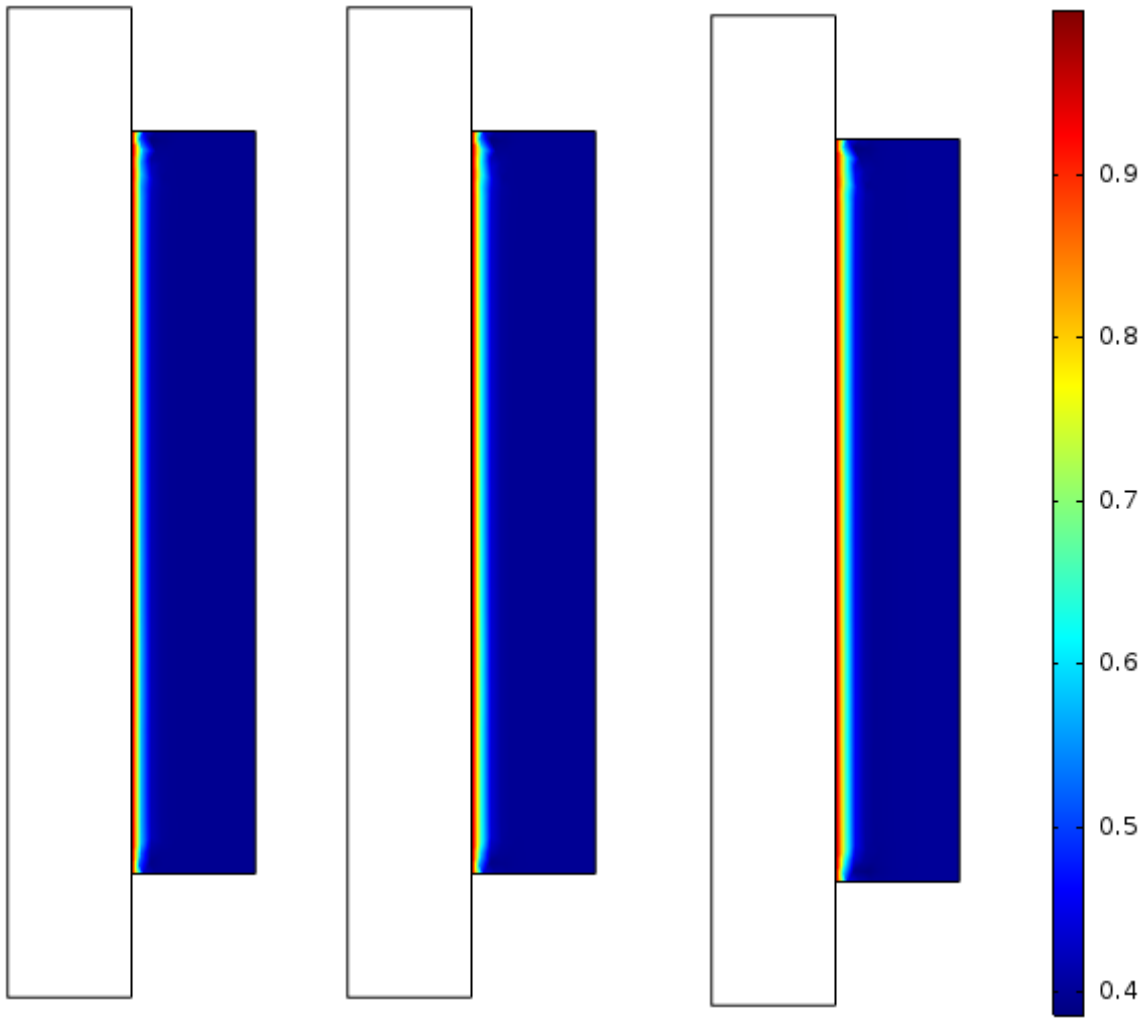

Fig.4.8. porosity evolution in the porous medium during the erosion process at times (a) 3s, (b) 10s, and (c) 20s.

4.8 Summary

An energy-consistent erosion constitutive relation for deformable porous medium is proposed. The model reveals the weakness of the well-known phenomenological model when the pressure gradient in the producing formation is not steep towards the wellbore. For axial erosion around the wellbore, the momentum transport by viscous effects on the porous layers can unseat the grains of the matrix. While a radial erosion in the producing formation occurs, when the sum of both the viscous stress and pressure difference across the grains (seepage forces) exceeds the critical hydraulic gradient. For competent formation, higher hydraulic gradient will be required to break the bonds between the particles; this is unlikely in most cases. It thus suggests that erosion will occur in weakly-cemented and unconsolidated formations. By inspection of the derived conceptual model, the following observations are restated:

1. Prior to significant erosion of the matrix, the sand-rate increases with the same profile as the fluid velocity; this is the transient state of the sand production process.
2. As sand production increases, the formation will respond by compacting.
3. The compaction of the eroding formation reduces the erosion rate, det ($\mathbf{F}$) <1, and also the rate of compaction further influences the reduction in erosion rate.
4. For constant fluid flux (which is not realistic in long eroding-reservoir in the field), the mass rate has a relatively linear relationship with the fluid-flux. This linear relationship is projected to occur when the erosion front is thin (a sharp interface).

5. The increment in sand rate with applied stress is assumed to be link to significant second-order effects, which reduce the critical hydraulic gradient and increase permeability to flow. Consequently, increasing the resultant hydraulic gradient (this is a non-linear coupling as observed in experiments by Papamichos, 2010).

5. A THERMODYNAMICALLY CONSISTENT MULTIPHASE-FIELD MODEL FOR NON-ISOTHERMAL TRANSPORT OF GAS-LIQUID-SOLID PARTICLE FLOW: THEORETICAL DEVELOPMENT

5.1 Scope

To rigorously predict the potential for self-killing due to sedimentation in the wellbore, the study on the transport of cavings or produced sand in the wellbore is highly essential. The hydrodynamic interactions between the solid and fluid particles play a big role in understanding the transport process. In addition, the constitutive relation of the fluid mixture may not be Newtonian as different “fluid species” mix up in the wellbore; a three-phase fluid flow problem can ensue when the reservoir fluid is oil or both gas and water are produced. In this study, a thermodynamically consistent phase-field model based on the notion of internal configurational forces are derived to characterize the n-phase mixture of gas, liquid, solid, water, and any other component. The model is based on averaged Navier-Stokes and Cahn-Hilliard system of equations. A free energy is introduced to account for the surface tension among the different components of the mixture and their contact lines.

5.2 Background on Multiphase Fluid Modeling

The modeling of multiphase-fluid, especially fluid-particle systems, is very complicated, as the hydrodynamic interactions among the different species in the mixture have significant impact on the transport process. One of the questions that arises when investigating fluid-particle flow process is understanding what governs the non-uniform

distribution of the dispersed phase concentration. Prior to the advent of supercomputing machines, these studies were mainly experimental, and some of the developed empirical relations are still in use today (Othmer 1956, Leva 1959, Zenz and Othmer 1960). Davidson and Harrison (1963) and Kunii and Levenspiel (1969) integrated the mechanisms responsible for the observed heterogeneities into design calculations, which dominated multiphase-fluid studies in the subsequent years. Their attempts sparked application of fundamental principles in solving complex flow problems. Pritchett et al. (1978), and Gidaspow and Ettenhadieh (1983) pioneered the application of continuity and momentum balance equations for two-phase flow problems. Their works formed the foundation on which many computational fluid dynamics (CFD) simulations are based.

The use of CFD simulations in the investigation of complex multiphase-fluid systems is rapidly increasing today, though some of the empirical relations still remain. CFD-based models are built on three levels of details. The most fundamental approach is the use of Newtonian equations for translation and rotation of each solid particles, while ensuring that Navier-Stokes and continuity equations are satisfied at each point in the fluid phase. No slip condition is placed between the solid and fluid phases and between the fluid and the boundaries of the domain.

The second level of description is the use of discrete particle modeling. This approach entails the replacement of the fluid velocity at each point by its average over a representative volume element. The force exerted on each particle by the fluid is related to the particle's velocity relative to the locally averaged fluid velocity, and the local concentration of the particles; many empirical correlations have been developed in this

regard. Furthermore, Newtonian equations of motion are then used to solve the kinetics and kinematics of each solid particles, taking into account the direct collisions among the particles. Some of the notable works on the use of discrete particle modeling for particle-fluid system include Tsuji et al. (1993), Hoomans et al. (1996), Cundall and Strack (1979); Cundall and Strack developed the soft-particle modeling approach. In the soft particle modeling approach, particles can deform and the deformations are then used to determine the interacting forces between them. The non-linear relationship between force and displacement was developed by Hertz (1882) and it was improved upon by Mindlin and Deresiewicz (1953) and Di Renzo and Di Maio (2004); this model is rarely used for modeling flow of particulates due to its complication and high computing cost. Nevertheless, simpler versions of the nonlinear model have been developed by Walton and Braun (1986) and Walton (1993); Walton used semi-latched spring force-displacement model in the normal direction and an approximate form of the Mndlin and Deresiewicz theory in the tangential direction, for constant normal force. Other authors who have contributed to the development of particle-particle interactions, using simplified models of Hertz-Mindlin and Deresiewicz are Thornton and Yin (1991), Langston et al. (1994), Thornton (1997), and Vu-Quoc and Zhang (1999a,b); for further information, the paper by Zhu (2007) gives detailed overview of the discrete particle modeling approach.

The most common method for modeling flow of dense particle-fluid flow is based on Eulerian descriptions of both solid and fluid phases of the continuum. The velocities of the fluid and solid particles are averaged over the local spatial domain. The velocity fields of the phases are then defined at all points in space; hence, resulting into two equations

for the two species. This approach is less computationally demanding compared to the first two approaches mentioned earlier. Nevertheless, unlike the discrete particle models, the Euler-Euler method suffers the disadvantage that closures must be formulated for certain terms in the governing momentum equation in the particle phase; these terms are generated from the process of averaging the momentum equation and are related to the velocity fields and particle concentration. However, the discrete particle method does not provide means of properly representing these averaged terms.

Significant progress has been made in the modeling of multiphase flow. Anderson and Jackson (1967) derived the continuum equations of motion for the gas-particle flow. Garg et al. (1975 and 1978) performed some numerical experiments on the derived equations to obtain the bubble behavior in a fluidized bed. Balzer and Simonim (1993), Balzer et al. (1996), Boemer et al. (1997), Ding and Gidaspow (1990), Ding and Lyczkowski (1992), Enwald and Peirano (1995), Gidaspow et al. (1983), Gidaspow (1994), Kuipers (1990), Lavieville et al. (1995), Lun and Savage (1986), Nott (1991), Sinclair and Jackson (1989), Syamlal (1987), Ljus (2000), and Wachem et al. (2001) improved the constitutive models and performed several simulations on gas-solid flows. Similarly, Ishii (1975) derived the multiphase fluid-fluid governing equations using different assumptions from Anderson and Jackon's; its model is more accurate for flow of immiscible fluids.

Another major setback for the common two-fluid model is that the models fail when the mixture behavior significantly deviates from being Newtonian. For liquid-liquid, gas-liquid, solid-gas, or liquid-solid mixtures, the two-fluid model assumes a Newtonian

behavior of each phase, and based on many experimental findings, this approximation in the constitutive behavior of the mixture works for certain range of composition. When the volume fraction of the solid particles, for example in a fluid-solid mixture, is very high, the mixture cannot be represented as a Newtonian fluid. To overcome this limitations of the Euler-Euler method, advanced modeling methods are being proposed by many authors.

5.2.1 Advanced Modeling Methods for Multicomponent Fluid Flows

Most studies on three-phase systems do not consider hydrodynamic interactions among the species of the mixture (Barret and Blowey 1996, 1999a, 1999b, 2001, Blowey et al. 1996, Copetti 2000, Eyre 1993, Garcke et al. 2000). Also, the studies on the two-fluid models are inaccurate as the mixture significantly deviates from Newtonian fluid.

Projection method was used by Smith et al. (2002) to understand the motion of triple junction in level-set framework. Kan et al. (1998) used immersed boundary method (Peskin 1977) to simulate compound drop of three immiscible fluids. Kim et al. (1997), Milliken and Leal (1994), and Stone and Leal (1990) used boundary integral methods to study effect of surfactants drop dynamics, while Eggleton et al. (2001) studied the effect of surfactant on tip-streaming. Drumright and Renardy (2004), James and Lowengrub (2004), and Renardy et al. (2002) studied the effect of insoluble surfactants on drop deformations in two and three dimensions using volume of fluid methods. Jan and Tryggvason (1991) performed an investigation on the effect of surfactants on the dynamics of rising bubbles using immersed boundary/front-tracking algorithm. Ceniceros (2003) used hybrid level-set/front-tracking algorithm to study the effect of surfactants on capillary waves. Furthermore, Johnson and Borhan (2000) studied the effect of surfactants

on the evolution of the shape of non-spherical drop with a translational motion in a slow moving fluid, using a combination of boundary integral method and finite difference scheme.

Kim et al. (2004) simulated three-phase systems and suppressed the hydrodynamic interactions, while Kim and Lowengrub (2005) included the influence of the hydrodynamic interactions using thermodynamically consistent phase-field model.

In this work, thermodynamically consistent phase-field model is used to investigate the flow of multicomponent phases of a mixture, but with the addition of internal workings in the bulk of the different phases and interfaces due to the internal configurational forces. Lowengrub and Truskinovsky (1998) introduced a generalized force component into the energy equation, which they failed to ascribe its source. This study has been able to identify this generalized force as the micro-force responsible for the volume expansion of each phase. The derived system of equations couples averaged linear momentum balance to the Cahn-Hilliard type equations for the phase variables; mass ratios of the fluid components are the components of the vector order-parameter. The advantages of this approach over previous attempts include: (1) there is no need to perform any correction steps to multiple junctions, (2) incorporating other physical properties like miscible and immiscible fluid components is easy, and (3) a balance law for the micro-forces system is presented.

5.2.2 Phase-Field Model

The use of diffuse interface deviates from the perspective of Gibbs who assumed sharp interface. Many authors have used the concept of diffuse interface to model the

continuity of physical quantities across this boundary (Falk 1980, 1983, 1990, Pengtao et al. 2013, Igor et al. 2010, Kim 2012, Anderson et al. 1998, Jacqmin 1999, Truskinovsky 1993, Zhang and Wang 2016, Fried and Gurtin 1993, and Antanovskii 1994); the order parameter is coupled with other field variables to ensure their continuity across the interface. In this study, the order parameter is the mass concentrations of the species in the mixture. In essence this variable identifies the state of each phase in the continuum (mixture). The internal micro-force is the conjugate to the rate at which this variable changes and it expends power during the creation of a surface, for example, the evolution or dissolution of gas.

5.2.3 The Notion of Configurational Forces

The notion of internal configurational forces was introduced into continuum physics by the works of Burton (1892), Eshelby (1951, 1970, and 1975), Herring (1951), Peach and Koehler (1950); their proposition was that additional force system is needed to adequately describe phenomena that are associated with the material body, especially phenomena that the standard Newtonian force system cannot describe. For example, the creation of new surfaces in a material body cannot be described by Newtonian force system. Newtonian force system is responsible for deformation or stretching of a material body.

Gurtin (2000) and Gurtin and Struthers (1990) further expatiated on this notion. Their argument was that the balance of micro-forces should be a basic concept in continuum physics. These forces are linked to the integrity of the material structure, and do perform work during transport of material particles and the evolution of material

structures. Configurational stress is different from residual stress, which is a stress in the reference configuration of an undeformed material body; it is referenced to the standard Newtonian force system. The internal configurational force system becomes indeterminate when there is no change in the material structure, but becomes dominant as changes (not due to deformation or straining) occur in the material. This notion will be added to the total energy system of the mixture in this study.

Consider a migrating control volume, Ω, containing a part, *P*, that is intersecting an interface, $\wp$, which separates two phases in the region. The total working of the migrating control volume consists of:

1. The contributions associated with the workings within the bulk of the material body. These workings are subdivided into two parts, which are

a. Working due to standard Newtonian forces

$$\int_{\partial P} \mathbf{Pn}.\frac{\partial \mathbf{y}}{\partial t}\, da + \int_{P} \mathbf{b}.\frac{\partial \mathbf{y}}{\partial t}\, dV \quad \text{..... (5.1)}$$

b. Working due to internal configurational forces in the bulk of the material of the corresponding phase

$$\int_{\partial P} \mathbf{Cn}.\mathbf{q}\, da + \int_{P} (\mathbf{g}+\mathbf{d}).\mathbf{q}\, dV \quad \text{..... (5.2)}$$

This net configurational working tends to increase the volume of part *P* through addition of materials at its boundary.

2. The contributions associated with the moving interface.

$$\int_{\wp \cap P} \left\{ \left(\mathbf{e}^{\wp} + \mathbf{g}^{\wp} \right) . \mathbf{v} + \mathbf{b}^{\wp} . \mathbf{y}^{*} \right\} da + \int_{\partial \wp} \mathbf{Q} \mathbf{n} . \mathbf{w} \; ds \quad \text{..... (5.3)}$$

P is the first Piola- Kirchhoff stress. $\mathbf{q}$ is the conjugate velocity following the boundary surface to part *P,* and $\dot{\mathbf{y}}$ is the corresponding motion velocity following the boundary surface of part *P.* The force responsible for the migration of the interface is $\mathbf{e}^{\wp}$ and the corresponding work-conjugate velocity is **v. y*** is the corresponding motion velocity following the interface. $\mathbf{g}^{\wp}$ is the internal force that pins the material points at the interface. **Q** is the interfacial stress, which can be further subdivided into surface tension and surface shear. $\mathbf{b}^{\wp}$ is characterized as the interface inertia force, and it is responsible for temporal changes in momentum of the interface.

5.3 Model Development

Considering N_f number of species in a mixture, the mass concentration of each species at any point in time is

$$c_k = \frac{M_k}{M} \quad \text{..... (5.4)}$$

Where, $M = \sum_{k=1}^{N_f} M_k$ is the total mass of the mixture, and

$$\sum_{k=1}^{N_f} c_k = 1 \quad \text{..... (5.5)}$$

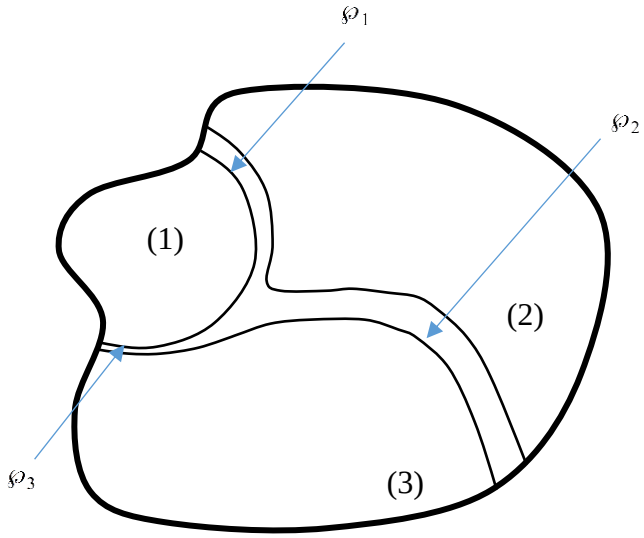

Fig.5.1. Representative volume element of the mixture of three species having different interface widths.

Fig. 5.1 shows the representative volume element of three components of a mixture. The widths of the interfaces differ because of the difference in the strengths of the internal configurational forces of each species and the interfaces. For rigorous modeling of the behavior of the mixture, the constitutive behavior of the interfaces should not be relegated to the strength of the surface tension only. But for simplicity, I will account for the influence of surface tension on the constitutive behavior of the mixture by defining a free energy that will include the gradient energies.

Let the part in each of the phases, which is far from the interfaces, move at a velocity $\dot{\boldsymbol{y}}_k$ and has a density

$$\rho_k = \frac{M_k}{V_k} \quad \text{.....(5.6)}$$

where V_k is the volume of species *k* in the mixture. The volume fraction of each species is defined as

$$\phi_k = \frac{V_k}{V} \quad \text{.....(5.7)}$$

and the mixture density, $\bar{\rho} = \sum_{k=1}^{N_f} \rho_k \phi_k$, is also related to its components' densities via

$$\bar{\rho}\, c_k = \rho_k\, \phi_k \quad \text{.....(5.8)}$$

or

$$\frac{1}{\bar{\rho}} = \sum_{k=1}^{N_f} \frac{c_k}{\rho_k} \quad \text{.....(5.9)}$$

It should be noted that one of the components of the proposed mixture is gas, whose density is dependent on pressure. The density of the gas phase is

$$\rho_k = \frac{pM_k}{Z_k R_k T} \quad \text{.....(5.10)}$$

Lowengrub and Truskinovsky (1998) termed the mixture of incompressible fluid components as quasi-incompressible because the mixture density is not constant, but depends on the mass fractions of the components. In this work, the presence of gas makes the mixture compressible; hence, degeneracy will not exist in the free energy equation.

The mass-averaged velocity field of the mixture is

$$\dot{\mathbf{y}} = \frac{1}{\bar{\rho}} \sum_{k=1}^{N_f} \rho_k \phi_k \dot{\mathbf{y}}_k = \sum_{k=1}^{N_f} c_k \dot{\mathbf{y}}_k \quad \text{..... (5.11)}$$

5.3.1 Mass Balance of Species

By local spatial averaging, the mass balance for each species in arbitrary region *P* is

$$\frac{\partial}{\partial t}\left(\rho_k \phi_k\right) + \nabla \cdot \left(\rho_k \phi_k \dot{\mathbf{y}}_k \right) = \dot{m}_k \quad \text{..... (5.12)}$$

$\dot{m}_k$ is the net rate of mass supply of each species in an arbitrary sub region *P*. For the foregoing problem, the net rate of mass supply of the solid particles is zero, while the magnitude of the supply of gas is same as the magnitude of the mass of liquid depleted in the liquid matrix. As a result, equation (5.13) holds for the mixture mass balance. Depending on the mechanism responsible for sand production, the mass rate for the solid particles may be continuous or intermittent. At the early stage of the erosion process, the rate of sand production is continuous until severe compaction of the reservoir impedes the transport process. In case of wellbore breakout, the influx time of the cavings into the wellbore may be very short. The mass rate of the solid particles is the rate at which the slender rock layers buckle; this rate may not be constant, as the tendency for the formation of the slender rock layers reduces as the failure process progresses. By summing Eq. 5.12 in *k*, the mass balance for the mixture is

$$\frac{\partial \bar{\rho}}{\partial t} + \nabla . \left(\bar{\rho}\, \dot{\mathbf{y}} \right) = \sum_{k=1}^{N_f} \dot{m}_k = 0 \quad \text{..... (5.13)}$$

It should be noted that the conservation of mass of each species states that

$$\frac{\partial \rho_k}{\partial t} + \nabla . \left(\rho_k \dot{\mathbf{y}}_k \right) = 0 \quad \text{..... (5.14)}$$

From equations (5.12) and (5.14), yields the mass concentration equation

$$\bar{\rho}\, \dot{c}_k = \nabla . \mathbf{J}_k + \dot{m}_k \quad \text{..... (5.15)}$$

where, $\mathbf{J}_k$ is the diffusion flux.

5.3.2 Balance of Linear Momentum

For each component, the balance of linear momentum is

$$\bar{\rho}\, c_k \frac{D^k}{Dt} \left(\ddot{\mathbf{y}}_k \right) = \nabla . \mathbf{T}_k + \bar{\rho}\, c_k \mathbf{g}_c + \pi_k \quad \text{..... (5.16)}$$

$\frac{D^k}{Dt}$ is the material derivative with respect to component velocity, $\mathbf{T}_k$ is the first Cauchy stress for each component, $\mathbf{g}_c$ is the gravity force and π_k is the sum of the forces due to the interactions among the phases. Noting that by disregarding the inter particle-particle interaction forces and summing over *k*, yields the condition necessary for the conservation of linear momentum for the mixture:

$$\sum_{k=1}^{N_f} \pi_k = 0 \quad \text{..... (5.17)}$$

Thus, the resulting linear momentum of the mixture is

$$\bar{\rho}\,\ddot{\mathbf{y}} = \nabla.\mathbf{T} + \bar{\rho}\,\mathbf{g}_c \quad \text{..... (5.18)}$$

where the stress tensor of the mixture is $\mathbf{T} = \sum_{k=1}^{N_f}\left(\mathbf{T}_k - \bar{\rho}\,c_k\mathbf{u}_k \otimes \mathbf{u}_k\right)$. One of the objectives of this study is to derive thermodynamically consistent constitutive relations for **T** and $\boldsymbol{J}_k$.

5.3.3 Energy Balance of the Mixture

The total global energy of the mixture is

$$\frac{d}{dt}\int_P\left(\bar{\rho}\,e + \frac{1}{2}\bar{\rho}\,|\mathbf{u}|^2\right)dV = \int_{\partial P}\left(\mathbf{T}\mathbf{n}.\mathbf{u} - \mathbf{q}_r.\mathbf{n}\right)da$$

$$+\int_P\left(\bar{\rho}\,\mathbf{g}_c.\mathbf{u} + \bar{\rho}\,r + \sum_{k=1}^{N_f}\mathbf{d}_k.\mathbf{q}_k\right)dV + \int_{\partial P}\sum_{k=1}^{N_f}\mathbf{C}_k\mathbf{n}.\mathbf{q}_k\,da + \int_P\sum_{k=1}^{N_f}\mathbf{g}_k.\mathbf{q}_k\,da \quad \text{..... (5.19)}$$

The conjugate velocity following part *P* is related to the order parameter via

$$\mathbf{q}_k.\mathbf{m} = \frac{\dot{c}_k}{|\nabla c_k|} \quad \text{..... (5.20)}$$

$\boldsymbol{m}$ is the unit vector normal to the state surface; and defining micro-stress $\boldsymbol{t}_k$ as

$$\mathbf{C}_k = \mathbf{m} \otimes |\nabla c_k|\,\mathbf{t}_k \quad \text{..... (5.21a)}$$

$$\left.\begin{aligned}\mathbf{f}_k &= \mathbf{d}_k\,\mathbf{m}\\ \mathbf{f}_k.\mathbf{m} &= |\nabla c_k|\,f_k\end{aligned}\right\} \quad \text{..... (5.21b)}$$

and substituting equations (5.20) and (5.21) into (5.19), the total global energy of the mixture becomes

$$\frac{d}{dt}\int_P\left(\bar{\rho}\,e+\frac{1}{2}\bar{\rho}\,|\mathbf{u}|^2\right)dV=\int_{\partial P}\left(\mathbf{T}\mathbf{n}.\mathbf{u}-\mathbf{q}_r.\mathbf{n}\right)da+\int_P\left(\bar{\rho}\,\mathbf{g}_c.\mathbf{u}+\bar{\rho}\,r\right)dV$$

$$+\int_{\partial P}\sum_{k=1}^{N_f}\mathbf{t}_k.\mathbf{n}\,\dot{c}_k\,da+\int_P\sum_{k=1}^{N_f}f_k\dot{c}_k\,da \quad \text{..... (5.22)}$$

Noting that $\dot{\boldsymbol{y}}=\boldsymbol{u}$ is the velocity vector. e is the internal energy of the system, r is the density of the heat sources that keeps the temperature of the mixture constant, and f_k is the external (micro) body force to the part P. The internal (micro) body force does no work, since it is internal to part P. The workings at the interface are not included in the energy balance equation above, but by defining a Cahn-Hilliard type free energy equation which includes the surface tension, the influence of the interfacial stress can be incorporated into the constitutive behavior of the mixture.

By using divergence theorem in Eq. 5.22, and applying the balance of mechanical power and mass balance of the mixture, the energy balance equation in local form yields

$$\bar{\rho}\,\dot{e}=\mathbf{T}.\mathbf{D}-\nabla.\mathbf{q}_r+\bar{\rho}\,r+\sum_{k=1}^{N_f}\nabla.\left(\mathbf{t}_k\dot{c}_k\right)+\sum_{k=1}^{N_f}f_k\dot{c}_k \quad \text{..... (5.23)}$$

5.3.4 The Second Postulate of Thermodynamics; Clausius-Duhem Inequality

All admissible thermodynamic process must not violate the conventional entropy inequality, which states that the rate of increase of entropy in a sub-region, P, in the material should not be less than the sum of entropy generation within the sub-region and influx of entropy across the boundary of P.

The diffusion of one phase into another sub-region causes some dissipation in the total energy of the system, as power is expended; hence, the diffusion of the evolved gas

in the liquid matrix to the gas matrix is a dissipative process and the energy expended needs to be accounted for in the foregoing problem. The conventional power balance does not take into account this additional energy expended, but by following the micro-entropy imbalance relation postulated by Podio-Guidugli (2006), the entropy inequality becomes

$$\frac{d}{dt}\int_P \bar{\rho}\,\eta\,dV \geq -\int_{\partial P}\frac{\mathbf{q}\,r}{T}.\mathbf{n}\,da + \int_P \bar{\rho}\,\frac{r}{T}da - \int_{\partial P}\sum_{k=1}^{N_f}\mu_k\,\mathbf{J}_k.\mathbf{n}\,da + \int_P \sum_{k=1}^{N_f}\mu_k\,\dot{m}_k dV \quad \text{..... (5.24)}$$

By combining the first postulate of thermodynamics (Eq. 5.23) with the second (Eq. 5.24) the Clausius-Duhem inequality in local form becomes

$$\begin{aligned} &-\bar{\rho}\,\dot{\psi} - \bar{\rho}\,\dot{T}\eta - \mathbf{T}.\mathbf{D} - \nabla T.\frac{\mathbf{q}_r}{T} + \sum_{k=1}^{N_f}\nabla.\left(\mathbf{t}_k\dot{c}_k\right) + \sum_{k=1}^{N_f} f_k\,\dot{c}_k \\ &-\sum_{k=1}^{N_f}\nabla.\left(\mu_k\,\mathbf{J}_k\right) + \sum_{k=1}^{N_f}\mu_k\,\dot{m}_k \geq 0 \end{aligned} \quad \text{..... (5.25)}$$

From the balance of the micro-forces (in local form) in the bulk of part *P* (Eq. 5.2), a sub-region far away from the interfaces,

$$\nabla.\mathbf{t}_k + g_k + f_k = 0 \quad \text{..... (5.26)}$$

the Clausius-Duhem inequality yields

$$-\bar{\rho}\,\dot{\psi} - \bar{\rho}\,\dot{T}\eta - \mathbf{T}.\mathbf{D} - \nabla T.\frac{\mathbf{q}_r}{T} + \sum_{k=1}^{N_f}\mathbf{t}_k.\nabla\dot{c}_k - \sum_{k=1}^{N_f} g_k\,\dot{c}_k - \sum_{k=1}^{N_f}\mathbf{J}_k.\nabla\mu_k + \sum_{k=1}^{N_f}\mu_k\bar{\rho}\,\dot{c}_k \geq 0 \quad \text{.. (5.27)}$$

It should be noted that $\boldsymbol{q}_r$ is the heat flux, T is the absolute temperature of the mixture, ψ is the Helmholtz free energy, and η is the entropy of the system. For invariance under change in observer, the conjugate pairs of stress and rate of deformation for the stress

power are used in the development of the constitutive relation of the mixture. μ_k is the chemical potential of each species, which characterizes the diffusion process.

5.3.5 Constitutive Relations

Based on the coupled processes in the foregoing problem, the independent variables in the constitutive model are proposed to be $(\mathbf{D}, T, \nabla T, c_k, \nabla c_k, \dot{c}_k, \mu_k, \nabla \mu_k)$. **D** is the symmetric part of the velocity gradient. The gradients of mass concentration, temperature, and chemical potential are included to account for non-local behavior in the material-makeup of the mixture. The time rate of change of the mass concentration of the species is introduced to account for the intrinsic rate dependency in material structure as a result of the motion of the interfaces.

Hence, the following response functions are proposed to define the constitutive behavior of the mixture at each point in time.

$$\psi = \hat{\psi}\left(\mathbf{D}, T, \nabla T, c_k, \nabla c_k, \dot{c}_k, \mu_k, \nabla \mu_k\right) \quad (5.28)$$

$$\mathbf{J}_k = \hat{\mathbf{J}}_k\left(\mathbf{D}, T, \nabla T, c_k, \nabla c_k, \dot{c}_k, \mu_k, \nabla \mu_k\right) \quad (5.29)$$

$$\mathbf{t}_k = \hat{\mathbf{t}}_k\left(\mathbf{D}, T, \nabla T, c_k, \nabla c_k, \dot{c}_k, \mu_k, \nabla \mu_k\right) \quad (5.30)$$

$$\eta = \hat{\eta}\left(\mathbf{D}, T, \nabla T, c_k, \nabla c_k, \dot{c}_k, \mu_k, \nabla \mu_k\right) \quad (5.31)$$

$$\mathbf{q}_\mathrm{r} = \hat{\mathbf{q}}_\mathrm{r}\left(\mathbf{D}, T, \nabla T, c_k, \nabla c_k, \dot{c}_k, \mu_k, \nabla \mu_k\right) \quad (5.32)$$

$$\mathbf{T} = \hat{\mathbf{T}}\left(\mathbf{D}, T, \nabla T, c_k, \nabla c_k, \dot{c}_k, \mu_k, \nabla \mu_k\right) + \mathbf{A}\left(T, \nabla T, c_k, \nabla c_k, \dot{c}_k, \mu_k, \nabla \mu_k\right)\left[\mathbf{L}\right] \quad (5.33)$$

These response functions are defined to obey Truesdell (Truesdell and Noll 1992) principle of equipresence, which states that a quantity present as an independent variable

in one constitutive equation should be present in all, except if its presence violates some laws of physics or the rule of invariance. The response function **A** in equation (5.33) is a linear transformation over the nine-dimensional space of tensors, and ***L*** is the velocity gradient; ***L = D + W.*** **A** is added to the stress response function to include the effect of viscosity. The response function may depend nonlinearly on the velocity gradient, which will necessitate dependency on acceleration gradients. Since no allowance for acceleration gradient is desired, a linear dependency on the velocity gradient is preferred. For material objectivity

$$\mathbf{A}\left(T,\nabla T,c_k,\nabla c_k,\dot{c}_k,\mu_k,\nabla\mu_k\right)[\mathbf{L}]=\mathbf{A}\left(T,\nabla T,c_k,\nabla c_k,\dot{c}_k,\mu_k,\nabla\mu_k\right)[\mathbf{D}] \quad \text{..... (5.34)}$$

and

$$\mathbf{Q}\,\mathbf{A}[\mathbf{D}]\mathbf{Q}^{\mathrm{T}}=\mathbf{A}\left[\mathbf{Q}\,\mathbf{D}\,\mathbf{Q}^{\mathrm{T}}\right] \quad \text{..... (5.35)}$$

Using Chain rule, the time rate of change of the Helmholtz free energy can be expressed as

$$\dot{\psi}=\frac{\partial\hat{\psi}}{\partial\mathbf{D}}.\dot{\mathbf{D}}+\frac{\partial\hat{\psi}}{\partial T}.\dot{T}+\frac{\partial\hat{\psi}}{\partial\nabla T}.\left(\dot{\overline{\nabla T}}\right)+\frac{\partial\hat{\psi}}{\partial c_k}\dot{c}_k+\frac{\partial\hat{\psi}}{\partial\dot{c}_k}\ddot{c}_k+\frac{\partial\hat{\psi}}{\partial\nabla c_k}\left(\dot{\overline{\nabla c_k}}\right)+\frac{\partial\hat{\psi}}{\partial\mu_k}\dot{\mu}_k+\frac{\partial\hat{\psi}}{\partial\nabla\mu_k}.\left(\dot{\overline{\nabla\mu_k}}\right) \quad (5.36)$$

and by using the variational derivative of the free energy functional yields the relation

$$\begin{aligned}\dot{\psi}=&\frac{\partial\hat{\psi}}{\partial\mathbf{D}}.\dot{\mathbf{D}}+\frac{\partial\hat{\psi}}{\partial T}.\dot{T}+\frac{\partial\hat{\psi}}{\partial\nabla T}.\left(\nabla\dot{T}-\mathbf{D}.\nabla T\right)+\frac{\partial\hat{\psi}}{\partial c_k}\dot{c}_k+\frac{\partial\hat{\psi}}{\partial\dot{c}_k}\ddot{c}_k\\&+\frac{\partial\hat{\psi}}{\partial\nabla c_k}\left(\nabla\dot{c}_k-\mathbf{D}.\nabla c_k\right)+\frac{\partial\hat{\psi}}{\partial\mu_k}\dot{\mu}_k+\frac{\partial\hat{\psi}}{\partial\nabla\mu_k}.\left(\nabla\dot{\mu}_k-\mathbf{D}.\nabla\mu_k\right)\end{aligned} \quad \text{..... (5.37)}$$

By substituting Eq. (5.36) into Eq. (5.27) and using the Coleman-Noll entropy principle to place restrictions on the response functions, the following relations are derived:

$$\eta = -\frac{\partial \psi}{\partial T} \quad \text{..... (5.38)}$$

$$\mathbf{t}_k = \bar{\rho}\frac{\partial \psi}{\partial \nabla c_k} \quad \text{..... (5.39)}$$

$$\mu_k = \frac{\partial \psi}{\partial c_k} - \frac{1}{\bar{\rho}}\left(\nabla . \mathbf{t}_k + f_k\right) \quad \text{..... (5.40)}$$

$$\mathbf{J}_k = \bar{\rho}\frac{\partial \psi}{\partial \nabla \mu_k} . \mathbf{D} \quad \text{..... (5.41)}$$

$$\mathbf{T} = \bar{\rho}\sum_{k=1}^{\mathrm{N_f}} \frac{\partial \psi}{\partial \nabla c_k} . \nabla c_k + \bar{\rho}\,\nabla T . \frac{\partial \psi}{\partial \nabla T} + \mathbf{A}[\,\mathbf{D}\,] \quad \text{..... (5.42)}$$

and the reduced form of the entropy inequality is

$$\bar{\rho}\frac{\partial \psi}{\partial \nabla T} . \nabla \dot{T} + \bar{\rho}\sum_{k=1}^{\mathrm{N_f}} \frac{\partial \psi}{\partial \mu_k} . \dot{\mu}_k + \bar{\rho}\sum_{k=1}^{\mathrm{N_f}} \frac{\partial \psi}{\partial \nabla \mu_k} . \nabla \dot{\mu}_k + \frac{\mathbf{q}_\mathrm{r}}{T} . \nabla T \le 0 \quad \text{..... (5.43)}$$

It should be noted that the Coleman-Noll entropy principle states that the second postulate must hold for any thermodynamic process irrespective of the difficulty involved in producing such process in the laboratory. Thus, the above relations suggest that the response functions should each depend on the following independent variables

$$\psi = \hat{\psi}\left(T, \nabla T, c_k, \nabla c_k, \mu_k, \nabla \mu_k\right) \quad \text{..... (5.44)}$$

$$\mathbf{J}_k = \hat{\mathbf{J}}_k\left(\mathbf{D}, T, \nabla T, c_k, \nabla c_k, \mu_k, \nabla \mu_k\right) \quad \text{..... (5.45)}$$

$$\mathbf{t}_k = \hat{\mathbf{t}}_k\left(T, \nabla T, c_k, \nabla c_k, \mu_k, \nabla \mu_k\right) \quad \text{..... (5.46)}$$

$$\eta = \hat{\eta}\left(T, \nabla T, c_k, \nabla c_k, \mu_k, \nabla \mu_k\right) \quad \text{..... (5.47)}$$

$$\mathbf{q}_{\mathrm{r}} = \hat{\mathbf{q}}_{\mathrm{r}}\left(\mathbf{D}, T, \nabla T, c_k, \nabla c_k, \dot{c}_k, \mu_k, \nabla \mu_k\right) \quad \text{..... (5.48)}$$

$$\mathbf{T} = \hat{\mathbf{T}}\left(\mathbf{D}, T, \nabla T, c_k, \nabla c_k, \dot{c}_k, \mu_k, \nabla \mu_k\right) + \mathbf{A}\left(T, \nabla T, c_k, \nabla c_k, \dot{c}_k, \mu_k, \nabla \mu_k\right)\left[\mathbf{D}\right] \quad \text{..... (5.49)}$$

The derived relation for the chemical potential is same as the generalized chemical potential in Kim and Lowengrub (2005), except that the external micro-force is incorporated into equation (5.40). Another difference between the two models is the absent of a Lagrange multiplier in Eq. (5. 40), which Kim and Lowengrub introduced to exploit degeneracy in the quasi-incompressible mixture flow. As mentioned earlier, the foregoing model development assumes a compressible mixture.

Using a response function **A** that is linearly dependent on the velocity gradient suggests that the constitutive relation between the Cauchy stress and the independent variables is

$$\mathbf{T} = \bar{\rho} \sum_{k=1}^{\mathrm{N_f}} \frac{\partial \psi}{\partial \nabla c_k} \cdot \nabla c_k + \bar{\rho} \nabla T \cdot \frac{\partial \psi}{\partial \nabla T} - p\,\mathbf{I} + 2\mu\,\mathbf{D} + \lambda\left(\mathrm{tr}\,\mathbf{D}\right)\mathbf{I} \quad \text{..... (5.50)}$$

μ and λ are scalar functions of these independent variables $\left(T, \nabla T, c_k, \nabla c_k, \dot{c}_k, \mu_k, \nabla \mu_k\right)$, while *p* is fluid pressure. The constitutive relation shows that additional fluid stresses are introduced by gradient of concentration and temperature; the additional stress due to concentration gradients mimic the surface tension stresses.

It is obvious from these relations that rate dependency can only enter the constitutive model through heat flux and Cauchy stress. The diffusion flux depends on the velocity gradient of the mixture if the free energy is so constructed to incorporate the

chemical potentials of each species. By further restricting the free energy to not depend explicitly on the chemical potentials and their gradients, the response functions become

$$\psi = \hat{\psi}\left(T, \nabla T, c_k, \nabla c_k\right) \quad \text{(5.51)}$$

$$\mathbf{t}_k = \hat{\mathbf{t}}_k\left(T, \nabla T, c_k, \nabla c_k\right) \quad \text{(5.52)}$$

$$\eta = \hat{\eta}\left(T, \nabla T, c_k, \nabla c_k\right) \quad \text{(5.53)}$$

$$\mathbf{q}_{\mathrm{r}} = \hat{\mathbf{q}}_{\mathrm{r}}\left(\mathbf{D}, T, \nabla T, c_k, \nabla c_k, \dot{c}_k, \mu_k, \nabla \mu_k\right) \quad \text{(5.54)}$$

$$\mathbf{T} = \bar{\rho} \sum_{k=1}^{\mathrm{N_f}} \frac{\partial \psi}{\partial \nabla c_k} . \nabla c_k + \bar{\rho}\, \nabla T . \frac{\partial \psi}{\partial \nabla T} - p\, \mathbf{I} + 2\mu\, \mathbf{D} + \lambda\left(\mathrm{tr}\, \mathbf{D}\right)\mathbf{I} \quad \text{(5.55)}$$

In this case, μ and λ are scalar functions of the independent variables $\left[T, \nabla T, c_k, \nabla c_k, \dot{c}_k\right]$. The reduced form of the entropy inequality becomes

$$\sum_{k=1}^{\mathrm{N_f}} \pi_{d,k}\left(\mathbf{D}, T, \nabla T, c_k, \nabla c_k, \mu_k, \nabla \mu_k\right) \dot{c}_k + \bar{\rho} \frac{\partial \psi}{\partial \nabla T} . \nabla \dot{T} + \sum_{k=1}^{\mathrm{N_f}} \mathbf{J}_k . \nabla \mu_k + \frac{\mathbf{q}_{\mathrm{r}}}{T} . \nabla T \le 0 \quad \text{(5.56)}$$

$$\sum_{k=1}^{\mathrm{N_f}} \pi_{d,k}\left(\mathbf{D}, T, \nabla T, c_k, \nabla c_k, \mu_k, \nabla \mu_k\right) \dot{c}_k = \sum_{k=1}^{\mathrm{N_f}} \frac{\partial \psi}{\partial c_k} - \frac{1}{\bar{\rho}}\left(\nabla . \mathbf{t}_k + f_k\right) - \mu_k \quad \text{(5.57)}$$

For the inequality above to be satisfied for all $\left[\mathbf{D}, T, \nabla T, c_k, \nabla c_k, \dot{c}_k, \mu_k, \nabla \mu_k\right]$, it thus implies that

$$\sum_{k=1}^{N_f} \pi_{d,k}\left(\mathbf{D},T,\nabla T,c_k,\nabla c_k,\mu_k,\nabla\mu_k\right)\dot{c}_k = \\ -\bar{\rho}\frac{\partial\psi}{\partial\nabla T}.\nabla\dot{T} - \sum_{k=1}^{N_f}\mathbf{b}_k.\nabla\mu_k - \frac{\mathbf{q}_r}{T}.\nabla T - \sum_{k=1}^{N_f}\delta_k\left(\mathbf{D},T,\nabla T,c_k,\nabla c_k,\mu_k,\nabla\mu_k\right)\dot{c}_k \quad \text{..... (5.58)}$$

$$\mathbf{J}_k = -\hat{\mathbf{a}}_k\left(\mathbf{D},T,\nabla T,c_k,\nabla c_k,\mu_k,\nabla\mu_k\right)\dot{c}_k - \mathbf{M}_k\nabla\mu_k \quad \text{..... (5.59)}$$

$\boldsymbol{a}_k$ and $\boldsymbol{b}_k$ are arbitrary vectors, characterizing dissipation due to heterogeneities in each of the phases, $\boldsymbol{M}_k$ is the mobility tensor for component *k*, and δ_k is the net dissipation density. Therefore, by substituting equation (5.58) into (5.57), and considering each of the components of the mixture, the chemical potential is thus derived as

$$\mu_k - \mathbf{b}_k.\nabla\mu_k = \bar{\rho}\,c_k\frac{\partial\psi}{\partial\nabla T}.\nabla\dot{T} - \frac{\mathbf{q}_r}{T}.\nabla T + \frac{\partial\psi}{\partial c_k} - \frac{1}{\bar{\rho}}\left(\nabla.\mathbf{t}_k + f_k\right) + \delta_k\dot{c}_k \quad \text{..... (5.60)}$$

Eq. (5.60) assumes that all the species are in thermal equilibrium with each other in each part, *P*, of the continuum. Since each of the phases is assumed to be homogeneous and isotropic, except at the interfaces, vectors $\boldsymbol{a}_k$ and $\boldsymbol{b}_k$ will be zero.

5.3.6 Constructing the Free Energy Functional and Diffuse Interface Thickness

The free energy is constructed to account for both the bulk and interfacial energies. Cahn and Hilliard (1958) developed a framework for constructing free energy for two-phase problems. The choice of the free energy functional should support both forward and backward diffusion, thus, a generalized form of the Cahn-Hilliard free energy equation developed by Steinbach et al. (1995) is proposed in this work. Considering the dissipation due to the diffusion in each of the species, the total free energy density is constructed as

$$\psi = f_1(T) + f_2(c_k) + f_3(\nabla c_k) + f_4(\mu_k) \quad \text{..... (5.61)}$$

$f_1(T)$ is the free energy density due heat transfer in the mixture, $f_2(c_k)$ is the energy density due to the phobic effect among the phases, $f_3(\nabla c_k)$ is the energy responsible for the philic effect between the phases, and $f_4(\mu_k)$ is the dissipation density due to diffusion in each of the phases; this construction is unlike the classical definition of free energy as a function of concentration only. The gradient energy term also represents the nonlocal interactions between the phases, the mixing/blending of the phases.

The profile of the order parameter across the interface is dependent on the competition between the bulk and interfacial energies. Thus, the free energy of the mixture considering a slight deviation from thermal equilibrium among the phases is

$$\Psi = \int_{\Omega} \psi \; d\Omega \quad \text{..... (5.62)}$$

And substituting the equation (5.60) into (5.61) yields

$$\Psi = \int_{\Omega} \left\{ \begin{array}{l} f_1(T,\nabla T) + \sum_{k,\,j\,=\,1}^{N_f} \frac{1}{4a_{jk}} \left[c_j{}^2 c_k{}^2 - m_{jk} \left(\frac{1}{3} c_j{}^3 + c_j{}^2 c_k - \frac{1}{3} c_k{}^3 - c_k{}^2 c_j \right) \right] \\ + \sum_{k,\,j\,=\,1}^{N_f} \frac{\varepsilon_{jk}{}^2}{2} \left| c_k \nabla c_j - c_j \nabla c_k \right|^2 + \sum_{k\,=\,1}^{N_f} c_k \, \mu_k \end{array} \right\} d\,\Omega \quad \text{..... (5.63)}$$

Although multiphase systems are sensitive to the triple-point energies, these energies and other higher-order energies are disregarded as the physical assumption is that the triple point between the three different phases adjusts according to the dynamics of the dual phase boundaries. m_{jk} is the driving force for the phase transition between the phases at sharing interface contacts, and it is defined as the deviation from the two-phase

equilibrium between the two phases. This force depends on the temperature and mobility of the interface. But in this study, thermal equilibrium is assumed to exist between the phases, hence the total free energy becomes

$$\Psi = \int_{\Omega} \left\{ \begin{array}{l} f_1(T, \nabla T) + \sum_{k,\, j\, =\, 1}^{N_f} \frac{1}{4a_{jk}} \left[c_j^{\,2} c_k^{\,2} \right] + \sum_{k,\, j\, =\, 1}^{N_f} \frac{\varepsilon_{jk}^{\,2}}{2} \left| c_k \nabla c_j - c_j \nabla c_k \right|^2 \\ + \sum_{k\, =\, 1}^{N_f} c_k \mu_k \end{array} \right\} d\Omega \quad \text{..... (5.64)}$$

Based on the definition proposed by Wheeler et al. (1992), the surface tension, σ_{jk}, and thickness of the interface, λ_{jk}, are related according to

$$\varepsilon_{jk}^{\,2} = \lambda_{jk}\, \sigma_{jk} \quad \text{..... (5.65)}$$

Eq. (5.65) is defined as the interfacial (gradient) energy coefficient which is often assumed to be constant for simplicity.

$$a_{jk} = \frac{\lambda_{jk}}{72\, \sigma_{jk}} \quad \text{..... (5.66)}$$

The determination of the interface width is controlled by the concentrations of each phase and the bulk-free energies. Van-der-Waals (1893) hypothesized that equilibrium interphase profile minimizes the free energy, and at equilibrium the chemical potential is zero. Then, by using calculus of variation, the three coupled governing equations relating the interface widths with the phase concentrations are (assuming equilibrium conditions)

$$\frac{36\sigma_{12}}{\lambda_{12}}c_2{}^2c_1+\frac{36\sigma_{13}}{\lambda_{13}}c_3{}^2c_1+\lambda_{12}\sigma_{12}\left(c_1\nabla c_2-c_2\nabla c_1\right)\nabla c_2$$
$$+\lambda_{13}\sigma_{13}\left(c_1\nabla c_3-c_3\nabla c_1\right)\nabla c_3+\nabla\left\{\lambda_{12}\sigma_{12}\left(c_1\nabla c_2-c_2\nabla c_1\right)c_2\right\} \quad \text{..... (5.67a)}$$
$$+\nabla\left\{\lambda_{13}\sigma_{13}\left(c_1\nabla c_3-c_3\nabla c_1\right)c_3\right\}+\frac{\delta f_1}{\delta c_1}=0$$

$$\frac{36\sigma_{12}}{\lambda_{12}}c_1{}^2c_2+\frac{36\sigma_{23}}{\lambda_{23}}c_3{}^2c_2-\lambda_{12}\sigma_{12}\left(c_1\nabla c_2-c_2\nabla c_1\right)\nabla c_1$$
$$+\lambda_{23}\sigma_{23}\left(c_2\nabla c_3-c_3\nabla c_2\right)\nabla c_3+\nabla\left\{\lambda_{12}\sigma_{12}\left(c_1\nabla c_2-c_2\nabla c_1\right)c_1\right\} \quad \text{..... (5.67b)}$$
$$+\nabla\left\{\lambda_{23}\sigma_{23}\left(c_2\nabla c_3-c_3\nabla c_2\right)c_3\right\}+\frac{\delta f_1}{\delta c_2}=0$$

$$\frac{36\sigma_{13}}{\lambda_{13}}c_1{}^2c_3+\frac{36\sigma_{23}}{\lambda_{23}}c_2{}^2c_3-\lambda_{13}\sigma_{13}\left(c_1\nabla c_3-c_3\nabla c_1\right)\nabla c_1$$
$$-\lambda_{23}\sigma_{23}\left(c_2\nabla c_3-c_3\nabla c_2\right)\nabla c_2-\nabla\left\{\lambda_{13}\sigma_{13}\left(c_1\nabla c_3-c_3\nabla c_1\right)c_1\right\} \quad \text{..... (5.67c)}$$
$$-\nabla\left\{\lambda_{23}\sigma_{23}\left(c_2\nabla c_3-c_3\nabla c_2\right)c_2\right\}+\frac{\delta f_1}{\delta c_3}=0$$

The general boundary conditions derived from calculus of variation are

$$\left\{\lambda_{12}\sigma_{12}\left(c_1\nabla c_2-c_2\nabla c_1\right)c_2+\lambda_{13}\sigma_{13}\left(c_1\nabla c_3-c_3\nabla c_1\right)c_3\right\}\delta c_1\Big]_{-\infty}^{+\infty}\Big]_{-\infty}^{+\infty}=0 \quad \text{..... (5.68a)}$$

$$\left\{\lambda_{12}\sigma_{12}\left(c_1\nabla c_2-c_2\nabla c_1\right)c_1-\lambda_{23}\sigma_{23}\left(c_2\nabla c_3-c_3\nabla c_2\right)c_2\right\}\delta c_2\Big]_{-\infty}^{+\infty}\Big]_{-\infty}^{+\infty}=0 \quad \text{..... (5.68b)}$$

$$\left\{\lambda_{13}\sigma_{13}\left(c_1\nabla c_3-c_3\nabla c_1\right)c_1+\lambda_{23}\sigma_{23}\left(c_2\nabla c_3-c_3\nabla c_2\right)c_2\right\}\delta c_3\Big]_{-\infty}^{+\infty}\Big]_{-\infty}^{+\infty}=0 \quad \text{..... (5.68c)}$$

At the boundaries of each phases, far from the interfaces, the mass concentrations are specified to be 1, thus implying the variation of the mass concentrations will be zero.

Similarly, at these boundaries, there are no influx, therefore, $\boldsymbol{n}.\nabla c_k = 0$; $\boldsymbol{n}$ is the unit normal vector to the boundary surfaces. There are many models describing the relationship between the phase concentration and interface thickness for binary systems (Jacqmin 1999, Pengtao et al. 2004, Badalassi et al. 2003, Anderson et al. 1998, Kim 2012). The major difference in these models is in the definition of the bulk free energy. They assumed isothermal transport process and no dissipation during the diffusion of the species to the interfaces. Equations (5.68a, 5.68b, and 5.68c) define the relationship between the interfacial width of a flat surface and the concentrations at a point in time (quasi-equilibrium). Cahn and Hilliard (1959) extended van-der-Waals' hypothesis to a time-dependent scenario:

$$\frac{Dc_k}{Dt} = \nabla.\mathbf{M}_k \nabla\left(\frac{\delta \Psi}{\delta c_k}\right) \quad \text{..... (5.69)}$$

The surface tensions acting at each interface increases as the temperature increases, but the thickness of the interface reduces with increase in temperature. Therefore, for the foregoing problem, the surface tension acting at each interface, at equilibrium, is determined by substituting the relationship between the concentrations and interfacial widths in Eq. 67 into the free energy density relation, to obtain,

$$\Psi = \int_{-\infty}^{+\infty} \left\{ f_1(T, \nabla T) + \sum_{k,j=1}^{N_f} \frac{1}{4a_{jk}} \left[c_j^2 c_k^2 \right] + \sum_{k,j=1}^{N_f} \frac{\varepsilon_{jk}^2}{2} \left| c_k \nabla c_j - c_j \nabla c_k \right|^2 \right\} dz \quad \text{..... (5.70)}$$

z is the coordinate axis normal to the interface.

5.4 Governing Field Equations

The governing field equations, based on continuum phase field model, for the flow of multicomponent fluid are essentially the balance of linear momentum, mass concentration equation, equation of chemical potential, balance of internal configurational forces, continuity equation of the mixture, and energy equation; these relations consider the hydrodynamic interactions among the species.

Substituting Eq. (5.59) into Eq. (5.15), and assuming isotropy, the mass concentration equations become

$$\bar{\rho}\,\dot{c}_k = \nabla\cdot\mathbf{M}_k\nabla\mu_k + \dot{m}_k \quad \text{..... (5.71)}$$

Furthermore, by substituting Eq. (5.50) into Eq. (5.18), the linear momentum equation of the mixture yields

$$\bar{\rho}\,\dot{\mathbf{u}} = \nabla\cdot\left\{\bar{\rho}\sum_{k=1}^{N_f}\frac{\partial\psi}{\partial\nabla c_k}\cdot\nabla c_k + \bar{\rho}\,\nabla T\cdot\frac{\partial\psi}{\partial\nabla T} - p\,\mathbf{I} + 2\mu\,\mathbf{D} + \lambda\,(\mathrm{tr}\,\mathbf{D})\mathbf{I}\right\} + \bar{\rho}\,\mathbf{g}_c \quad \text{..... (5.72)}$$

By substituting Eq. (5.39) into Eq. (5.26), the balance of internal configurational forces is

$$\nabla\cdot\bar{\rho}\frac{\partial\psi}{\partial\nabla c_k} + g_k + f_k = 0 \quad \text{..... (5.73)}$$

Similarly, by replacing the definition of the microstress tensor into the chemical potential equation, it yields

$$\mu_k = \bar{\rho}\,c_k\frac{\partial\psi}{\partial\nabla T}\cdot\nabla\dot{T} - \frac{\mathbf{q}_r}{T}\cdot\nabla T + \frac{\partial\psi}{\partial c_k} - \frac{1}{\bar{\rho}}\left(\nabla\cdot\bar{\rho}\frac{\partial\psi}{\partial\nabla c_k} + f_k\right) \quad \text{..... (5.74)}$$

The continuity equation of the mixture is

$$\frac{\partial \bar{\rho}}{\partial t} + \nabla.\left(\bar{\rho}\,\dot{\mathbf{y}}\right) = \sum_{k=1}^{N_f} \dot{m}_k = 0 \quad \text{.....(5.13)}$$

Finally, by substituting the expressions of the Cauchy stress and microstress tensors into Eq. (5.23), and using the thermodynamic relations between enthalpy and internal energy, the energy equation of the system becomes

$$\begin{aligned}\bar{\rho}\sum_{k=1}^{N_f} C_{p,k} c_k \left(\frac{\partial T}{\partial t} + \mathbf{u}.\nabla T\right) + \nabla.\,\mathbf{q}_r = \bar{\rho}\, r + \sum_{k=1}^{N_f} \nabla.\left(\bar{\rho}\,\frac{\partial \psi}{\partial \nabla c_k}\dot{c}_k\right) + \sum_{k=1}^{N_f} f_k \dot{c}_k \\ + \sum_{k=1}^{N_f} \alpha_k c_k \left(\frac{\partial p}{\partial t} + \mathbf{u}.\nabla p\right) + \left\{\bar{\rho}\sum_{k=1}^{N_f} \frac{\partial \psi}{\partial \nabla c_k}.\nabla c_k + \bar{\rho}\,\nabla T.\frac{\partial \psi}{\partial \nabla T} - p\,\mathbf{I} + 2\mu\,\mathbf{D} + \lambda\left(\mathrm{tr}\,\mathbf{D}\right)\mathbf{I}\right\}.\mathbf{D}\end{aligned} \quad (5.75)$$

$C_{p,k}$ is specific heat capacity at constant pressure for each species and α_k is the bulk expansion coefficient; this property is determined from equations for state, for gases.

When solving the field equations for a three-dimensional domain, there are eight dependent variables to be solved for, which are velocity vector (3-dependent variables), pressure of the mixture (1-dependent variable), temperature of the mixture (1-dependent variable), and mass concentrations of each phase (3-dependent variables).

5.5 Summary

A thermodynamically consistent multiphase-field model is developed for the flow of gas, liquid, and cavings mixture in the wellbore. The internal workings due to the internal configurational force system in the bulk of each phase are incorporated into the model. Using Coleman-Noll entropy principle to place restrictions on the proposed response functions, which are defined to obey Truesdell principle of equipresence, it is

derived that the mixture stress tensor is a function of effective viscosity of the mixture, temperature gradient, and mass concentration gradients of each species of the mixture. The additional stress due to concentration gradient mimics surface tension, while the additional stress due to temperature gradient is another non-local constitutive behavior of the mixture as a result of a non-isothermal transport process.

6. A QUICK AND ENERGY CONSISTENT ANALYTICAL METHOD FOR PREDICTING HYDRAULIC FRACTURE PROPAGATION THROUGH HETEROGENEOUS LAYERED MEDIA AND FORMATIONS WITH NATURAL FRACTURES: THE USE OF AN EFFECTIVE FRACTURE TOUGHNESS

6.1 Scope

An effective fracture toughness, based on equivalent energy release-rate hypothesis is presented for homogenizing heterogeneous layered media. Using crack closure method, the energy released when a mode-1 fracture propagates through an equivalent homogenized layer is equated to the sum of the energies released in the heterogeneous layered media. And from extensive numerical experiments, the predictions of fracture tips' positions through this proposed method are of the same range of accuracy as the known linear blend rule; the weakest link arguments technique performed poorly when compared to the other two methods. Therefore, homogenizing heterogeneous layered media with energy consistent approach will reduce the complexities associated with modeling fracture propagation in multi-layer without losing accuracy. Furthermore, an effective fracture toughness, based on equivalent energy release rate, equivalent strain energy, and modified Kachanov's damage theory is presented in this study. The proposed approach will reduce the computation time required in predicting fracture containment potential in formations with opened or sealed natural fractures. And comparing the proposed phenomenological model with the rigorous solution provided by Mori-Tanaka, it was observed that the margin of error was negligible. The benefit of the proposed

phenomenological model over the Mori-Tanaka's effective shear modulus model is the ease of estimating the effective fracture toughness. Thus, these models can be applied to quickly estimate the potential for hydraulic fracture containment or broaching possibilities during oil and gas blowouts and fracturing operations.

6.2 Background on Hydraulic Fracture Modeling and Effective Fracture Toughness

"Pseudo-3D" (P-3D) models are often used for quick hydraulic fracturing design or prediction of hydraulic fracture containment in the petroleum industry; these models are less computationally expensive compared to the fully 3D and planar 3D models (Brady et al. 1993, Clifton and Abou-Sayed 1979, 1981, Hirth and Lothe 1968, and Bui 1977). In the P-3D models, the fluid flow is assumed to be one-dimensional along the length of the fracture, while the pressure profile in each elliptic cross sections is constrained to be linear. And as assumed in the PKN model (Perkins and Kern 1961, Nordgren 1972) that the cross sections are independent of each other, so that the plane strain assumption decouples the fluid flow and solid mechanics; similarly, this constraint is applied in the P3D models. The linear pressure profile in the cross sections is based on the assumption that the vertical fracture extension is slow such that the dynamic pressure gradient in the vertical sections is negligible.

Many authors have contributed to the development of the equilibrium height problem (P-3D), starting from the work of Simonson et al. (1978), who developed the model for symmetric 3-layer formation, with constant internal applied pressure. Ahmed (1984), and Newberry et al. (1985) solved an asymmetric 3-layer equilibrium height

problem; while Fung et al. (1987) and Economides and Nolte (2000) extended the asymmetric equilibrium height problem to multi-layer formations with constant and linearly varying pressure profiles in the vertical sections respectively. But as pointed out by Liu and Valko (2015), the model developed by Economides and Nolte has some intrinsic errors; and sometimes yield unacceptable results. Other notable contributions to the development of the P-3D models include Palmer and Carroll (1982, 1983), Palmer and Craig (1984), Settari (1986), Meyer (1986), Advani et al. (1990), and Adachi et al. (2010).

Analytical P-3D model for asymmetric multi-layer formations with linearly varying pressure profile in each cross section is very complicated, and difficult to tract. To reduce the complexity, an effective fracture toughness, based on equivalent energy release rate, developed for the upper and lower layers will condense the multi-layer problem to the classical three-layer problem, which algebra is tractable.

In the same vein, we also proposed in this paper the use of an effective fracture toughness, based on the same hypothesis mentioned earlier, which can approximately describe hydraulic fracture propagation in formations with natural fractures. The interactions between hydraulic and natural fractures have been studied by many authors in the past (Olson and Dahi 2009, Zhou et al. 2015, Renshaw and Pollard 1995, Dahi and Olson 2011, Gu et al. 2012, Gu and Weng 2010, Chuprakov et al. 2013, Zhou et al. 2008, Warpinski and Teufel 1987, Gao and Rice 1989, Wu and Olson 2014). From the various studies, there are three possibilities that may occur when a hydraulic fracture intersect a natural fracture: (1) the hydraulic fracture may cross the natural fracture without change in propagation direction (2) the hydraulic fracture is arrested by the natural fracture;

consequently, the natural fracture, becoming part of the hydraulic fracture network and propagates from its end(s) or (3) from a weak point along its length.

In this study, the complex hydraulic fracture network created by the interactions of the parent hydraulic fracture with ordered and disordered natural fractures will be simplified such that an effective fracture toughness, dependent on area of the discontinuities of a representative volume element and the mechanical properties of the formation matrix can suggest the containment potential of the hydraulic fracture in the host formation.

In past studies, the use of linear blend rule (Atkins 1980, Atkins and Mai 1985, Eriksson and Atkins 1995, and Eriksson 1998) and weakest link arguments (Landes and Shaffer 1980, Wallin et al. 1984, Slatcher 1986, Iwadate et al. 1983, Beremin 1983, Sainte et al. 1995) have been used to homogenize heterogeneous layered media. However, Heerens et al. (1994) showed that the predictions through the weakest link method are inaccurate.

6.3 Mathematical Formulations

6.3.1 Effective Fracture Toughness for Layered Media

Fractures tend to grow in the direction that maximizes the potential energy released. And as a result, most hydraulic fractures propagate in mode-1; although diversion may occur at the boundary of two formations or when intercepted by natural fractures. In this study, the hydraulic fracture is assumed to propagate through boundaries in mode-1 only.

As the hydraulic fracture propagates through each formation, there is an increase in the total energy released; and considering Fig. 6.1, the total energy released is

$$\Pi_T = \int_{-H_1}^{H_N} \int_{0}^{L} G_1 \, dx \, dz \quad \text{..... (6.1)}$$

where G_1 is the energy release rate, as defined by Griffith (1921). Layers $n+1$ to N can be lumped together as a heterogeneous formation having a varying fracture toughness $K_{c,3}(z)$, while layers 1 to $n-1$ are also lumped together as a heterogeneous formation 1, having mode-1 fracture toughness $K_{c,1}(z)$. Therefore, the multi-layer equilibrium-height problem reduces to the classical three-layer problem (Fig. 6.2).

Assuming the formations have a linearly elastic response, the energy released per unit length of the fracture is

$$\Pi = \int_{0}^{H_N} G_{1+} \, (-dz) + \int_{0}^{H_1} G_{1-} \, dz \quad \text{..... (6.2)}$$

Using superposition theorem, the normal stresses at the tips of the vertical fracture plane (in the y-z plane) at arbitrary positions z_0 and z_1 are

$$\sigma_{yy}(z=-z_1) = \sigma_{yy}{}^{-} = -S_{h\min}(z=z_1) + \frac{K_{I-}}{\sqrt{2\pi(z)}} \quad \text{..... (6.3)}$$

$$\sigma_{yy}(z=z_0) = \sigma_{yy}{}^{+} = -S_{h\min}(z=-z_0) + \frac{K_{I+}}{\sqrt{2\pi(-z)}} \quad \text{..... (6.4)}$$

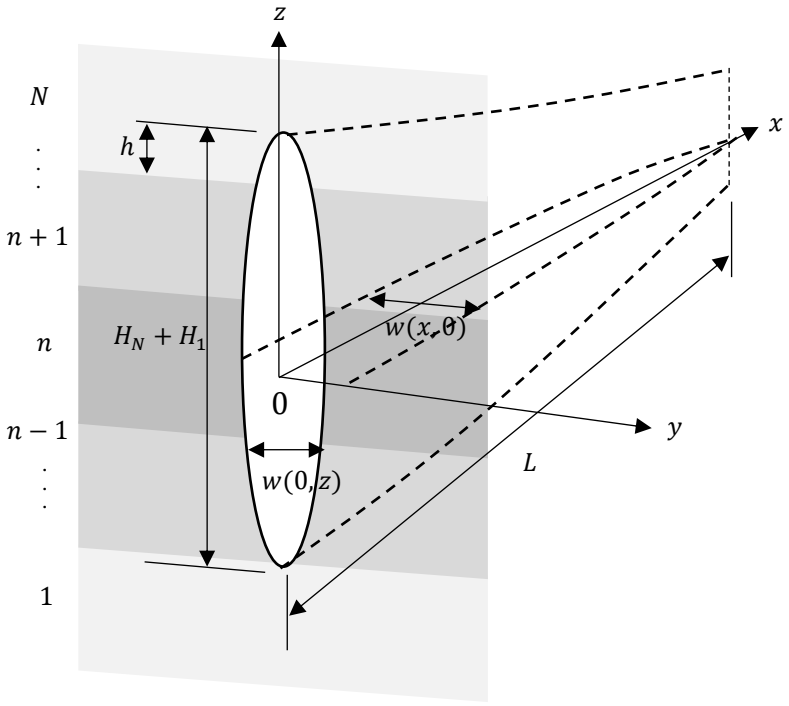

Fig. 6.1. Asymmetric multilayer hydraulic fracture propagation.

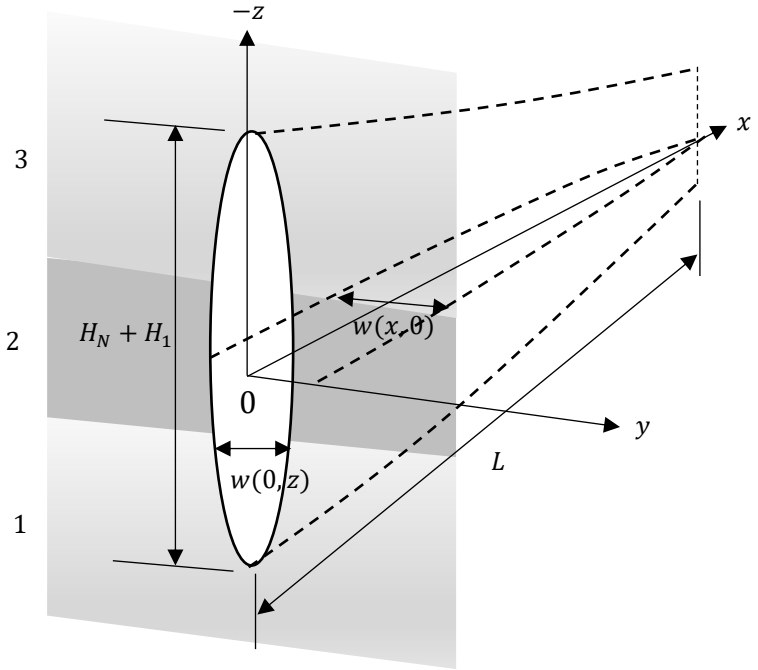

Fig. 6.2. Asymmetric three-layer equilibrium height problem.

with the extension of the upper tip by z_0, new fracture surfaces are created in $0 \le z \le z_0$ and the displacement of the upper-right face is

$$u_{yy}{}^{+} = \frac{\kappa+1}{4\mu\pi} K_{I+} \sqrt{2\pi(z_0 - z)} \quad \text{..... (6.5)}$$

Using crack closure method (Irwin 1958 and Broek 1991), the work done by the normal stress in the fracture extension is equal to the energy required to close the fracture after opening

$$\Pi^{+} = 2\int_0^{z_0} \frac{1}{2} \sigma_{yy}{}^{+} u_{yy}{}^{+} \, dz \quad \text{..... (6.6)}$$

The factor 2 in Eq.6.6 accounts for the right and left surfaces of the fracture. And $2u_{yy}{}^{+}(z) = w^{+}(0,z)$. Therefore, the total energy released when the upper fracture tip propagates from the bottom of formation *n+1* to point *h* from the bottom of layer *N* is

$$\begin{aligned} \Pi^{+} = & \int_0^{h_{n+1}} \sigma_{yy,n+1} \frac{\kappa_{n+1}+1}{4\mu_{n+1}\pi} K_{Ic,n+1} \sqrt{2\pi(h_{n+1} - z)} \, dz \\ & + \int_{h_{n+1}}^{h_{n+2}} \sigma_{yy,n+2} \frac{\kappa_{n+2}+1}{4\mu_{n+2}\pi} K_{Ic,n+2} \sqrt{2\pi(h_{n+2} - h_{n+1} - z)} \, dz + \ldots \\ & \ldots + \int_{h_{N-1}}^{h_{N-1}+h} \sigma_{yy,N} \frac{\kappa_N+1}{4\mu_N\pi} K_{Ic,N} \sqrt{2\pi(h - z)} \, dz \end{aligned} \quad \text{..... (6.7)}$$

Where, the Irwin (1957) criterion, $K_I = K_{IC}$ was implied in Eq. 6.7. From Fig. 6.2, the equivalent energy released, as the upper tip propagates into the abutting layer (lumped), is

$$\overline{\Pi}^{+} = \int_0^{h_{N-1}+h} \sigma_{yy}(z) \frac{\overline{\kappa}+1}{4\overline{\mu}\pi} \overline{K_{Ic}}^{+}(z) \sqrt{2\pi(h - z)} \, dz \quad \text{.....(6.8)}$$

Hence, the effective fracture toughness for the lumped upper layer, $\overline{K_{IC}}^{+}$ can be estimated from the hypothesis that $\overline{\Pi}^{+} = \Pi^{+}$. Supposing the in-situ stresses are uniformly distributed throughout each layer, and the upper layers are lumped as a homogeneous formation with fracture toughness, $\overline{K_{IC}}^{+}$, therefore, the effective fracture toughness of the upper layer can be determined from the algebraic expression below. It should be noted that a Heaviside function was used to represent the uniformly distributed in-situ stresses in each layer in Eq. 6.8 above. And $\bar{\kappa}$ and $\bar{\mu}$ are averaged properties (Poisson ratio function and shear modulus respectively) of the formations; for plane strain approximation, $\bar{\kappa} = 3 - 4\bar{\nu}$ and plane stress $\bar{\kappa} = (3-\bar{\nu})/(1+\bar{\nu})$.

$$\sqrt{2\pi}\,\frac{\bar{\kappa}+1}{4\bar{\mu}\pi}\overline{K_{IC}}^{+}\left\{-\frac{2}{3}\left[\sum_{n=1}^{N} S_{h\min,n}\left(h_{N-1}+h-h_{n-1}\right)^{\frac{3}{2}} - S_{h\min,n}\left(h_{N-1}+h-h_{n}\right)^{\frac{3}{2}}\right]\right\}$$

$$+\frac{\bar{\kappa}+1}{8\bar{\mu}}\left(\overline{K_{IC}}^{+}\right)^{2}\left(h_{N-1}+h\right) = \left[\sum_{n=1}^{N} -\frac{2\sqrt{2\pi}}{3} S_{h\min,n}\,\frac{\kappa_n+1}{4\mu_n\pi} K_{IC,n}\left(h_{n}-h_{n-1}\right)^{\frac{3}{2}} + \frac{\kappa_n+1}{8\mu_n} K_{IC,n}{}^{2}\left(h_{n}-h_{n-1}\right)\right] \quad \text{.....(6.9)}$$

Alternatively, the shear modulus and Poisson ratio can also be represented with Heaviside functions, which will further make Eq. 6.9 more complicated. Similarly, the effective fracture toughness for the formations below the host formation can be estimated from Eq. 6.10

$$\sqrt{2\pi}\,\frac{\bar{\kappa}+1}{\bar{\mu}}\overline{K_{IC}}^{-}\left\{-\frac{2}{3}\left[\sum_{n=1}^{M}S_{h\min,n}\left(h_{M-1}+h-h_{n-1}\right)^{\frac{3}{2}}-S_{h\min,n}\left(h_{M-1}+h-h_{n}\right)^{\frac{3}{2}}\right]\right\}$$

$$+\frac{\bar{\kappa}+1}{8\bar{\mu}}\left(\overline{K_{IC}}^{-}\right)^{2}\left(h_{M-1}+h\right)=\left[\begin{array}{l}\displaystyle\sum_{n=1}^{M}-\frac{2\sqrt{2\pi}}{3}S_{h\min,n}\frac{\kappa_n+1}{4\mu_n\pi}K_{IC,n}\left(h_{n}-h_{n-1}\right)^{\frac{3}{2}}\\ +\dfrac{\kappa_n+1}{8\mu_n}K_{IC,n}{}^{2}\left(h_{n}-h_{n-1}\right)\end{array}\right] \qquad \text{..... (6.10)}$$

6.3.2 Effective Fracture Toughness Derivation Without Tensile Stresses

As fracture propagates through each medium, the tensile forces acting on the fracture edges, away from the tips reduces with crack length. Thus, neglecting the tensile force contributions and following the same procedure in Section 6.3.1 above, the effective fracture toughness for the homogenized upper and lower barriers, based on equivalent energy-release rate hypothesis are derived as

$$\overline{K}_{IC}{}^{+}=\frac{\displaystyle\sum_{n=1}^{N}\frac{\kappa_n+1}{\mu_n}S_{h\min,n}K_{IC,n}\left(h_n-h_{n-1}\right)^{\frac{3}{2}}}{\dfrac{\bar{\kappa}+1}{\bar{\mu}}\displaystyle\sum_{n=1}^{N}S_{h\min,n}\left\{\left(h_{N-1}+h-h_{n-1}\right)^{\frac{3}{2}}-\left(h_{N-1}+h-h_{n}\right)^{\frac{3}{2}}\right\}} \qquad \text{..... (6.11)}$$

$$\overline{K}_{IC}{}^{-}=\frac{\displaystyle\sum_{n=1}^{M}\frac{\kappa_n+1}{\mu_n}S_{h\min,n}K_{IC,n}\left(h_n-h_{n-1}\right)^{\frac{3}{2}}}{\dfrac{\bar{\kappa}+1}{\bar{\mu}}\displaystyle\sum_{n=1}^{M}S_{h\min,n}\left\{\left(h_{M-1}+h-h_{n-1}\right)^{\frac{3}{2}}-\left(h_{M-1}+h-h_{n}\right)^{\frac{3}{2}}\right\}} \qquad \text{..... (6.12)}$$

6.3.3 Minimum Fracture Extension Pressures

When the pressure driving the hydraulic fracture is assumed to be constant, the fracture extension pressure was derived by Simonson et al. (1978) as

$$P_F = S_{2,h\min}(z) + \frac{K_{IC}}{\sqrt{\pi h_\xi}} \quad \text{..... (6.13)}$$

where, h_ξ is the half thickness of the host formation. But when the displacements of the upper and lower tips of the fracture are significant, the hydrostatic pressure can significantly affect the extension potential.

The fracture extension pressure may not only be affected by gravity, but the relative positions of the fracture tips can affect the value. Considering the three different cases in Fig. 6.3. The critical extension pressures for the lower and upper tips in case 1 respectively, as derived in the Appendix A are

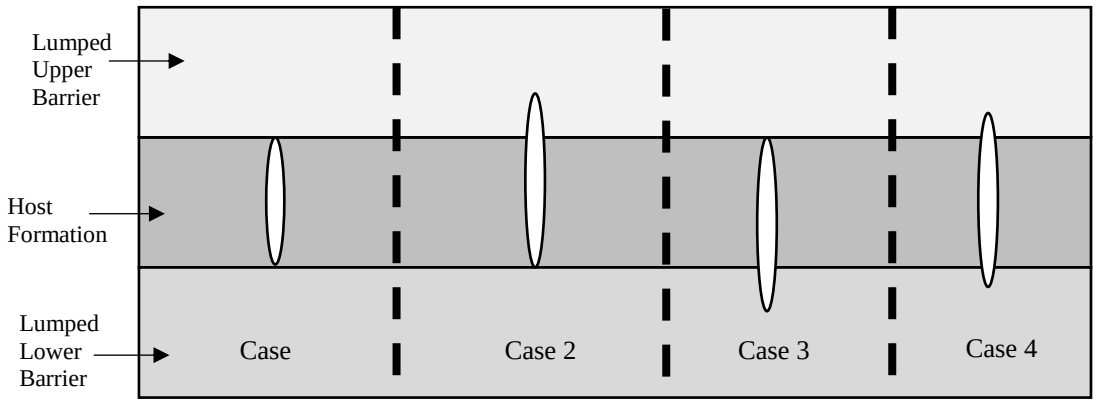

Fig. 6.3.Possible fracture tips positions in three-layer media.

$$P_{FD} = \left(\frac{\overline{K_{IC}}^{-}}{\sqrt{\pi h_\xi}} + S_{2,h\min} - \frac{1}{2} g h_\xi \rho \right) \quad \text{.....(6.14)}$$

$$P_{FU} = \left(\frac{\overline{K_{IC}}^{+}}{\sqrt{\pi h_\xi}} + S_{2,h\min} + \frac{1}{2} g h_\xi \rho \right) \quad \text{.....(6.15)}$$

$$P_{FU} = \frac{2\overline{K_{IC}}^{+}\sqrt{\pi} + \sqrt{h_\xi}\left\{ g h_\xi \pi\rho + 2\left[\begin{array}{l} S_{3,h\min}\sqrt{1-k_3^{\,2}} \\ +\left(-\sqrt{\frac{1+k_3}{1-k_3}} + k_3\sqrt{\frac{1+k_3}{1-k_3}} + \pi \right) S_{2,h\min} \end{array} \right] \right\}}{2\sqrt{h_\xi}\left(-\sqrt{\frac{1+k_3}{1-k_3}} + k_3\sqrt{\frac{1+k_3}{1-k_3}} + \sqrt{1-k_3^{\,2}} + \pi \right)} \quad \text{..... (6.16)}$$
$$+ \frac{4\sqrt{h_\xi}\left(S_{3,h\min} - S_{2,h\min}\right)\arcsin\left[\sqrt{\frac{1-k_3}{2}}\right]}{2\sqrt{h_\xi}\left(-\sqrt{\frac{1+k_3}{1-k_3}} + k_3\sqrt{\frac{1+k_3}{1-k_3}} + \sqrt{1-k_3^{\,2}} + \pi \right)}$$

$$P_{FD} = \frac{\sqrt{k_3+1}\left\{ g h_\xi \pi\rho + 2\left[S_{3,h\min}\sqrt{\frac{1-k_3}{1+k_3}}\left(1+k_3\right) - \left(\sqrt{\frac{1-k_3}{1+k_3}} k_3 + \sqrt{\frac{1-k_3}{1+k_3}} + \pi \right) S_{2,h\min} \right] \right\}}{2\left\{ k_3\left(\sqrt{1-k_3} - \sqrt{\frac{1-k_3}{1+k_3}}\sqrt{1+k_3} \right) + \sqrt{1-k_3} - \sqrt{\frac{1-k_3}{1+k_3}}\sqrt{1+k_3} - \pi\sqrt{1+k_3} \right\}} \quad \text{..... (6.17)}$$
$$- \frac{2\overline{K_{IC}}^{-}\sqrt{\pi}\sqrt{\frac{1+k_3}{h_\xi}} - 4\sqrt{k_3+1}\left(S_{3,h\min} - S_{2,h\min}\right)\arcsin\left[\sqrt{\frac{1-k_3}{2}}\right]}{2\left\{ k_3\left(\sqrt{1-k_3} - \sqrt{\frac{1-k_3}{1+k_3}}\sqrt{1+k_3} \right) + \sqrt{1-k_3} - \sqrt{\frac{1-k_3}{1+k_3}}\sqrt{1+k_3} - \pi\sqrt{1+k_3} \right\}}$$

Noting that $S_{2,h\min}$ is the minimum principal in-situ stress at the host formation. Cases 2 and 3 are not very common; but could be relevant to the extension of existing fractures in formations. In case 2, the critical extension pressures for the upper and lower tips are respectively derived in Appendix A as shown in Eq. 6.18 and Eq. 6.19 respectively.

Noting that, $k_3 = \frac{h_\xi}{h_u + h_\xi}$, where h_u is the displacement of the upper tip. For case 3, the critical extension pressures for the upper and lower tips are

$$P_{FU} = \frac{2\overline{K_{IC}}^{+}\sqrt{\pi} + \sqrt{h_\xi}\left\{ gh_\xi \pi\rho + 2\left[S_{2,h\min}\sqrt{1-k_1^{\,2}} - \left(\sqrt{\frac{1-k_1}{1+k_1}} + k_1\sqrt{\frac{1-k_1}{1+k_1}} - \pi \right) S_{1,h\min} \right] \right\}}{2\sqrt{h_\xi}\left(-\sqrt{\frac{1-k_1}{1+k_1}} - k_1\sqrt{\frac{1-k_1}{1+k_1}} + \sqrt{1-k_1^{\,2}} + \pi \right)} \quad \text{.. (6.18)}$$

$$+ \frac{4\sqrt{h_\xi}\left(S_{2,h\min} - S_{1,h\min}\right)\arcsin\left[\sqrt{\frac{1+k_1}{2}}\right]}{2\sqrt{h_\xi}\left(-\sqrt{\frac{1-k_1}{1+k_1}} - k_1\sqrt{\frac{1-k_1}{1+k_1}} + \sqrt{1-k_1^{\,2}} + \pi \right)}$$

$$P_{FD} = \frac{\sqrt{\frac{\pi}{h_\xi}}\overline{K_{IC}}^{-} - gh_\xi\pi\rho - \left[\begin{array}{l} S_{2,h\min}\sqrt{\frac{1+k_1}{1-k_1}} + k_1 S_{2,h\min}\sqrt{\frac{1+k_1}{1-k_1}} \\ + S_{1,h\min}\sqrt{1-k_1^{\,2}} + \pi S_{1,h\min} \end{array} \right]}{\left(-\sqrt{\frac{1+k_1}{1-k_1}} + k_1\sqrt{\frac{1+k_1}{1-k_1}} + \sqrt{1-k_1^{\,2}} + \pi \right)} \quad \text{..... (6.19)}$$

$$+ \frac{gh_\xi\rho\arcsin\left[\sqrt{\frac{1-k_1}{2}}\right] + \left(gh_\xi\rho + 2S_{2,h\min} - 2S_{1,h\min}\right)\arcsin\left[\sqrt{\frac{1+k_1}{2}}\right]}{2\sqrt{h_\xi}\left(-\sqrt{\frac{1+k_1}{1-k_1}} + k_1\sqrt{\frac{1+k_1}{1-k_1}} + \sqrt{1-k_1^{\,2}} + \pi \right)}$$

And $k_1 = \frac{h_\xi}{h_d + h_\xi}$.

6.3.4 Effective Fracture Toughness for Formations with Disordered Natural Fractures

The growth of hydraulic fractures in formations with natural fractures depends on many factors, including the orientation of the micro cracks, the infill materials in the cracks, the tensile strength of the rock, treatment pressure, fluid viscosity, and many other factors as studied by Zhou et al. 2015. To describe the random path of the hydraulic

fracture in disordered natural fracture network will be very complicated. But the use of damage theory with the crack closure method (described above) can approximately suggest the containment potential of the hydraulic fracture.

Sometimes the natural fractures may be filled with materials that have higher modulus than the rock matrix; on the other hand the infill materials may have lower Young's modulus than the matrix. The surface density of the cracks and its mechanical strength affect the bearing capacity of the crack-matrix system. If the cracks are filled with higher modulus materials, they help to reinforce the strength of the crack-matrix system; but when the cracks are empty or filled with lower modulus materials, there is a reduction in the bearing capacity of the crack-matrix system. This is the crux of the effective stress introduced by Kachanov (2013); in the classical continuum damage theory, the inclusions are empty; thus, this study will cover both opened and filled discontinuities. For disordered natural fracture network, the impact of the inclinations of the natural fractures to the propagating hydraulic fracture cannot be included in the model development in a deterministic way, except by the use of random theory, which we have decided not to pursue in this paper.

As mentioned in the previous section, the effective fracture toughness that describes the containment potential of the hydraulic fracture, propagating in the rock with natural fractures, is based on the use of equivalent energy released rate and equivalent strain energy (by compressional loading) hypotheses. In the equivalent system, the hydraulic fracture network is represented by a mode-1 fracture propagating in a homogeneous medium; and having the same energy released as the fracture propagates to

the same height or length. In the equivalent system, the energy released due to mode-2 propagation of the hydraulic fracture is disregarded: when hydraulic fracture is arrested by a natural fracture and consequently the natural fracture propagates from its ends, if the natural fracture is inclined to the direction of maximum in-situ stress in the plane, the propagation will be mixed mode.

The model development are based on the following assumptions:

Assumption 1: The surface discontinuities do not evolve with the applied loadings. This suggest that there is no need to develop an evolution equation for the damage variable, which is the ratio of the effective surface area of the discontinuities in a representative volume element (RVE) and surface area of the RVE.

Assumption 2: The surface discontinuities are isotopically distributed.

Assumption 3: The rock behaves as a linearly elastic material.

Assumption 4: The natural fractures are filled with a material that also has a linearly elastic response.

The effective stress tensor defined by Kachanov for a material body having empty inclusions is given as

$$\boldsymbol{\sigma}' = \frac{\boldsymbol{\sigma}}{1-\phi} \quad \text{..... (6.20)}$$

But assuming the filling of the discontinuities reduces its effective area relative to the matrix, then, the effective area of the discontinuities is proposed as

$$S_{\phi,e} = S_{\phi}(1-\lambda)^{\beta} \quad \text{..... (6.21)}$$

where λ is the ratio of elastic moduli of the infill material and the matrix, and β is a constant parameter. In a case where the infill material has higher elastic modulus than the matrix, then the overall elastic modulus of the inclusion-matrix system will be higher; a reinforcement of the matrix. But the works by Elselby (1957), Hashin and Shtrikman (1963), Hill (1965), Mori and Tanaka (1973), Willis (1981), Walpole (1981), Weng (1984), and Chen et al. (1992) provide more rigorous studies on the impact of inclusions on the elastic modulus of the host matrix. However, the computation of the effective fracture toughness is demanding (Li and Zhou 2012).

As stated in **Assumption 1**, the damage variable is defined as

$$D = \frac{S_{\phi,e}}{S} = \phi(1-\lambda)^{\beta} \quad \text{..... (6.22)}$$

And using the crack closure method, the energy released in the damaged rock material is equivalent to the energy released in a virgin rock with the normal stress acting on the face of the fracture being the effective stress, i.e.

$$\Pi = 2\int_0^{z_0} \frac{1}{2}\sigma_{yy} u_{yy}\, dz = 2\int_0^{z_0} \frac{1}{2}\sigma'_{yy}\, u'_{yy}\, dz \quad \text{..... (6.23)}$$

Where,

$$u'_{yy} = \frac{\kappa'+1}{4\mu'\pi} K'_{IC} \sqrt{2\pi(z_0 - z)} \quad \text{..... (6.24)}$$

and, $$\sigma'_{yy} = -S'_{h\min} + \frac{K'_{IC}}{\sqrt{2\pi z}} \quad \text{..... (6.25)}$$

$$u_{yy} = \frac{\kappa+1}{4\mu\pi} K_{IC} \sqrt{2\pi(z_0 - z)} \quad \text{..... (6.26)}$$

$$\sigma_{yy} = -S_{h\min} + \frac{K_{IC}}{\sqrt{2\pi z}} \quad \text{..... (6.27)}$$

by substituting equations (6.22)-(6.25) into (6.21), the effective fracture toughness can be determined from the algebraic expression

$$\begin{aligned} &\frac{\kappa'+1}{\mu'} K'_{IC} \left(-\frac{2}{3} S'_{h\min} z_0^{3/2} + \frac{K'_{IC}}{\sqrt{2\pi}} \frac{\pi}{2} z_0 \right) \\ &= \frac{\kappa+1}{\mu} K_{IC} \left(-\frac{2}{3} S_{h\min} z_0^{3/2} + \frac{K_{IC}}{\sqrt{2\pi}} \frac{\pi}{2} z_0 \right) \end{aligned} \quad \text{..... (6.28)}$$

Since damage prior to loading is under consideration and not damage induced by the loading; thus, considering a compression loading of the RVE. The elastic strain energy (compressional loading) and the effective elastic energy are equivalent, i.e.

$$\frac{1}{2} \int_B \boldsymbol{\sigma}\boldsymbol{\varepsilon} \, dv = \frac{1}{2} \int_{B'} \boldsymbol{\sigma}'\boldsymbol{\varepsilon}' \, dv' \quad \text{..... (6.29)}$$

Hence, the relationship between the damaged and virgin shear moduli is

$$\mu = \mu' \left[1 - \phi (1-\lambda)^{\beta} \right]^2 \quad \text{..... (6.30)}$$

The constant parameter, β, can be determined by curve-fitting the effective shear modulus in Eq. 6.30 with Mori-Tanaka's model or from experiment.

When the contributions of the tensile stresses along the fracture edges are disregarded, the damaged fracture toughness of the formation becomes

$$K_{IC} = K'_{IC}\sqrt{1-\phi(1-\lambda)^{\beta}} \quad \text{..... (6.31)}$$

6.3.5 Effective Fracture Toughness for Formations with Ordered Natural Fractures

When the natural fractures are oriented in the same direction, the path of the main hydraulic fracture stem can be easily traced compared to the disordered pattern. In this case the energy released as the fracture propagates in both modes 1 and 2 is

$$\Pi = 2\int_{c}\frac{1}{2}\sigma_{yy}u_{yy}\,ds + \int_{c_2}2N\frac{1}{2}\sigma_{xy}u_{xx}\,ds_2 = 2\int_{0}^{z_0}\frac{1}{2}\sigma'_{yy}\,u'_{yy}\,dz \quad \text{..... (6.32)}$$

Where, c is the path of the main hydraulic fracture, and c_2 is the distance the fracture propagates in mixed mode. N is the number of repeated pattern of the natural fractures; in other words, the number of rows. Eq. (6.32) is derived based on the assumption that the natural fracture will propagate from one of its ends, when it arrests the hydraulic fracture.

$$u_{xx} = \frac{\kappa+1}{4\mu\pi}K_{IIC}\sqrt{2\pi(z_0 - z)} \quad \text{..... (6.33)}$$

$$\sigma_{xy} = \frac{K_{IIC}}{\sqrt{2\pi z}} \quad \text{..... (6.34)}$$

Depending on the projected path, the steps in Section 6.3.4 can be followed in estimating the effective fracture toughness from equation (6.32).

6.4 Numerical Examples

A hydraulic fracture stands in layer 6, with its tips at the top and bottom of the formation, which is 9m (30 ft.) thick. Using the full multi-layer equilibrium height model, the tips displacements at different internal pressures are shown in Figs 6.4, 6.5, and 6.6.

Table 6.1 shows the description of the layers. While the use of the energy-released-based effective fracture toughness for the same range of pressures are shown in Figs. 6.7, 6.8, and 6.9. The equivalent three-layer system, based on equivalent energy release rate hypothesis, (3ER-EHP) to the eleven-layer problem (11-EHP) is shown in **Table 6.2** below.

Layer	**Top** m.	**Thickness** m.	**Stress** MPa	**K_{IC}** $MPa\sqrt{m}$	**E** MPa	**ν** -	**Lithology** -
1	2743.200	152.40	52.30	1.10	29510	0.3	Shale
2	2895.600	30.480	53.99	1.10	29510	0.3	Shale
3	2926.080	4.572	49.02	1.32	29510	0.26	Sand
4	2930.652	15.240	54.50	1.10	29510	0.3	Shale
5	2945.892	3.048	49.34	1.32	29510	0.26	Sand
6	2948.940	9.144	54.79	1.10	29510	0.3	Shale
7	2958.084	3.048	49.54	1.32	29510	0.26	Sand
8	2961.132	4.572	54.97	1.10	29510	0.3	Shale
9	2965.704	3.048	49.67	1.32	29510	0.26	Sand
10	2968.752	30.480	55.35	1.10	29510	0.3	Shale
11	2999.232	152.400	57.05	1.10	29510	0.3	Shale

Table 6.1.Description of the formation properties and in-situ stress profiles for the 11-layer problem.

Layer		**Top** m.	**Thickness** m.	**Stress** MPa	**K_{IC}** $MPa\sqrt{m}$	**E** MPa	**ν** -	**Lithology** -
3	1	2743.200	152.40	52.30	0.672	29510	0.3	Shaly-Sand
	2	2895.600	30.480	53.99	0.672	29510	0.3	Shaly-Sand
	3	2926.080	4.572	49.02	0.672	29510	0.3	Shaly-Sand
	4	2930.652	15.240	54.50	0.672	29510	0.3	Shaly-Sand
	5	2945.892	3.048	49.34	0.672	29510	0.3	Shaly-Sand
2	6	2948.940	9.144	54.79	1.10	29510	0.3	Shale
1	7	2958.084	3.048	49.54	0.676	29510	0.3	Shaly-Sand
	8	2961.132	4.572	54.97	0.676	29510	0.3	Shaly-Sand
	9	2965.704	3.048	49.67	0.676	29510	0.3	Shaly-Sand
	10	2968.752	30.480	55.35	0.676	29510	0.3	Shaly-Sand
	11	2999.232	152.400	57.05	0.676	29510	0.3	Shaly-Sand

Table 6.2.Description of the formation properties and in-situ stress profiles for the equivalent three-layer problem.

Comparing the region maps in Figs. 6.4, 6.5, and 6.6 and Figs. 6.7, 6.8, and 6.9, it is evident that the two solutions are equivalent.

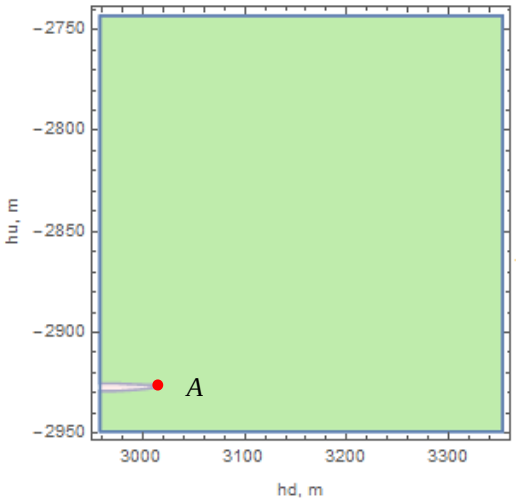

Fig. 6.4. Region map of the tips positions when the pressure inside the fracture is 53.09MPa (7700 psi) for 11-EHP.

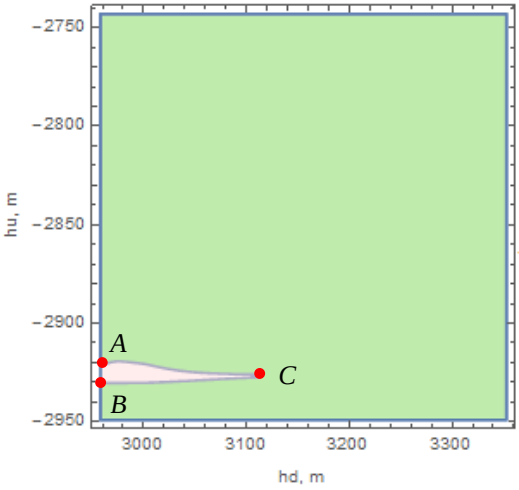

Fig. 6.5. Region map of the tips positions when the pressure inside the fracture is 53.78MPa (7800 psi) for 11-EHP.

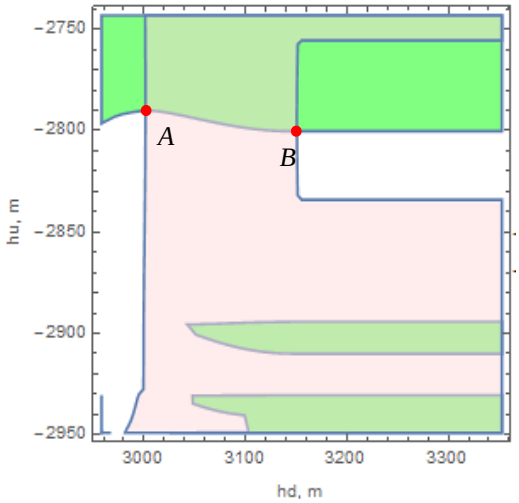

Fig. 6.6. Region map of the tips positions when the pressure inside the fracture is 54.47MPa (7900 psi) for 11-EHP.

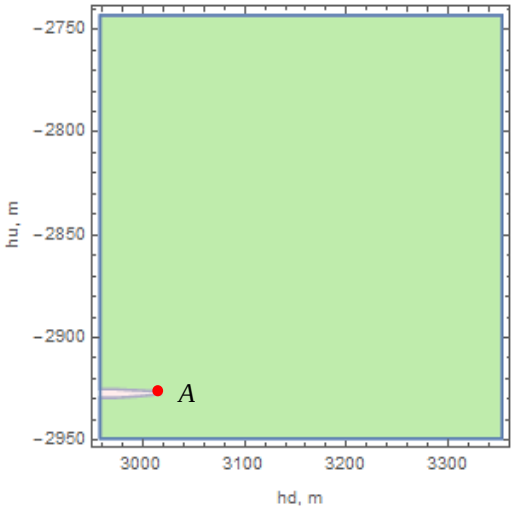

Fig.6.7. Region map of the tips positions when the pressure inside the fracture is 53.09MPa (7700 psi) for 3ER-EHP.

Points A, B, and C in Figs. 6.4, 6.5, 6.7, and 6.8 are not the practical solutions to the nonlinear equation; at these pressure values, the initial upper and lower tips are stable. In Figs. 6.6 and 6.9 Point B is the pair solution to the practical solution A. From the map, the upper tip is located at depth 2790 m, while the lower tip is located at depth 3005 m.

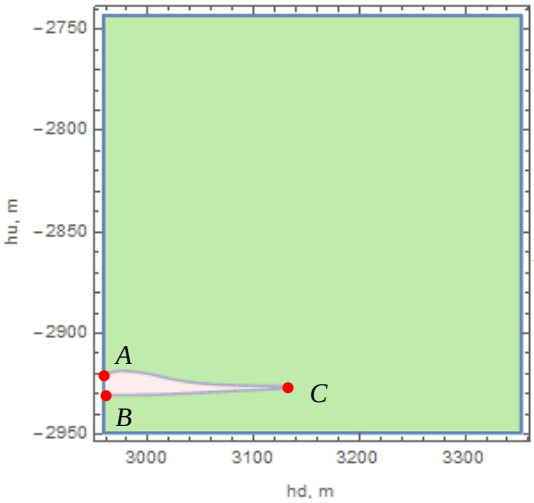

Fig. 6.8. Region map of the tips positions when the pressure inside the fracture is 53.78MPa (7800 psi) for 3ER-EHP.

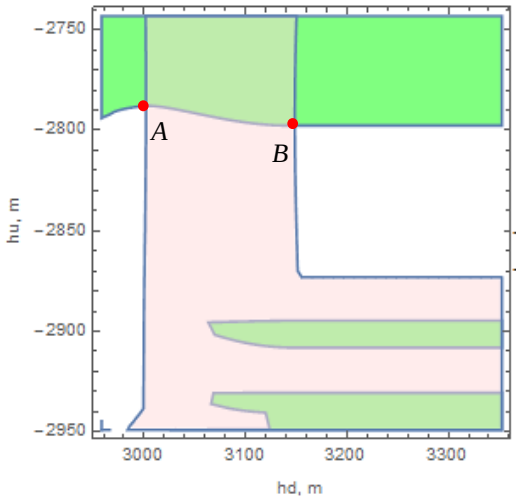

Fig. 6.9. Region map of the tips positions when the pressure inside the fracture is 54.47MPa (7900 psi) for 3ER-EHP.

Using the linear blend rule and weakest link arguments, the effective fracture toughness for the upper and lower barriers are 1.11 MPa and 1.1 MPa respectively. The locations of the tips in these equivalent systems are similar to the 3ER-EHP (Figs. 6.10 and 6.11); for shorthand writing, the equivalent three layer problem based on blend rule is 3BR-EHP, and that based on weakest link arguments is 3WL-EHP. In this case, both 3ER-EHP and 3WL-EHP yielded similar results, while 3BR-EHP and 3ERR-EHP gave more accurate

positions of the tips relative to the other homogenization methods (Figs. 6.12, 6.13, 6.14, 6.15, and 6.16).

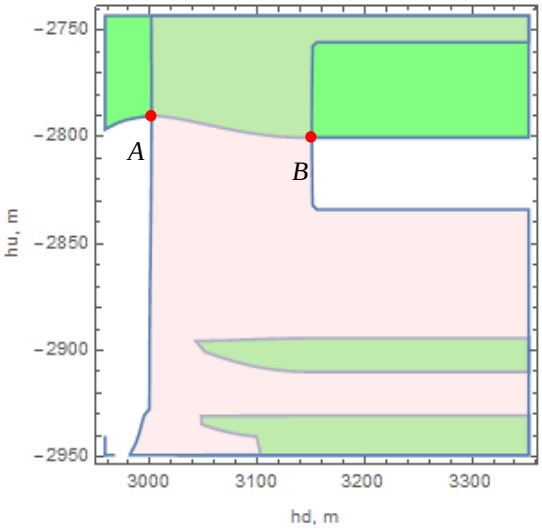

Fig. 6.10. Region map of the tips positions when the pressure inside the fracture is 54.47MPa (7900 psi) for 3BR-EHP.

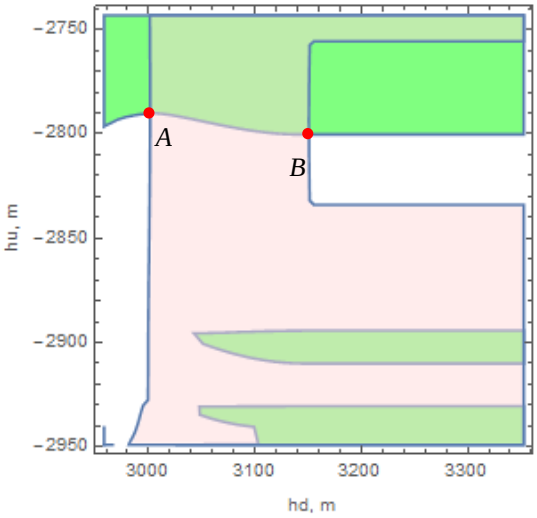

Fig. 6.11. Region map of the tips positions when the pressure inside the fracture is 54.47MPa (7900 psi) for 3WL-EHP.

From these examples, it is evident that the use of energy-release rate hypothesis for homogenizing multilayer problems may not be accurate (to a small degree), except when the contributions of the tensile stresses are neglected.

Table 6.3 shows the description of eleven layers with significant modulus contrasts. And the effective fracture toughness for the upper and lower barriers using the equivalent energy release rate hypothesis are 1.44MPa and 1.59 MPa respectively. While the effective fracture toughness for the upper and lower homogenized barriers when using

the linear blend rule are 4.17 MPa and 5.46 MPa respectively; and using the weakest point arguments, the effective fracture toughness are 1.6MPa and 3.28MPa respectively. In the same vein, the effective fracture toughness using the reduced equivalent energy release rate hypothesis (3ERR-EHP) are 3.38MPa and 4.15 MPa respectively.

Alternatively, the use of equivalent strain energy hypothesis, which is mathematically tedious, may be used in lieu of the energy released rate; this comparison will not be pursued in this paper.

Layer	**Top** m.	**Thickness** m.	**Stress** MPa	**K_{IC}** $MPa\sqrt{m}$	**E** MPa	**ν** -	**Lithology** -
1	2743.200	152.40	52.30	5.10	29510	0.3	Shale
2	2895.600	30.480	53.99	1.10	29510	0.3	Sand
3	2926.080	4.572	49.02	3.32	29510	0.26	Shale
4	2930.652	15.240	54.50	1.10	29510	0.3	Shale
5	2945.892	3.048	49.34	5.32	29510	0.26	Shale
6	2948.940	9.144	54.79	1.10	29510	0.3	Shale
7	2958.084	3.048	49.54	6.32	29510	0.26	Sand
8	2961.132	4.572	54.97	2.10	29510	0.3	Shale
9	2965.704	3.048	49.67	1.32	29510	0.26	Sand
10	2968.752	30.480	55.35	3.10	29510	0.3	Shale
11	2999.232	152.400	57.05	6.10	29510	0.3	Shale

Table 6.3. Description of the formation properties and in-situ stress profiles for the 11-EHP, Case 2.

The tensile stress is greatest at the tips of the fracture, and reduces along the length of the fracture. Along the edges of the fracture, away from the tips, the Irwin criterion, $K_I = K_{IC}$, does not apply; but $K_I < K_{IC}$. Thus, neglecting the tensile stress contribution in the crack closure energy function will yield more accurate results; and this is evident

in the two example cases.

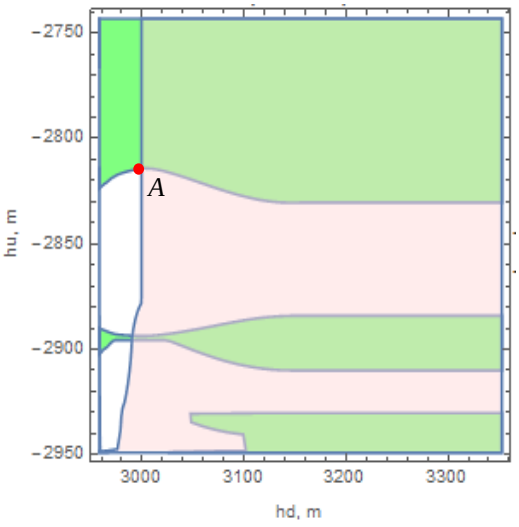

Fig. 6.12. Region map of the tips positions when the pressure inside the fracture is 54.47MPa (7900 psi) for 11-EHP, Case 2.

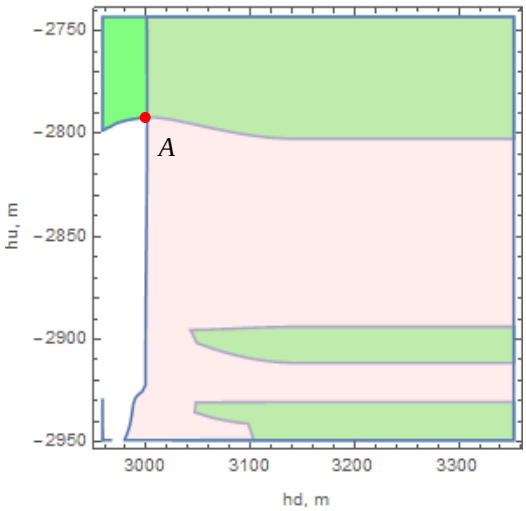

Fig. 6.13. Region map of the tips positions when the pressure inside the fracture is 54.47MPa (7900 psi) for 3ER-EHP, Case 2.

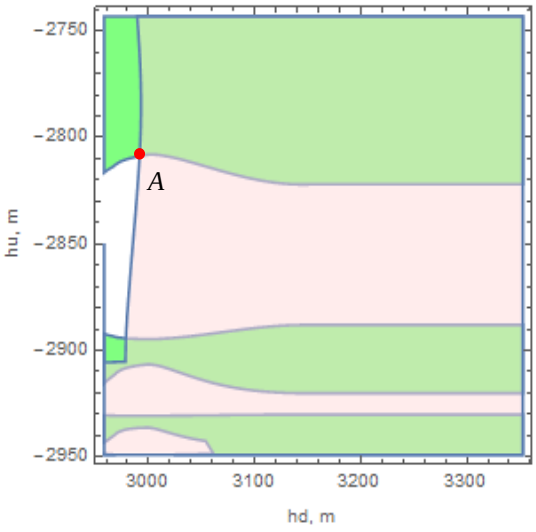

Fig. 6.14. Region map of the tips positions when the pressure inside the fracture is 54.47MPa (7900 psi) for 3BR-EHP, Case 2.

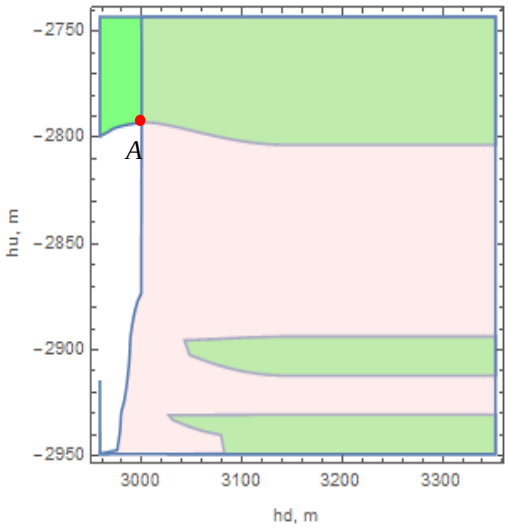

Fig. 6.15. Region map of the tips positions when the pressure inside the fracture is 54.47MPa (7900 psi) for 3WL-EHP, Case 2.

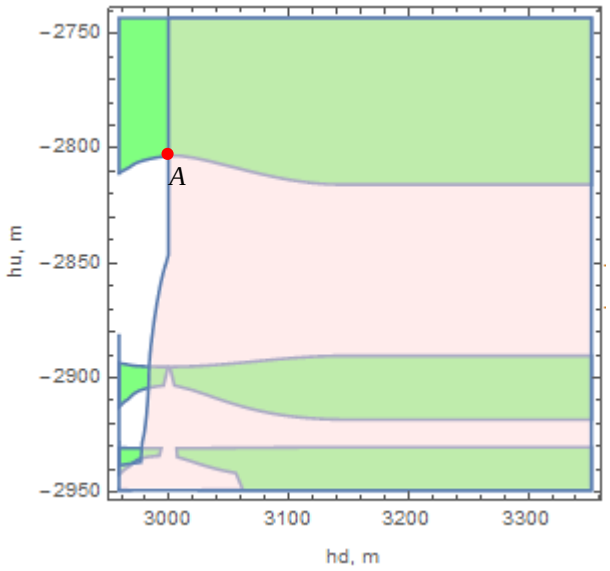

Fig.6.16. Region map of the tips positions when the pressure inside the fracture is 54.47MPa (7900 psi) for 3EER-EHP, Case 2.

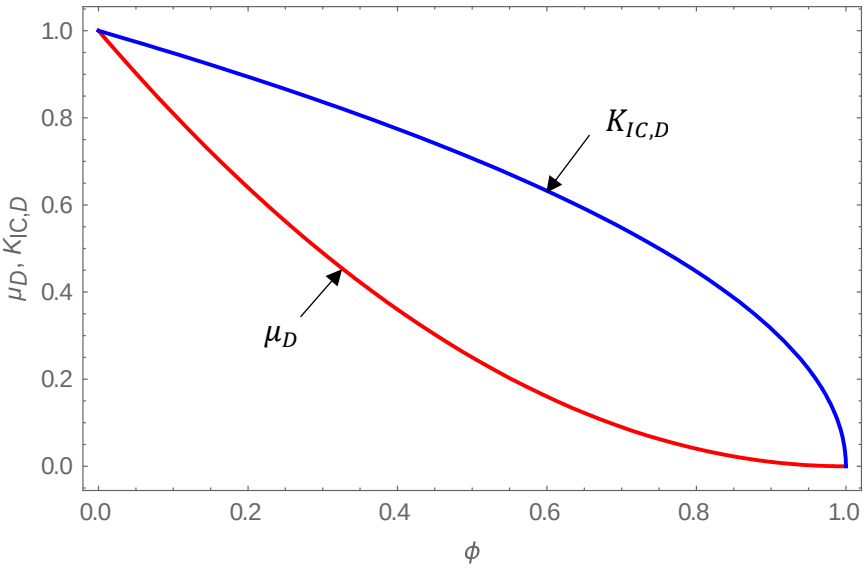

Fig. 6.17. Variations of the normalized shear modulus, μ_D, and normalized fracture toughness with damage in any material displaying a linear elastic response. $\lambda = 0$ in this case.

Fig. 6.17 shows that the impact of damage on the elastic properties of the formation matrix do not follow the same path. The Young's and shear moduli are more severely damaged than the fracture toughness. And based on isotropic damage assumption, the Poisson ratio will not be affected by the presence of the discontinuities (damage), based on the continuum damage theory; the impact of damage on other elastic properties are beyond the scope of this article. And Figs. 6.18a and 6.18b, show the variations of the effective shear modulus and fracture toughness when the discontinuities (inclusions, or natural fractures) are filled with material having lower or higher Young's modulus.

To compare the predictions of the proposed effective shear modulus for the damaged/reinforced material with Mori-Tanaka's model, Table 6.4 shows the three cases:

Case	**Matrix Young's Mod.** GPa.	**Infill Young's Mod.** GPa	**Matrix Poisson Ratio** --	**Infill Poisson Ratio** --
1	29.5	0	0.3	0
2	29.5	5.0	0.3	0.33
3	20.0	25.0	0.26	0.25

Table 6.4. Elastic Properties of the Matrix and Inclusions.

As observed in Fig.6. 19a, the prediction from the proposed phenomenological model mimics the rigorous Mori-Tanaka model. In the second and third cases, the values of β are 2.5 and 1.2 respectively.

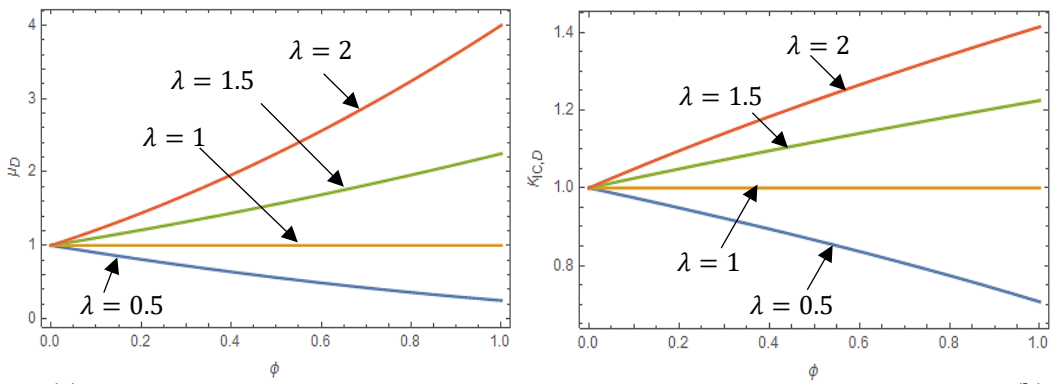

Fig. 6.18. (a) Variation of the normalized shear modulus, μ_D, considering different infill materials (b) Variation of normalized fracture toughness, $K_{IC,D}$, with damage considering different infill materials.

6.5 Summary

Using equivalent energy release-rate hypothesis, an effective fracture toughness was derived to homogenize heterogeneous layered media. Homogenizing heterogeneous layered media into a single layer can reduce multi-layer equilibrium-height problem to the classical three-layer equilibrium-height problem. And the reduction of the multi-layer problem to the classical three-layer problem reduces the model complexity. The predictions from the proposed model have the same range of accuracy as the well-known linear blend rule; while the predictions from the weakest link arguments method were also observed to be inaccurate.

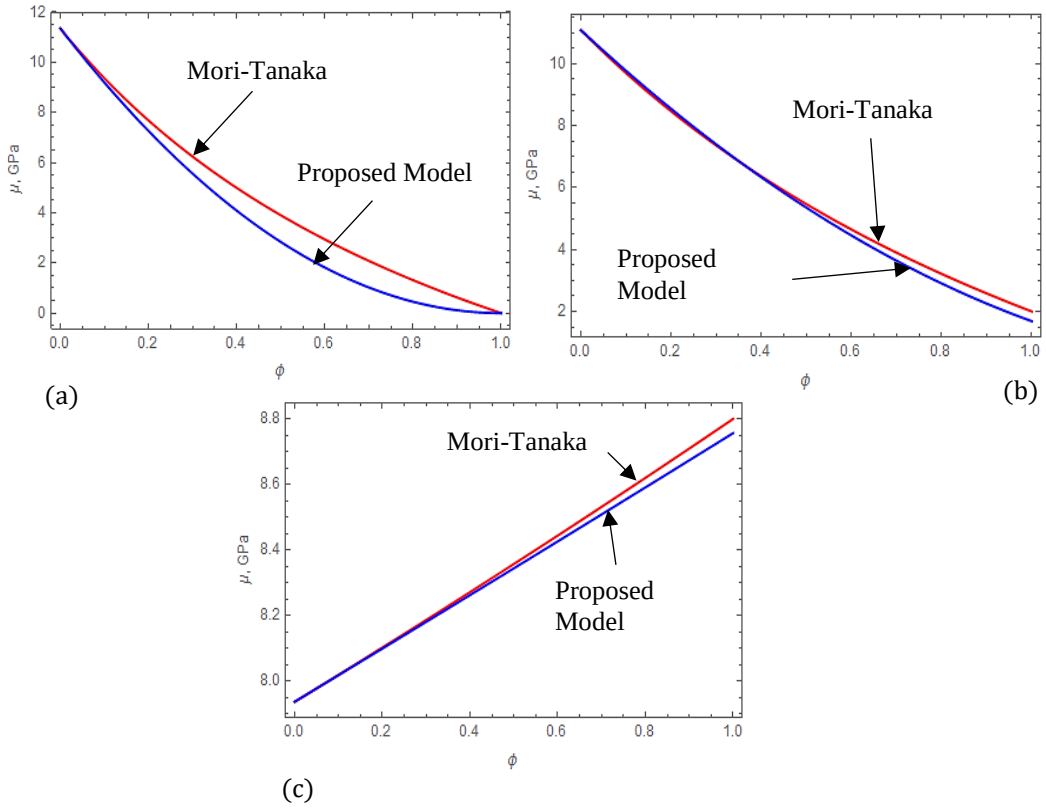

Fig. 6.19. Comparing the performance of the proposed model for effective shear modulus of a material body having (a) empty or open natural fractures, Case 1, (b) micro-fractures filled with lower modulus material, Case 2, and (c) micro-fractures filled with higher modulus material, Case 3.

Furthermore, an effective fracture toughness formulation for predicting the growth of hydraulic fracture in a formation with micro-cracks or any other form of ordered or disordered inclusions was developed. The formulation is based on the use of damage theory, equivalent energy-release rate, and equivalent strain-energy hypotheses.

The presence of infill materials in the micro-cracks (closed natural fractures) will affect the overall elastic properties of the damaged/reinforced rock-fracture system. And using a phenomenological approach, which is based on the use of an effective area, the

proposed model performs very well as the rigorous Mori-Tanaka model, when the fractures are open.Then using the Mori-Tanaka model for the effective shear modulus, as reference, the constant parameter in the proposed model can be determined; subsequently, estimating the effective fracture toughness for the rock-closed fracture system. The benefit of the proposed model over the Mori-Tanaka is its simplicity in computing the effective fracture toughness.

7. CONCLUSIONS AND FUTURE WORKS

The main objectives of this work are to develop the hydromechanical frameworks for predicting the potential for self-killing of oil and gas wells, and a quick model for determining the hydraulic fracture containment potential in heterogeneous media. Thus, the two main sources of sand production, wellbore breakout and erosion, are treated in this study. Also, a thermodynamically consistent phase-field model is developed to rigorously predict the hydrodynamics of gas-liquid-solid flow in the wellbore. Furthermore, using equivalent energy released rate hypothesis alongside continuum damage theory, an effective fracture toughness model for predicting fracture containment potential in heterogeneous media is proposed.

7.1 Wellbore Breakout Mechanisms

The following conclusions are drawn from the study on shear failure and extensile splitting/cracking in rocks:

- When the wellbore orientation is not aligned in the directions of the in-situ principal stresses, the direction of the first breakout episode is not parallel to the minimum in-situ horizontal stress; the breakout angle significantly depends on the well deviation and azimuthal angles and the depth of burial. For subsequent breakout episodes, the breakout angle tends to turn in the direction of the minimum horizontal in-situ stress.
- For the first time a theoretical framework for predicting the morphology of toroidal breakout is proposed in this work. In a homogeneous formation, the fracture angles

are the same for both propagating shear fractures, and the two failure lines will definitely meet at the center. When the formation is heterogeneous, the intersecting location depends greatly on the degree of vertical heterogeneity layout of the formation. If the upper layer is "softer" than the lower layer, the shear fracture lines will intersect at the upper layer. And if the layout is reversed, the two lines will intersect at the lower layer; in a nutshell, irrespective of the layout, the two lines will intersect in the softer layer. Knowing the breakout azimuth and location of the intersection of the projected shear fractures, the breakout volume can be approximately determined; this approach saves a lot of computation efforts.

- The size of splinter/caving produced during breakout significantly depends on the prevailing in-situ stress loadings, the initial damage distribution around the borehole, the mechanical properties of the rock, the geometry of the borehole, and a necessary condition for unstable crack growth around the borehole. As the radial or back stress acting on the representative microcrack increases, the potential for caving generation reduces; hence this is one of the reasons wellbore breakout is not a continuous process. The unstable crack growth phase is independent of the stress changes around the borehole, but as the length of the slender rock layer reaches a limiting buckling length the breakout episode ends as the slender rock layer buckles. Assuming all parameters are same, except plane strain modulus, breakout width in sandstone is expected to be wider than shale, since caving size increases with the plain strain modulus of the rock when other parameters are kept constant. More so, higher in-situ stress magnitude reduces the size of caving. It

thus implies that larger splinter/ boulder will be produced at shallow depth than in deep formations. Another consequence of higher hoops stress distribution around the borehole is that large cavings will be produced in a vertical well than in a horizontal well, when the in-situ stress loadings are same in the two well profiles. Hence, it can be inferred that under same in-situ stress loading, pressure and velocity distributions in the wellbore, a vertical well may likely bridge than a horizontal well. But this inference is dependent on the failure potential around the wellbore, since a horizontal wellbore has higher potential to fail than a vertical well.

- In addition, the broader the initial damage around the wellbore is the less likely the formation of splinter/caving because the standing crack at the mid-point of the damaged zone (average representation of the damaged zone) experiences higher back stress as its distance to the boundary increases. But once the unstable crack-growth phase can be reached, the breakout width will be wider as the initial damaged zone is broader.
- Furthermore, the geometry of the wellbore has significant impact on the size of the splinter to be produced. As the wellbore becomes more elliptic the limiting buckling length of the slender rock layer reduces. This suggests that peradventure when the unstable crack growth phase is reached around a typical elliptic wellbore, the size of the splinter produced will be smaller to that produced from a circular wellbore.

7.2 Erosion

An energy-consistent erosion constitutive relation for deformable porous medium is proposed. The model reveals the weakness of the well-known phenomenological model when the pressure gradient in the producing formation is not steep towards the wellbore. For axial erosion around the wellbore, the momentum transport by viscous effects on the porous layers can unseat the grains of the matrix. While a radial erosion in the producing formation occurs, when the sum of both the viscous stress and pressure difference across the grains (seepage forces) exceeds the critical hydraulic gradient. For competent formation, higher hydraulic gradient will be required to break the bonds between the particles; this is unlikely in most cases. It thus suggests that erosion will occur in weakly-cemented and unconsolidated formations. By inspection of the derived conceptual model, the following observations are restated:

- Prior to significant erosion of the matrix, the sand-rate increases with the same profile as the fluid velocity; this is the transient state of the sand production process.
- As sand production increases, the formation will respond by compacting.
- The compaction of the eroding formation reduces the erosion rate, $\det(\mathbf{F}) < 1$, and also the rate of compaction further influences the reduction in erosion rate.
- For constant fluid flux (which is not realistic in long eroding-reservoir in the field), the mass rate has a relatively linear relationship with the fluid-flux. This linear relationship is projected to occur when the erosion front is thin (a sharp interface).

- The increment in sand rate with applied stress is assumed to be link to significant second-order effects, which reduce the critical hydraulic gradient and increase permeability to flow. Consequently, increasing the resultant hydraulic gradient (this is a non-linear coupling as observed in experiments by Papamichos, 2010).

7.3 Thermodynamically Consistent Multiphase-Field Modeling of Gas-Liquid-Solid Flow

A thermodynamically consistent multiphase-field model is developed for the flow of gas, liquid, and cavings mixture in the wellbore. The internal workings due to the internal configurational force system in the bulk of each phase are incorporated into the model. Using Coleman-Noll entropy principle to place restrictions on the proposed response functions, which are defined to obey Truesdell principle of equipresence, it is derived that the mixture stress tensor is a function of effective viscosity of the mixture, temperature gradient, and mass concentration gradients of each species of the mixture. The additional stress due to concentration gradient mimics surface tension, while the additional stress due to temperature gradient is another non-local constitutive behavior of the mixture due to a non-isothermal transport process.

7.4 Quick Method for Predicting Fracture Broaching

Using equivalent energy release-rate hypothesis, an effective fracture toughness was derived to homogenize heterogeneous layered media. Homogenizing heterogeneous layered media into a single layer can reduce multi-layer equilibrium-height problem to the classical three-layer equilibrium-height problem. And the reduction of the multi-layer problem to the classical three-layer problem reduces the model complexity. The

predictions from the proposed model have the same range of accuracy as the well-known linear blend rule; while the predictions from the weakest link arguments method were also observed to be inaccurate.

Furthermore, an effective fracture toughness formulation for predicting the growth of hydraulic fracture in a formation with micro-cracks or any other form of ordered or disordered inclusions was developed. The formulation is based on the use of damage theory, equivalent energy-release rate, and equivalent strain-energy hypotheses. The presence of infill materials in the micro-cracks (closed natural fractures) will affect the overall elastic properties of the damaged/reinforced rock-fracture system. And using a phenomenological approach, which is based on the use of an effective area, the proposed model performs very well as the rigorous Mori-Tanaka model, when the fractures are open. Then using the Mori-Tanaka model for the effective shear modulus, as reference, the constant parameter in the proposed model can be determined; subsequently, estimating the effective fracture toughness for the rock-closed fracture system. The benefit of the proposed model over the Mori-Tanaka is its simplicity in computing the effective fracture toughness.

7.5 Future Works

This study is relatively new in petroleum geomechanics, hence further studies are needed to better understand the self-killing phenomenon. Some of these works include:

- A numerical implementation of the multiphase-field model for flow of gas, liquid, and cavings in the wellbore.
- The impact of in-hole tubular on self-killing potential.

- Coupling all the multiphysics, erosion, wellbore breakout, wellbore hydrodynamics, and reservoir compaction into a single functioning simulator.
- The impact of fluid flow stresses on the size of caving.
- The influence of casing setting depth on wellbore bridging.
- Complete well-bridging analysis. As the cavings settle in the wellbore, due to partial bridging criterion, what will be the packing distribution that will consequently stanch the flow?

NOMENCLATURE

D	damage variable
G_{I+}	energy release rate in upper barriers
G_{I-}	energy release rate in lower barriers
h_u	displacement of the upper tip
h_d	displacement of the lower tip
K_{I+}	stress intensity factor at upper tip
K_{I-}	stress intensity factor at lower tip
$\overline{K}_{IC}^{+}$	effective fracture toughness for upper homogenized upper barriers
$\overline{K}_{IC}^{-}$	effective fracture toughness for homogenized lower barriers
P_{FU}	minimum fracture extension pressure for upper tip
P_{FD}	minimum fracture extension pressure for lower tip

$S_{h,min}$	minimum horizontal in-situ stress
${u_{yy}}^{+}$	fracture half width in the upper barriers
${u_{yy}}^{-}$	fracture half width in the lower barriers
μ_n	formation, *n*, shear modulus
$\overline{\mu}_u$	Averaged shear modulus for upper barriers
$\overline{\mu}_d$	Averaged shear modulus for lower barriers
λ	ratio of inclusion and undamaged matrix elastic moduli
ϕ	Ratio of the surface area of discontinuity to surface area of representative volume element
C_0	Cohesion of Rock
T	Temperature
$\boldsymbol{T}$	Cauhcy stress
$\boldsymbol{S}$	First Piola-Kirchhoff stress tensor

θ_B, ς_B	Breakout width
r_{bk}	Breakout depth
p_w	Wellbore pressure
p_0	Formation pressure
σ_v	Vertical stress or overburden stress
S_H, σ_H	Maximum horizontal in-situ stress
S_h, σ_h	Minimum horizontal in-situ stress
$\sigma_{\theta\theta}$	Hoops stress
σ_{rr}	Radial stress
S	Strain energy density factor
F	Wedging force driving the micro crack
l	Micro crack half length
$d\psi$	Volumetric strain due to mechanical loading
E	Young's Modulus
L_B	Caving width
t_B	Caving height

p_c	Critical erosion pressure
$\boldsymbol{D}^f$	Symmetric velocity gradient tensor of fluid
$\boldsymbol{Q}$	Rotation tensor
v_s	Velocity of grains
$\boldsymbol{F}$	Deformation gradient
$\boldsymbol{L}$	Velocity gradient
N_c	Coordination number of packed rock grains
A_c	Area of contact of packed grains
k	permeability

REFERENCES

Adachi, J.I., Detournay, E. and Peirce, A.P., 2010. Analysis of the classical pseudo-3D model for hydraulic fracture with equilibrium height growth across stress barriers. International Journal of Rock Mechanics and Mining Sciences, 47(4), pp.625-639.

Adhikary, D.P. and Dyskin, A.V., 1998. A continuum model of layered rock masses with non-associative joint plasticity. International Journal for Numerical and Analytical Methods in Geomechanics, 22(4), pp.245-261.

Advani, S.H., Lee, T.S. and Lee, J.K., 1990. Three-dimensional modeling of hydraulic fractures in layered media: part I—finite element formulations. Journal of Energy Resources Technology, 112(1), pp.1-9.

Ahmed, U., 1984, January. A Practical Hydraulic Fracturing Model Simulating Necessary Fracture Geometry, Fluid Flow and Leakoff, and Proppant Transport. In SPE Unconventional Gas Recovery Symposium. Society of Petroleum Engineers.

Akbarnejad-Nesheli, B. and Schubert, J.J., 2006, January. Effect of Water Depth on Bridging Tendencies in Ultradeepwater Blowouts in Gulf of Mexico. In SPE Annual Technical Conference and Exhibition. Society of Petroleum Engineers.

Anderson, D.M., McFadden, G.B. and Wheeler, A.A., 1998. Diffuse-interface methods in fluid mechanics. Annual review of fluid mechanics, 30(1), pp.139-165.

Anderson, T.B. and Jackson, R., 1967. Fluid mechanical description of fluidized beds. Equations of motion. Industrial & Engineering Chemistry Fundamentals, 6(4), pp.527-539.

Antanovskii, L.K., 1994. Quasi-steady deformation of a two-dimensional bubble placed within a potential viscous flow. Meccanica, 29(1), pp.27-42.

Atkins, A.G. and Mai, Y.W., 1985. Elastic and plastic fracture: metals, polymers, ceramics, composites, biological materials. Ellis Horwood; Halsted Press, Toronto, England.

Atkins, A.G., 1979. Cracking of Layered Structures: the Suppression of Yielding by Cast Hardening. Mechanical Behavior of Materials, Vol. 3, pp.341-349.

Badalassi, V.E., Ceniceros, H.D. and Banerjee, S., 2003. Computation of multiphase systems with phase field models. Journal of Computational Physics, 190(2), pp.371-397.

Balzer, G. and Simonin, O. 1993. Extention of eulerian gas–solid flow modelling to dense fluidized bed, in: P. Viollet (Ed.), Proceedings of the 5th International Symposium on Refined Flow Modelling and Turbulence Measurements, France, Paris, pp. 417–424.

Balzer, G., Simonin, O., Boelle, A. and Lavieville, J., 1996. A unifying modelling approach for the numerical prediction of dilute and dense gas-solid two phase flow. Proceeding of 5th International Conference on Circulating Fluidized beds, May, Beijing, China.

Barrett J.W. and Blowey J.F., 1999a. Finite element approximation of a model for phase separation of a multicomponent alloy with nonsmooth free energy and a concentration dependent mobility matrix, Math. Models Methods Appl. Sci., 9.

Barrett, J.W. and Blowey, J.F., 1996. An error bound for the finite element approximation of a model for phase separation of a multi-component alloy. IMA Journal of Numerical Analysis, 16(2), pp.257-287.

Barrett, J.W. and Blowey, J.F., 1999b. An improved error bound for a finite element approximation of a model for phase separation of a multi-component alloy. IMA Journal of Numerical Analysis, 19(1), pp.147-168.

Barrett, J.W. and Blowey, J.F., 2001. An improved error bound for a finite element approximation of a model for phase separation of a multi-component alloy with a concentration dependent mobility matrix. Numerische Mathematik, 88(2), pp.255-297.

Beremin, F.M., Pineau, A., Mudry, F., Devaux, J.C., D'Escatha, Y. and Ledermann, P., 1983. A local criterion for cleavage fracture of a nuclear pressure vessel steel. Metallurgical transactions A, 14(11), pp.2277-2287.

Besson, J., 1990. Performance of slanted and horizontal wells on an anisotropic medium. In European Petroleum Conference. Society of Petroleum Engineers.

Blowey, J.F., Copetti, M.I.M. and Elliott, C.M., 1996. Numerical analysis of a model for phase separation of a multicomponent alloy. IMA Journal of Numerical Analysis, 16(1), pp.111-139.

Bogdanov, I., Jardel, S., Turki, A. and Kamp, A., 2010. Pore scale phase field model of two phase flow in porous medium. In Annual COMSOL Conference, Paris, France.

Brace, W.D. and Bombolakis, E.G., 1963. A note on brittle crack growth in compression. Journal of Geophysical Research, 68(12), pp.3709-3713.

Brace, W.F., Paulding, B.W. and Scholz, C.H., 1966. Dilatancy in the fracture of crystalline rocks. Journal of Geophysical Research, 71(16), pp.3939-3953.

Bratli, R.K. and Risnes, R., 1981. Stability and failure of sand arches. Society of Petroleum Engineers Journal, 21(02), pp.236-248.

Brinkman, H.C., 1949. A calculation of the viscous force exerted by a flowing fluid on a dense swarm of particles. Flow, Turbulence and Combustion, 1(1), p.27.

Broek D .1991, Elementary Engineering Fracture Mechanics, 4th Revised Edition, Kluwer Academic Publishers, Dordrecht, Netherlands.

Bui, H.D., 1977. An integral equations method for solving the problem of a plane crack of arbitrary shape. Journal of the Mechanics and Physics of Solids, 25(1), pp.29-39.

Burton, C.V., 1892. XVIII. A theory concerning the constitution of matter. The London, Edinburgh, and Dublin Philosophical Magazine and Journal of Science, 33(201), pp.191-204.

Cahn, J.W. and Hilliard, J.E., 1958. Free energy of a nonuniform system. I. Interfacial free energy. The Journal of chemical physics, 28(2), pp.258-267.

Cahn, J.W. and Hilliard, J.E., 1959. Free Energy of a Nonuniform System. III. Nucleation in a Two-Component Incompressible Fluid. The Journal of Chemical Physics, 31(3), pp.688-699.

Catherine, C.S., Carius, H. and Fant, M.D., 1995. Cleavage toughness of heterogeneous materials and application to welded joints. Fatigue & Fracture of Engineering Materials & Structures, 18(5), pp.597-604.

Ceniceros, H.D., 2003. The effects of surfactants on the formation and evolution of capillary waves. Physics of Fluids, 15(1), pp.245-256.

Chaboche, J.L., 1981. Continuous damage mechanics—a tool to describe phenomena before crack initiation. Nuclear Engineering and Design, 64(2), pp.233-247.

Chaboche, J.L., 1988. Continuum damage mechanics part 1 and part 2 Journal of Applied Mechanics, Vol. 55, pp.59-72.

Chaboche, J.L., 1979. The Concept of Effective Stress Applied Elasticity and to Viscoplasticity in Presence of Anisotropic Damage. Mechanical behavior of anisotropic solids, pp.737-760.

Cheatham, J.B., 1993, December. A new hypothesis to explain stability of borehole breakouts. In International journal of rock mechanics and mining sciences & geomechanics abstracts (Vol. 30, No. 7, pp. 1095-1101). Pergamon.

Chen, T., Dvorak, G.J. and Benveniste, Y., 1992. Mori-Tanaka estimates of the overall elastic moduli of certain composite materials. Journal of applied mechanics, 59(3), pp.539-546.

Chow, C.L. and Wang, J., 1987. An anisotropic theory of continuum damage mechanics for ductile fracture. Engineering Fracture Mechanics, 27(5), pp.547-558.

Chuprakov, D., Melchaeva, O. and Prioul, R., 2014. Injection-sensitive mechanics of hydraulic fracture interaction with discontinuities. Rock Mechanics and Rock Engineering, 47(5), pp.1625-1640.

Clifton, R.J. and Abou-Sayed, A.S., 1979, January. On the computation of the three-dimensional geometry of hydraulic fractures. In Symposium on Low Permeability Gas Reservoirs. Society of Petroleum Engineers.

Clifton, R.J. and Abou-Sayed, A.S., 1981, January. A variational approach to the prediction of the three-dimensional geometry of hydraulic fractures. In SPE/DOE Low Permeability Gas Reservoirs Symposium. Society of Petroleum Engineers.

Copetti, M.I.M., 2000. Numerical experiments of phase separation in ternary mixtures. Mathematics and computers in simulation, 52(1), pp.41-51.

Cundall, PA and Strack, OD, 1979. A discrete numerical model for granular assemblies. Geotechnical, 29 (1), pp.47-65.

Dahi-Taleghani, A. and Olson, J.E., 2011. Numerical modeling of multistranded-hydraulic-fracture propagation: Accounting for the interaction between induced and natural fractures. SPE journal, 16(03), pp.575-581.

Dananberger E.P., 1993, Outer Continental Shelf Drilling Blowouts, 1971-1991, paper OTC 7248, presented at the 25th annual OTC, Houston, TX, USA.

Davidson, J.F., D., Harrison. 1963. Fluidized Particles, Cambridge University. Press, Cambridge, England.

Detournay, E., 1986. An approximate statical solution of the elastoplastic interface for the problem of Galin with a cohesive-frictional material. International journal of solids and structures, 22(12), pp.1435-1454.

Di Renzo, A. and Di Maio, F.P., 2004. Comparison of contact-force models for the simulation of collisions in DEM-based granular flow codes. Chemical engineering science, 59(3), pp.525-541.

Ding, J. and Gidaspow, D., 1990. A bubbling fluidization model using kinetic theory of granular flow. AIChE journal, 36(4), pp.523-538.

Ding, J. and Lyczkowski, R.W., 1992. Three-dimensional kinetic theory modeling of hydrodynamics and erosion in fluidized beds. Powder Technology, 73(2), pp.127-138.

Drumright-Clarke, M.A. and Renardy, Y., 2004. The effect of insoluble surfactant at dilute concentration on drop breakup under shear with inertia. Physics of fluids, 16(1), pp.14-21.

Dyskin, A.V., Germanovich, L.N. and Salganik, R.L., 1991, January. A mechanism of deformation and fracture of brittle rocks. In The 32nd US Symposium on Rock Mechanics (USRMS). American Rock Mechanics Association.

Dyskin, A.V., Germanovich, L.N. and Ustinov, K.B., 1999. A 3-D model of wing crack growth and interaction. Engineering Fracture Mechanics, 63(1), pp.81-110.

Earlougher, R.C., 1977. Advances in well test analysis. Henry L. Doherty Memorial Fund of AIME.

Economides, M.J. ed., 2000. Reservoir stimulation (Vol. 18). Chichester, England: Wiley.

Eggleton, C.D., Tsai, T.M. and Stebe, K.J., 2001. Tip streaming from a drop in the presence of surfactants. Physical review letters, 87(4), p.048302.

Einstein, H. A.: 1937, Der Geschiebetrieb als wahrschein- lichkeits Problem, Mitt. d. Versuchsanstaltf Wasserbau, Eidg. T. H., Zurich.

Enwald, H., Peirano, E. and Almstedt, A.E., 1996. Eulerian two-phase flow theory applied to fluidization. International Journal of Multiphase Flow, 22, pp.21-66

Eriksson, K. and Atkins, A.G., 1995. The effective through crack fracture toughness of structural components of older inhomogeneous steels. Materials Ageing and Component Life Extension, Warrington, UK, Vol. 1, pp.147-154.

Eriksson, K., 1998. The effective fracture toughness of structural components obtained with the blend rule. Nuclear engineering and design, 182(2), pp.123-129.

Eshelby, J.D., 1951. The force on an elastic singularity. Philosophical Transactions of the Royal Society of London A: Mathematical, Physical and Engineering Sciences, 244(877), pp.87-112.

Eshelby, J.D., 1957, August. The determination of the elastic field of an ellipsoidal inclusion, and related problems. In Proceedings of the Royal Society of London A: Mathematical, Physical and Engineering Sciences (Vol. 241, No. 1226, pp. 376-396). The Royal Society.

Eshelby, J.D., 1970. The Energy Momentum Tensor in Continuum Mechanics, Inelastic Behavior of Solids, ed., Kanninen, MF, et al. McGraw-Hill, New York.

Eshelby, J.D., 1975. The elastic energy-momentum tensor. Journal of Elasticity, 5(3-4), pp.321-335.

Ewy, R.T. and Cook, N.G.W., 1990, October. Deformation and fracture around cylindrical openings in rock—II. Initiation, growth and interaction of fractures. In International Journal of Rock Mechanics and Mining Sciences & Geomechanics Abstracts (Vol. 27, No. 5, pp. 409-427). Pergamon.

Ewy, R.T. and Cook, N.G.W., 1990, October. Deformation and fracture around cylindrical openings in rock—II. Initiation, growth and interaction of fractures. In International Journal of Rock Mechanics and Mining Sciences & Geomechanics Abstracts (Vol. 27, No. 5, pp. 409-427). Pergamon.

Ewy, R.T., Cook, N.G. and Myer, L.R., 1988, January. Hollow cylinder tests for studying fracture around underground openings. In The 29th US Symposium on Rock Mechanics (USRMS). American Rock Mechanics Association.

Eyre, D.J., 1993. Systems of Cahn–Hilliard equations. SIAM Journal on Applied Mathematics, 53(6), pp.1686-1712.

Fairhurst, C. and Cook, N.G.W., 1966, September. The phenomenon of rock splitting parallel to the direction of maximum compression in the neighborhood of a surface. In Proceedings of the first congress on the international society of rock mechanics (Vol. 1, pp. 687-692).

Fairhurst, C. and Cook, N.G.W., 1966, September. The phenomenon of rock splitting parallel to the direction of maximum compression in the neighborhood of a surface. In Proceedings of the First Congress of the International Society of Rock Mechanics, Lisbon (Vol. 25, pp. 687-692).

Falk, F. and Konopka, P., 1990. Three-dimensional Landau theory describing the martensitic phase transformation of shape-memory alloys. Journal of Physics: Condensed Matter, 2(1), p.61.

Falk, F., 1980. Model free energy, mechanics, and thermodynamics of shape memory alloys. Acta Metallurgica, 28(12), pp.1773-1780.

Falk, F., 1983. Ginzburg-Landau theory of static domain walls in shape-memory alloys. Zeitschrift für Physik B Condensed Matter, 51(2), pp.177-185.

Freij-Ayoub, R., 1989. The dipole asymptotic solution for two parallel periodical arrays of cracks. International journal of fracture, 80(2), pp.R43-R48.

Freudenthal, A.M. and Geiringer, H., 1958. The mathematical theories of the inelastic continuum. In Elasticity and Plasticity/Elastizität und Plastizität (pp. 229-433). Springer, Berlin Heidelberg.

Freudenthal, A.M., 1975. Constitutive Equations of Rock with Shear Dilatancy, AROD Report, George Washington. University, Washington, DC.

Fried, E. and Gurtin, M.E., 1993. Continuum theory of thermally induced phase transitions based on an order parameter. Physica D: Nonlinear Phenomena, 68(3-4), pp.326-343.

Fung, R.L., Vilayakumar, S. and Cormack, D.E., 1987. Calculation of vertical fracture containment in layered formations. SPE formation evaluation, 2(04), pp.518-522.

Gao, H. and Rice, J.R., 1989. A first-order perturbation analysis of crack trapping by arrays of obstacles. Journal of Applied Mechanics, 56(4), pp.828-836.

Garcke, H., Nestler, B. and Stoth, B., 1999. A multiphase field concept: numerical simulations of moving phase boundaries and multiple junctions. SIAM Journal on Applied Mathematics, 60(1), pp.295-315.

Garg, S.K. and Pritchett, J.W., 1975. Dynamics of gas-fluidized beds. Journal of Applied Physics, 46(10), pp.4493-4500.

Germanovich, L.N. and Dyskin, A.V., 2000. Fracture Mechanisms and Instability of Openings in Compression. International Journal of Rock Mechanics and Mining Sciences. Vol 37, pp.263-284.

Germanovich, L.N. and Grekov, M.A., 1998. Influence of free surface. Rock Fracture Thermomechanics, Gordon and Breach Publishers, London, New York.

Germanovich, L.N., 2012, November. Thermal spalling of rock. In International Conference on Fracture 9-Sydney, Australia-1997.

Germanovich, L.N., Roegiers, J.C. and Dyskin, A.V., 1994. A model for borehole breakouts in brittle rocks. In Rock Mechanics in Petroleum Engineering. Society of Petroleum Engineers.

Gidaspow, D. and Ettehadieh, B., 1983. Fluidization in two-dimensional beds with a jet. 2. Hydrodynamic modeling. Industrial & Engineering Chemistry Fundamentals, 22(2), pp.193-201.

Gidaspow, D., 1994. Multiphase flow and fluidization: continuum and kinetic theory descriptions. Academic press. San Diego, California.

Gidaspow, D., Seo, Y.C. and Ettehadieh, B., 1983. Hydrodynamics of fluidization: Experimental and theoretical bubble sizes in a two-dimensional bed with a jet. Chemical Engineering Communications, 22(5-6), pp.253-272.

Gravanis, E., Sarris, E. and Papanastasiou, P., 2016, June. A hydro-mechanical erosion analytical model for sand prediction. In 50th US Rock Mechanics/Geomechanics Symposium. American Rock Mechanics Association.

Griffith, A.A., 1921. The phenomena of rupture and flow in solids. Philosophical transactions of the royal society of London. Series A, containing papers of a mathematical or physical character, 221, pp.163-198.

Gu, H. and Weng, X., 2010, January. Criterion for fractures crossing frictional interfaces at non-orthogonal angles. In 44th US Rock Mechanics Symposium and 5th US-Canada Rock Mechanics Symposium. American Rock Mechanics Association.

Gu, H., Weng, X., Lund, J.B., Mack, M.G., Ganguly, U. and Suarez-Rivera, R., 2012. Hydraulic fracture crossing natural fracture at nonorthogonal angles: a criterion and its validation. SPE Production & Operations, 27(01), pp.20-26.

Guenot, A. and Santarelli, F.J., 1988, January. Borehole stability: a new challenge for an old problem. In The 29th US Symposium on Rock Mechanics (USRMS). American Rock Mechanics Association.

Gurtin, M.E. and Struthers, A., 1990. Multiphase thermomechanics with interfacial structure. Archive for Rational Mechanics and Analysis, 112(2), pp.97-160.

Gurtin, M.E., 2000. On the plasticity of single crystals: free energy, microforces, plastic-strain gradients. Journal of the Mechanics and Physics of Solids, 48(5), pp.989-1036.

Handin, J., Hager Jr, R.V., Friedman, M. and Feather, J.N., 1963. Experimental deformation of sedimentary rocks under confining pressure: pore pressure tests. Aapg Bulletin, 47(5), pp.717-755.

Hao, L., Ke, P. and June, W., 1985. An anisotropic damage criterion for deformation instability and its application to forming limit analysis of metal plates. Engineering Fracture Mechanics, 21(5), pp.1031-1054.

Hashin, Z. and Shtrikman, S., 1963. A variational approach to the theory of the elastic behaviour of multiphase materials. Journal of the Mechanics and Physics of Solids, 11(2), pp.127-140.

Heerens, J., Zerbst, U., Bauschke, H.M. and Schwalbe, K.H., 2013. On the application of the weakest link model in the lower shelf and transition. In ECF10, Berlin 1994.

Herring, C., 1951. Some theorems on the free energies of crystal surfaces. Physical Review, 82(1), p.87.

Hertz, H., 1882. On the evaporation of liquids, especially mercury, in vacuo. Ann. Phys, 17, pp.178-193.

Hill, R., 1965. A self-consistent mechanics of composite materials. Journal of the Mechanics and Physics of Solids, 13(4), pp.213-222.

Hirth, J.P. and Lothe, J., 1968. Theory of Dislocations, McGraw-Hill. New York. USA. 780 pp.

Hoek, E. and Bieniawski, Z.T., 1965. Brittle fracture propagation in rock under compression. International Journal of Fracture Mechanics, 1(3), pp.137-155.

Hoomans, B.P.B., Kuipers, J.A.M., Briels, W.J. and Van Swaaij, W.P.M., 1996. Discrete particle simulation of bubble and slug formation in a two-dimensional gas-fluidised bed: a hard-sphere approach. Chemical Engineering Science, 51(1), pp.99-118.

Horii, H. and Nemat-Nasser, S., 1985. Compression-induced microcrack growth in brittle solids: axial splitting and shear failure. J. geophys. Res, *90*(B4), pp.3105-3125.

Irwin, G.R., 1957. Analysis of stresses and strains near the end of a crack traversing a plate. Spie Milestone series MS, 137(167-170), p.16.

Irwin, G.R., 1958. Fracture in "Handbuch der Physik," vol. V. Springer-Verlag Berlin, Göttingen, Heidelberg.

Ishii, M., 1975. Thermo-Fluid Dynamic Theory of Two-Phase Flow. Direction des études et recherches d'électricité de France. Volume 22. Eyrolles, Paris

Iwadate, T., Tanaka, Y., Ono, S., and Watanabe, J., "An Analysis of Elastic-Plastic Fracture Toughness Behavior for J^{Ic} Measurement in the Transition Region," Elastic-Plastic Fracture: Second Symposium, Volume II Fracture Resistance Curves and Engineering Applications, STP36785S, ASTM International, West Conshohocken, PA, 1983, pp. 531-561.

Iwasaki, T., Slade, J.J. and Stanley, W.E., 1937. Some notes on sand filtration [with discussion]. Journal (American Water Works Association), 29(10), pp.1591-1602.

Jacqmin, D., 1999. Calculation of two-phase Navier–Stokes flows using phase-field modeling. Journal of Computational Physics, 155(1), pp.96-127.

Jaeger, J.C. and Cook, N.G.W., 1979. Fundamentals of rock mechanics. Chapman and Hall, New York. 593 pp.

James, A.J. and Lowengrub, J., 2004. A surfactant-conserving volume-of-fluid method for interfacial flows with insoluble surfactant. Journal of computational physics, 201(2), pp.685-722.

Jan, Y.J. and Tryggvason, G., 1991, June. Computational studies of contaminated bubbles. In Proceedings of a symposium on the dynamics of bubbles and vorticity near free surfaces. Ed. I. Sahin and G. Tryggvason, ASME (Vol. 46).

Johnson, R.A. and Borhan, A., 2000. Stability of the shape of a surfactant-laden drop translating at low Reynolds number. Physics of Fluids, 12(4), pp.773-784.

Ju, J. and Chen, T.M., 1994b. Effective elastic moduli of two-dimensional brittle solids with interacting microcracks. II: Evolutionary damage models. Journal of applied mechanics, 61(2), pp.358-366.

Ju, J.W. and Chen, T.M., 1994a. Effective elastic moduli of two-dimensional brittle solids with interacting microcracks, Part I: basic formulations. Transactions-American Society of Mechanical Engineers Journal of Applied Mechanics, Vol. 61, pp.349-349.

Ju, J.W. and Lee, X., 1991. Micromechanical damage models for brittle solids. Part I: tensile loadings. Journal of Engineering Mechanics, 117(7), pp.1495-1514.

Kachanov, L., 2013. Introduction to continuum damage mechanics (Vol. 10). Springer Science & Business Media.

Kachanov, L.M. and Krajcinovic, D., 1987. Introduction to continuum damage mechanics. Martinus Nijhoff Publishers, The Netherlands.

Kachanov, L.M., 1958. On rupture time under condition of creep. Izvestia Akademi Nauk USSR, Otd. Techn. Nauk, Moskwa, 8, pp.26-31.

Kan, H.C., Udaykumar, H.S., Shyy, W. and Tran-Son-Tay, R., 1998. Hydrodynamics of a compound drop with application to leukocyte modeling. Physics of fluids, 10(4), pp.760-774.

Kemeny, J.M. and Cook, N.G., 1986. Crack models for the failure of rocks in compression (No. LBL-25311; CONF-870103-7). Lawrence Berkeley Lab., CA (USA).

Khilar, K.C., Fogler, H.S. and Gray, D.H., 1985. Model for piping-plugging in earthen structures. Journal of Geotechnical Engineering, 111(7), pp.833-846.

Kim, H.G., Lee, C.M., Lim, H.C. and Kyong, N.H., 1997. An experimental and numerical study on the flow over two-dimensional hills. Journal of Wind Engineering and Industrial Aerodynamics, 66(1), pp.17-33.

Kim, J. and Lowengrub, J., 2005. Phase field modeling and simulation of three-phase flows. Interfaces and free boundaries, 7(4), pp.435-466.

Kim, J., 2012. Phase-field models for multi-component fluid flows. Communications in Computational Physics, 12(03), pp.613-661.

Kim, J., Kang, K. and Lowengrub, J., 2004. Conservative multigrid methods for ternary Cahn-Hilliard systems. Communications in Mathematical Sciences, 2(1), pp.53-77.

Kolosoff, G., 1914. On some properties of problems in the plane theory of elasticity. Z. Math. Physik, 62, pp.384-409.

Krajcinovic, D. and Fonseka, G.U., 1981. The continuous damage theory of brittle materials. J. appl. Mech, 48(4), pp.809-824.

Krajcinovic, D., 1983. Constitutive equations for damaging materials. Journal of applied Mechanics, 50(2), pp.355-360.

Krajcinovic, D., 1985. Continuous damage mechanics revisited: basic concepts and definitions. Journal of Applied Mechanics, 52(4), pp.829-834.

Kuchuk, F.J., Goode, P.A., Wilkinson, D.J. and Thambynayagam, R.K.M., 1991. Pressure-transient behavior of horizontal wells with and without gas cap or aquifer. SPE Formation Evaluation, 6(01), pp.86-94.

Kuipers, J.A.M., 1990. A two-fluid micro balance model of fluidized beds. PhD Diss., Twente Univ. of Technology, The Netherlands.

Kunii, D. and Levenspiel, O., 1991. Flow modeling of fast fluidized beds. Circulating fluidized bed technology III, pp.91-98.

Landau, L.D. and Lifshitz, E.M., 1959. Course of Theoretical Physics Vol 7: Theory and Elasticity. Pergamon press, Oxford, UK.

Landes, J. and Shaffer, D., "Statistical Characterization of Fracture in the Transition Region," *Fracture Mechanics*, STP36981S, P. Paris, Ed., ASTM International, West Conshohocken, PA, 1980, pp. 368-382.

Langston, P.A., Tüzün, U. and Heyes, D.M., 1994. Continuous potential discrete particle simulations of stress and velocity fields in hoppers: transition from fluid to granular flow. Chemical Engineering Science, 49(8), pp.1259-1275.

Laviéville, J., Deutsch, E. and Simonin, O., 1995. Large eddy simulation of interactions between colliding particles and a homogeneous isotropic turbulence field. ASME-Publications-Fed, 228, pp.347-358.

Lemaitre, J. and Chaboche, J.L., 1985. Mécanique des Matériaux SolidesEdition Dunod. Paris.

Lemaitre, J., 1985. A continuous damage mechanics model for ductile fracture. Transactions of the ASME. Journal of Engineering Materials and Technology, 107(1), pp.83-89.

Lemaitre, J., 1986. Local approach of fracture. Engineering Fracture Mechanics, Vol. 25(5-6), pp.523-537.

Leva, M., 1959. Fluidization. McGraw-Hill, New York, USA.

Li, Y. and Zhou, M., 2013. Prediction of fracture toughness of ceramic composites as function of microstructure: I. Numerical simulations. Journal of the Mechanics and Physics of Solids, 61(2), pp.472-488.

Liu, C. and Shen, J., 2003. A phase field model for the mixture of two incompressible fluids and its approximation by a Fourier-spectral method. Physica D: Nonlinear Phenomena, 179(3), pp.211-228.

Ljus, C., 2000. On particle transport and turbulence modification in air-particle flows. Doctoral Thesis, Chalmers University of Technology.

Lowengrub, J. and Truskinovsky, L., 1998. Quasi–incompressible Cahn–Hilliard fluids and topological transitions. In Proceedings of the Royal Society of London A: Mathematical, Physical and Engineering Sciences (Vol. 454, No. 1978, pp. 2617-2654). The Royal Society.

Lun, C.K. and Savage, S.B., 1986. The effects of an impact velocity dependent coefficient of restitution on stresses developed by sheared granular materials. Acta Mechanica, 63(1), pp.15-44.

Maloney, S. and Kaiser, P.K., 1989, January. Results of borehole breakout simulation tests. In ISRM International Symposium. International Society for Rock Mechanics.

Martin, C.D., Martino, J.B. and Dzik, E.J., 1994, January. Comparison of borehole breakouts from laboratory and field tests. In Rock Mechanics in Petroleum Engineering. Society of Petroleum Engineers.

Maury, V., 1992. An overview of tunnel, underground excavation and borehole collapse mechanisms. Comprehensive Rock Engineering, 4, pp.369-412.

Maury, V.M. and Sauzay, J., 1987, January. Borehole instability: case histories, rock mechanics approach, and results. In SPE/IADC Drilling Conference. Society of Petroleum Engineers.

Mehta, A.J., 1991, June. Review notes on cohesive sediment erosion. In Coastal Sediments: (pp. 40-53). ASCE.

Meyer, B.R., 1986, January. Design formulae for 2-D and 3-D vertical hydraulic fractures: model comparison and parametric studies. In SPE Unconventional Gas Technology Symposium. Society of Petroleum Engineers.

Milliken, W.J. and Leal, L.G., 1994. The influence of surfactant on the deformation and breakup of a viscous drop: The effect of surfactant solubility. Journal of Colloid and Interface Science, 166(2), pp.275-285.

Mindlin, R.D. and Deresiewicz, H., 1953. Timoshenko's shear coefficient for flexural vibrations of beams (No. TR-10). Columbia University, New York.

Morales, R.H., Brady, B.H. and Ingraffea, A.R., 1993, January. Three-dimensional analysis and visualization of the wellbore and the fracturing process in inclined wells. In Low Permeability Reservoirs Symposium. Society of Petroleum Engineers.

Morales, R.H., Brady, B.H. and Ingraffea, A.R., 1993, January. Three-dimensional analysis and visualization of the wellbore and the fracturing process in inclined wells. In Low Permeability Reservoirs Symposium. Society of Petroleum Engineers.

Mori, T. and Tanaka, K., 1973. Average stress in matrix and average elastic energy of materials with misfitting inclusions. Acta metallurgica, 21(5), pp.571-574.

Morita, N. and Nagano, Y., 2016, September. Comparative Analysis of Various Failure Theories for Borehole Breakout Predictions. In SPE Annual Technical Conference and Exhibition. Society of Petroleum Engineers.

Morita, N., Whitfill, D.L., Massie, I. and Knudsen, T.W., 1989. Realistic sand-production prediction: numerical approach. SPE Production Engineering, 4(01), pp.15-24.

Mudry, F., 1982. Study of ductile fracture and fracture by cleavage of low alloy steels. Third State, UniversitC de Technologie de Compikgne.

Mühlhaus, H.B. and Vardoulakis, I., 1987. The thickness of shear bands in granular materials. Geotechnique, 37(3), pp.271-283.

Nawrocki, P.A. and Dusseault, M.B., 1995. Modelling of damaged zones around openings using radius-dependent Young's modulus. Rock mechanics and rock engineering, 28(4), pp.227-239.

Nemat-Nasser, S. and Horii, H., 1982. Compression-induced nonplanar crack extension with application to splitting, exfoliation, and rockburst. Journal of Geophysical Research: Solid Earth, 87(B8), pp.6805-6821.

Nemat-Nasser, S. and Horii, H., 1982. Compression-induced nonplanar crack extension with application to splitting, exfoliation, and rockburst. Journal of Geophysical Research: Solid Earth, 87(B8), pp.6805-6821.

Newberry, B.M., Nelson, R.F. and Ahmed, U., 1985. Prediction of vertical hydraulic fracture migration using compressional and shear wave slowness. In SPE/DOE Low Permeability Gas Reservoirs Symposium. Society of Petroleum Engineers.

Nichols, J.M. and Abell, A.B., 2003. Implementing the degrading effective stiffness of masonry in a finite element model. In Proceedings of the North American Masonry Conference, Clemson, SC. June, pp. 1-4.

Nichols, J.M. and Totoev, Y.Z., 1999. Experimental investigation of the damage mechanics of masonry under dynamic in-plane loads. In Proceedings of the North American Masonry Conference, Austin, TX, June, pp. 6-9.

Nordgren, R.P., 1972. Propagation of a vertical hydraulic fracture. Society of Petroleum Engineers Journal, 12(04), pp.306-314.

Nott, P.R., 1991. Analysis of granular flow in aerated and vibrated chutes. Doctoral dissertation, Princeton University.

Nur, A., 1974. Tectonophysics: the study of relations between deformation and forces in the earth. Advances in Rock Mechanics, 1, pp.243-317.

Odeh, A.S. and Babu, D.K., 1989, January. Transient flow behavior of horizontal wells, pressure drawdown, and buildup analysis. In SPE California Regional Meeting. Society of Petroleum Engineers.

Olson, J.E. and Taleghani, A.D., 2009, January. Modeling simultaneous growth of multiple hydraulic fractures and their interaction with natural fractures. In SPE Hydraulic Fracturing Technology Conference. Society of Petroleum Engineers.

Ortlepp, W.D. and Moore, M.A., 1987, January. Underground observation of high propagation-rate, extension fractures. In 6th ISRM Congress. International Society for Rock Mechanics.

Ortlepp, W.D., 1983, January. Considerations in the design of support for deep hard-rock tunnels. In 5th ISRM Congress. International Society for Rock Mechanics.

Othmer, D.F. ed., 1956. Fluidization. Reinhold Publishing Corporation, New York, USA.

Oyedokun O. and Schubert J. 2017. On Shear Dilatancy in Rocks, a Necessary Condition for Material Indifference. (Submitted to International Journal of Rock Mechanics and Mining Sciences).

Palmer, I.D. and Carroll Jr, H.B., 1983, January. Numerical solution for height and elongated hydraulic fractures. In SPE/DOE Low Permeability Gas Reservoirs Symposium. Society of Petroleum Engineers.

Palmer, I.D. and Carroll Jr, H.B., 1983. Three-dimensional hydraulic fracture propagation in the presence of stress variations. Society of Petroleum Engineers Journal, 23(06), pp.870-878.

Palmer, I.D. and Craig, H.R., 1984, January. Modeling of asymmetric vertical growth in elongated hydraulic fractures and application to first MWX stimulation. In SPE Unconventional Gas Recovery Symposium. Society of Petroleum Engineers.

Papamichos, E. and Stavropoulou, M., 1998. An erosion-mechanical model for sand production rate prediction. International Journal of Rock Mechanics and Mining Sciences, 35(4-5), pp.531-532.

Papamichos, E. and Vardoulakis, I., 2005. Sand erosion with a porosity diffusion law. Computers and Geotechnics, 32(1), pp.47-58.

Papamichos, E., 2004. Failure in rocks: hydro-mechanical coupling for erosion. Revue française de génie civil, 8(5-6), pp.709-734.

Papamichos, E., 2006. Sand production: Physical and experimental evidence. Revue européenne de génie civil, 10(6-7), pp.803-816.

Papanastasiou PC, Vardoulakis IG. 1994. Numerical analysis of borehole stability problem. Soil structure interaction: numerical analysis and modelling. E&FN Spon, p. 673-711 Chap. 19.

Papanastasiou, P.C. and Vardoulakis, I.G., 1992. Numerical treatment of progressive localization in relation to borehole stability. International Journal for Numerical and Analytical Methods in Geomechanics, 16(6), pp.389-424.

Papatzacos, P., 1987. Approximate partial-penetration pseudoskin for infinite-conductivity wells. SPE Reservoir Engineering, 2(02), pp.227-234.

Partheniades, E., 1965. Erosion and deposition of cohesive soils. Journal of the Hydraulics Division, 91(1), pp.105-139.

Peach, M. and Koehler, J.S., 1950. The forces exerted on dislocations and the stress fields produced by them. Physical Review, 80(3), p.436.

Perie, P.J. and Goodman, R.E., 1989. Evidence of new failure patterns in a thick-walled cylinder experiment. In Proc. 12th ETCE/ASME Conf. (Vol. 22, pp. 23-27).

Perkins, T.K. and Kern, L.R., 1961. Widths of hydraulic fractures. Journal of Petroleum Technology, 13(09), pp.937-949.

Perkins, T.K. and Weingarten, J.S., 1988, January. Stability and failure of spherical cavities in unconsolidated sand and weakly consolidated rock. In SPE Annual Technical Conference and Exhibition. Society of Petroleum Engineers.

Peskin, C.S., 1977. Numerical analysis of blood flow in the heart. Journal of computational physics, 25(3), pp.220-252.

Plumb, R.A., 1989, January. Fracture patterns associated with incipient wellbore breakouts. In ISRM International Symposium. International Society for Rock Mechanics.

Podio-Guidugli, P., 2006. Models of phase segregation and diffusion of atomic species on a lattice. Ricerche di Matematica, 55(1), pp.105-118.

Pritchett, J.W., Blake, T.R. and Garg, S.K., 1978. A numerical model of gas fluidized beds. In AIChE Symp. Ser (Vol. 74, No. 176, p. 134).

Pritchett, J.W., Blake, T.R. and Garg, S.K., 1978. A numerical model of gas fluidized beds. In AIChE Symp. Ser (Vol. 74, No. 176, p. 134).

Reiner, M., 1945. A mathematical theory of dilatancy. American Journal of Mathematics, 67(3), pp.350-362.

Reiner, M., 1948. Elasticity beyond the elastic limit. American Journal of Mathematics, 70(2), pp.433-446.

Renardy, Y.Y., Renardy, M. and Cristini, V., 2002. A new volume-of-fluid formulation for surfactants and simulations of drop deformation under shear at a low viscosity ratio. European Journal of Mechanics-B/Fluids, 21(1), pp.49-59.

Renshaw, C.E. and Pollard, D.D., 1995, April. An experimentally verified criterion for propagation across unbounded frictional interfaces in brittle, linear elastic materials.

In International journal of rock mechanics and mining sciences & geomechanics abstracts (Vol. 32, No. 3, pp. 237-249). Pergamon.

Rousselier, G., 1981. Finite deformation constitutive relations including ductile fracture damage. Three-dimensional constitutive relations and ductile fracture. (A 83-18477 06-39) Amsterdam, North-Holland Publishing Co., 1981, pp.331-355.

Sakthivadivel, R. and Irmay, S., 1966. A review of filtration theories. University of California, Hydraulic Engineering Laboratory, College of Engineering.

Scheuermann, A., Vardoulakis, I., Papanastasiou, P. and Stavropoulou, M., 2001. A sand erosion problem in axial flow conditions on the example of contact erosion due to horizontal groundwater flow. In IUTAM Symposium on Theoretical and Numerical Methods in Continuum Mechanics of Porous Materials (pp. 169-175). Springer Netherlands.

Settari, A. and Cleary, M.P., 1986. Development and testing of a pseudo-three-dimensional model of hydraulic fracture geometry. SPE Production Engineering, 1(06), pp.449-466.

Shao, J.F., Kondo, D. and Ikogou, S., 1994, April. Stress-induced microcracking in rock and its influence on wellbore stability analysis. In International journal of rock mechanics and mining sciences & geomechanics abstracts (Vol. 31, No. 2, pp. 149-155). Pergamon.

Sih, G.C., 1974. Strain-energy-density factor applied to mixed mode crack problems. International Journal of fracture, 10(3), pp.305-321.

Simonson, E.R., Abou-Sayed, A.S. and Clifton, R.J., 1978. Containment of massive hydraulic fractures. Society of Petroleum Engineers Journal, 18(01), pp.27-32.

Sinclair, J.L. and Jackson, R., 1989. Gas-particle flow in a vertical pipe with particle-particle interactions. AIChE Journal, 35(9), pp.1473-1486.

Skalle, P. and Podio, A.L., 1998, January. Trends extracted from 800 Gulf Coast blowouts during 1960-1996. In IADC/SPE drilling conference. Society of Petroleum Engineers.

Skalle, P., Jinjun, H. and Podio, A.L., 1999, January. Killing methods and consequences of 1120 gulf coast blowouts during 1960-1996. In Latin American and Caribbean Petroleum Engineering Conference. Society of Petroleum Engineers.

Slatcher, S., 1986. A Probabilistic Model for Lower-Shelf Fracture Toughness—Theory and Application. Fatigue & Fracture of Engineering Materials & Structures, 9(4), pp.275-289.

Smith, K.A., Solis, F.J. and Chopp, D., 2002. A projection method for motion of triple junctions by level sets. Interfaces and free boundaries, 4(3), pp.263-276.

Stacey, T. and De Jongh, C.L., 1977. Stress fracturing around a deep-level bored tunnel. Journal of the South African Institute of Mining and Metallurgy, pp.124-133.

Stavropoulou, M., Papanastasiou, P. and Vardoulakis, I., 1998. Coupled wellbore erosion and stability analysis. International journal for numerical and analytical methods in geomechanics, 22(9), pp.749-769.

Steinbach, I., Pezzolla, F., Nestler, B., Seeßelberg, M., Prieler, R., Schmitz, G.J. and Rezende, J.L., 1996. A phase field concept for multiphase systems. Physica D: Nonlinear Phenomena, 94(3), pp.135-147.

Stevenson, A.C., 1945, August. Complex potentials in two-dimensional elasticity. In Proceedings of the Royal Society of London A: Mathematical, Physical and Engineering Sciences (Vol. 184, No. 997, pp. 129-179). The Royal Society.

Stone, H.A. and Leal, L.G., 1990. The effects of surfactants on drop deformation and breakup. Journal of Fluid Mechanics, 220, pp.161-186.

Stone, T.J. and Babuška, I., 1998. A numerical method with a posteriori error estimation for determining the path taken by a propagating crack. Computer methods in applied mechanics and engineering, 160(3), pp.245-271

Sun C.T and Jin, Z.H 2012. Mixed Mode Fracture. Fracture Mechanics. Waltham, Massachussetts, USA: Academic Press. pp 105-121.

Swanson, S. R. (1969). Development of Constitutive Equations for Rocks, Ph.D. Thesis, University of Utah.

Syamlal, M., 1987. A review of granular stress constitutive relations (No. DOE/MC/21353-2372). EG and G Washington Analytical Services Center, Inc., Morgantown, WV (USA)

Thomson, W. (Lord Kelvin) (1875). Elasticity. Encyclopedia Britannica, United Kingdon, 9th Edition. pp 431-444.

Thornton, C. and Yin, K.K., 1991. Impact of elastic spheres with and without adhesion. Powder technology, 65(1-3), pp.153-166.

Thornton, C., 1997. Force transmission in granular media. KONA Powder and Particle Journal, 15, pp.81-90.

Timoshenko, S. and Goodier, J.N., Theory of elasticity. 1951. McGraw-Hill, New York, 412, p.108.

Truedell, C. and Noll, W., 1992. The nonlinear field theories of mechanics. Handbuch der Physik. Flügge, S., (Ed.), Bd. III/3. Berlin-Göttingen-Heidelberg: Springer.

Truskinovsky, L., 1993. Kinks versus shocks. In Shock induced transitions and phase structures in general media. Springer, New York. pp. 185-229.

Tsuji, Y., Kawaguchi, T. and Tanaka, T., 1993. Discrete particle simulation of two-dimensional fluidized bed. Powder technology, 77(1), pp.79-87.

Valko, P.P. and Liu, S., 2015, February. An Improved Equilibrium-Height Model for Predicting Hydraulic Fracture Height Migration in Multi-Layered Formations. In SPE Hydraulic Fracturing Technology Conference. Society of Petroleum Engineers.

Van der Waals, J.D., 1893. Thermodynamische theorie der capillariteit in de onderstelling van continue dichtheidsverandering, Verhand. Kon. Akad. Wetensch. Amsterdam Sect, 1.

Van Wachem, B.G.M. and Almstedt, A.E., 2003. Methods for multiphase computational fluid dynamics. Chemical Engineering Journal, 96(1), pp.81-98.

Vardoulakis, I. and Papamichos, E., 2001. A continuum theory for erosion in granular media. Actes de la journées scientifique Internationale, Cermes, 21, pp.41-60.

Vardoulakis, I. and Sulem, J., 1995. Bifurcation analysis in geomechanics. Hapman & Hall, London, England.

Vardoulakis, I., Papanastasiou, P. and Stavropoulou, M., 2001. Sand erosion in axial flow conditions. Transport in Porous Media, 45(2), pp.267-280.

Vardoulakis, I., Stavropoulou, M. and Papanastasiou, P., 1996. Hydro-mechanical aspects of the sand production problem. Transport in porous media, 22(2), pp.225-244.

Vaziri, H.H., 1988. Theoretical analysis of stress, pressure, and formation damage during production. Journal of Canadian Petroleum Technology, 27(06).

Voyiadjis, G.Z. and Kattan, P.I., 2005. Damage mechanics. CRC Press, Boca Raton, Florida, USA.

Voyiadjis, G.Z., 1988. Degradation of elastic modulus in elastoplastic coupling with finite strains. International Journal of Plasticity, 4(4), pp.335-353.

Voyiadjis, G.Z., 2012. Advances in damage mechanics: metals and metal matrix composites. Elsevier.

Vu-Quoc, L. and Zhang, X., 1999a, November. An elastoplastic contact force–displacement model in the normal direction: displacement–driven version. In Proceedings of the Royal Society of London A: Mathematical, Physical and Engineering Sciences (Vol. 455, No. 1991, pp. 4013-4044). The Royal Society.

Vu-Quoc, L. and Zhang, X., 1999b. An accurate and efficient tangential force–displacement model for elastic frictional contact in particle-flow simulations. Mechanics of materials, 31(4), pp.235-269.

Wallin, K., Saario, T. and Törrönen, K., 2013. Statistical model for carbide induced brittle fracture in steel. Metal Science. Vol. 18. Iss. 1,1984. pp 13-16.

Walpole, L.J., 1981. Elastic behavior of composite materials: theoretical foundations. Advances in applied mechanics, 21, pp.169-242.

Walton, O.R. and Braun, R.L., 1986. Viscosity, granular-temperature, and stress calculations for shearing assemblies of inelastic, frictional disks. Journal of Rheology, 30(5), pp.949-980.

Walton, O.R., 1993. Numerical simulation of inelastic, frictional particle-particle interactions. In M.C., Roco (Ed.). Particulate two-phase flow, Butterworth-Heinemann, Boston, MA. pp 884-911.

Wan, R.G. and Wang, J., 2002, January. Modeling sand production and erosion growth under combined axial and radial flow. In SPE International Thermal Operations and Heavy Oil Symposium and International Horizontal Well Technology Conference. Society of Petroleum Engineers.

Wan, R.G. and Wang, J., 2002, January. Modeling sand production and erosion growth under combined axial and radial flow. In SPE International Thermal Operations and Heavy Oil Symposium and International Horizontal Well Technology Conference. Society of Petroleum Engineers.

Warpinski, N.R. and Teufel, L.W., 1987. Influence of geologic discontinuities on hydraulic fracture propagation (includes associated papers 17011 and 17074). Journal of Petroleum Technology, 39(02), pp.209-220.

Weng, G.J., 1984. Some elastic properties of reinforced solids, with special reference to isotropic ones containing spherical inclusions. International Journal of Engineering Science, 22(7), pp.845-856.

Wheeler, A.A., Boettinger, W.J. and McFadden, G.B., 1992. Phase-field model for isothermal phase transitions in binary alloys. Physical Review A, 45(10), p.7424.

Willis, J.R., 1981. Variational and related methods for the overall properties of composites. Advances in applied mechanics, 21, pp.1-78.

Willson, S.M., 2012, January. A Wellbore Stability Approach for Self-Killing Blowout Assessment. In SPE Deepwater Drilling and Completions Conference. Society of Petroleum Engineers.

Wilson, S.M., Nagoo, A.S. and Sharma, M.M., 2013, March. Analysis of Potential Bridging Scenarios during Blowout Event. In SPE/IADC 163438 presented at the SPE/IADC Drilling Conference and Exhibition held in Amsterdam, the Netherlands (pp. 5-7).

Wu, K., 2014. Mechanics analysis of interaction between hydraulic and natural fractures in shale reservoirs. Unconventional Resources Technology Conference (URTEC).

Yue, P., Feng, J.J., Liu, C. and Shen, J., 2004. A diffuse-interface method for simulating two-phase flows of complex fluids. Journal of Fluid Mechanics, 515, pp.293-317.

Zenz, F.A. and Othmer, D.F., 1960. Fluidization and fluid-particle systems. Reinhold. Reinhold Publishing Corporation, New York, USA.

Zhou, J., Chen, M., Jin, Y. and Zhang, G.Q., 2008. Analysis of fracture propagation behavior and fracture geometry using a tri-axial fracturing system in naturally fractured reservoirs. International Journal of Rock Mechanics and Mining Sciences, 45(7), pp.1143-1152.

Zhou, J., Huang, H. and Deo, M., 2015, November. Modeling the Interaction between Hydraulic and Natural Fractures Using Dual-Lattice Discrete Element Method. In 49th US Rock Mechanics/Geomechanics Symposium. American Rock Mechanics Association.

Zhu, H.P., Zhou, Z.Y., Yang, R.Y. and Yu, A.B., 2007. Discrete particle simulation of particulate systems: theoretical developments. Chemical Engineering Science, 62(13), pp.3378-3396.

Zoback, M.D., Moos, D., Mastin, L. and Anderson, R.N., 1985. Well bore breakouts and in situ stress. Journal of Geophysical Research: Solid Earth, 90(B7), pp.5523-5530.

Zou, Y., Taylor, W.E.G. and Heath, D.J., 1996, January. A numerical model for borehole breakouts. In International journal of rock mechanics and mining sciences & geomechanics abstracts (Vol. 33, No. 1, pp. 103-109). Pergamon.

Zreik, D.A., Krishnappan, B.G., Germaine, J.T., Madsen, O.S. and Ladd, C.C., 1998. Erosional and mechanical strengths of deposited cohesive sediments. Journal of Hydraulic Engineering, 124(11), pp.1076-1085.

APPENDIX A

DERIVATION OF MINIMUM FRACTURE PROPAGATION PRESSURE FOR THREE-LAYER PROBLEM

Sneddon and Elliot (1946) derived the stress intensity factor at the tip of a fracture subjected to a constant internal pressure. Modifying the equation by including the effect of gravity, the stress intensity factor at the bottom tip, when the fracture is contained in formation n only:

$$K_{I,D} = \frac{1}{\sqrt{\pi l}} \int_{-l}^{z} p(z,t) - \sigma_n \sqrt{\frac{l+z}{l-z}}\, dz \quad \text{..... (A.6.1)}$$

Let $z^* = \frac{z}{l}$ ..... (A.6.2)

And at $\left.\begin{matrix} z = z, z^* = z^* \\ z = -l, z^* = -1 \end{matrix}\right\}$ ..... (A.6.3)

$$\frac{dz^*}{dz} = \frac{1}{l} \quad \text{..... (A.6.4)}$$

Substituting (A.6.3) and (A.6.4) into (A.6.1),

$$K_{I,D} = \sqrt{\frac{l}{\pi}} \int_{-1}^{z^*} \left(p_Q(t) + \rho g l z^* - \sigma_n \right) \sqrt{\frac{1+z^*}{1-z^*}}\, dz^* \quad \text{..... (A.6.5)}$$

Solving (A.6.5) and substituting (A.6.2) back yields

$$K_{I,D}=\frac{1}{2\sqrt{\pi}\sqrt{l(l-z)}}\left\{-(l-z)\sqrt{l+z}\left(g(2l+z)\rho-2\sigma_n\right)\right.$$
$$\left.+2l\sqrt{l-z}\left(gl\rho-2\sigma_n\right)\sin^{-1}\left(\frac{\sqrt{\frac{l+z}{l}}}{\sqrt{2}}\right)+p_Q\left(2(-l+z)\sqrt{l+z}+4l\sqrt{l-z}\sin^{-1}\left(\frac{\sqrt{\frac{l+z}{l}}}{\sqrt{2}}\right)\right)\right\} \quad \text{..... (A.6.6)}$$

$$\lim_{z\to l}\left\{K_{I,D}\right\}=\frac{\sqrt{l\pi}}{2}\left(gl\rho+2p_Q-2\sigma_n\right) \quad \text{..... (A.6.7)}$$

Therefore, the critical pressure at the mid position Q to cause the lower tip to move is

$$p_Q=P_{FD}=\left(\frac{K_{IC,D}}{\sqrt{\pi l}}+\sigma_n-\frac{1}{2}gl\rho\right) \quad \text{..... (A6.8)}$$

At the upper tip, the stress intensity factor is

$$K_{I,U}=\frac{1}{\sqrt{\pi l}}\int_{-l}^{z}p(z,t)-\sigma_n\sqrt{\frac{l-z}{l+z}}dz \quad \text{..... (A.6.9)}$$

Let $z^*=-\frac{z}{l}$ ..... (A.6.10)

And at $\left.\begin{matrix}z=z,z^*=-z^*\\ z=-l,z^*=1\end{matrix}\right\}$ .....(A.6.11)

$$\frac{dz^*}{dz}=-\frac{1}{l} \quad \text{..... (A.6.12)}$$

Substituting (A.6.11) and (A.6.12) into (A.6.9),

$$K_{I,U}=\sqrt{\frac{l}{\pi}}\int_{-z^*}^{1}\left(p_Q(t)-\rho glz^*-\sigma_n\right)\sqrt{\frac{1+z^*}{1-z^*}}dz^* \quad \text{..... (A.6.13)}$$

Solving (A.6.13) and substituting (A.6.2) back yields

$$K_{I,U} = \frac{1}{2\sqrt{\pi}\sqrt{l(l-z)}}\left\{-(l-z)\sqrt{(l+z)}\left(g(2l+z)\rho+2\sigma_n\right)\right.$$
$$\left.-2l\sqrt{(l-z)}(gl\rho+2\sigma_n)\cos^{-1}\left(\frac{\sqrt{\frac{l+z}{l}}}{\sqrt{2}}\right)+2p_Q\left((l-z)\sqrt{(l+z)}+2l\sqrt{(l-z)}\cos^{-1}\left(\frac{\sqrt{\frac{l+z}{l}}}{\sqrt{2}}\right)\right)\right\} \quad \text{... (A.6.14)}$$

$$\lim_{z\to l}\left\{K_{I,U}\right\} = \frac{\sqrt{l\pi}}{2}\left(-gl\rho+2p_Q-2\sigma_n\right) \quad \text{..... (A.6.15)}$$

Therefore, the critical pressure at midpoint Q to cause the upper tip to move is

$$p_Q = P_{FU} = \left(\frac{K_{IC,U}}{\sqrt{\pi l}}+\sigma_n+\frac{1}{2}gl\rho\right) \quad \text{..... (A.6.16)}$$

Noting that $l = h_\xi$. Hence, extending the derivation to three layer: the stress intensity factor at the upper tip is

$$K_{I,U} = \frac{1}{\sqrt{\pi l}}\left\{\int_{-k_3}^{1}\left(p_Q(t)-\rho glz^*-\sigma_3\right)\sqrt{\frac{1+z^*}{1-z^*}}dz^*+\int_{-k_1}^{-k_3}\left(p_Q(t)-\rho glz^*-\sigma_2\right)\sqrt{\frac{1+z^*}{1-z^*}}dz^*\right.$$
$$\left.+\int_{-z^*}^{-k_1}\left(p_Q(t)-\rho glz^*-\sigma_1\right)\sqrt{\frac{1+z^*}{1-z^*}}dz^*\right\}_{z\to l} \quad \text{..... (A.6.17)}$$

Therefore, the minimum fracture extension pressure for the upper tip at any location z is p_Q in A.6.17; since the algebraic expression is complicated, it will not be displayed in this paper. In the same vein, when k_1 approaches unity, the fracture extension pressure for the upper tip corresponds to case 2 in Fig. 6.3. And when k_3 approaches unity, the fracture extension pressure for the upper tip corresponds to case 3 in Fig. 6.3.

Similarly, the stress intensity factor at the lower tip is

$$K_{I,D} = \frac{1}{\sqrt{\pi l}} \left\{ \int_{-1}^{k_3} \left(p_Q(t) + \rho g l z^* - \sigma_3 \right) \sqrt{\frac{1+z^*}{1-z^*}} dz^* + \int_{k_3}^{k_1} \left(p_Q(t) + \rho g l z^* - \sigma_2 \right) \sqrt{\frac{1+z^*}{1-z^*}} dz^* + \int_{k_1}^{z} \left(p_Q(t) + \rho g l z^* - \sigma_1 \right) \sqrt{\frac{1+z^*}{1-z^*}} dz^* \right\}_{z \to l} \quad \text{..... (A.6.18)}$$

And when k_1 approaches unity, the fracture extension pressure for the lower tip corresponds to case 3 in Fig. 6.3. While when k_3 approaches unity, the fracture extension pressure for the lower tip corresponds to case 2 in Fig. 6.3.

APPENDIX B

LIST OF PUBLICATIONS WRITTEN FROM THE DISSERTATION

B.1 Peer-Reviewed Articles:

I. Oyedokun O, Schubert J. 2016. A Quick and Energy Consistent Analytical Method for Predicting Hydraulic Fracture Propagation through Layered Media and Jointed Rock Mass: The Use of an Effective Fracture Toughness. *Journal of Natural Gas Science and Engineering* (Accepted, in Press): *The paper presents an effective fracture toughness, which is based on equivalent energy release-rate hypothesis for homogenizing heterogeneous layered media*.

B.2 Manuscripts Under Peer Review

II. Oyedokun, O. and Schubert, J. Theoretical Development on Morphology of Wellbore Toroidal Breakout. *In 50th US Rock Mechanics/Geomechanics Symposium. American Rock Mechanics Association: The study presents two methodologies based on shear-failure theory and fracture mechanics approach for predicting the shape of type B breakout.*

III. Oyedokun O. and Schubert J. 2017. A Thermodynamically Consistent MultiPhase-Field Model for Non-Isothermal Transport of Gas-Liquid-Solid Particle Flow. Part 1: Theoretical Development (Submitted to *Journal of Fluid Mechanics*): *The paper presents a thermodynamically consistent multiphase-field model for modeling non-isothermal transport of fluid and solid particles.*

IV. Oyedokun O. and Schubert J. 2017. Estimating Caving Size during Wellbore Breakout. (Submitted to *International Journal of Rock Mechanics and Mining Sciences*): *The paper presents a framework for determining the dimensions of caving generated during the breakout process. The limiting buckling lengths of the slender rock-layers, which form during the process are determined using theory of plate buckling.*

V. Oyedokun O. and Schubert J. 2017. Development of an Energy-Consistent Erosion Constitutive Relation for Deformable Porous Media (submitted to *Transport in Porous Media*): *The proposed erosion constitutive relation, which satisfies the principle of frame indifference, captures the impacts of compacton on the rate of erosion.*